NUREG-2238

U.S.NRC
United States Nuclear Regulatory Commission
Protecting People and the Environment

Validation of a Computational Fluid Dynamics Method Using Vertical Dry Cask Simulator Data

Office of Nuclear Regulatory Research

AVAILABILITY OF REFERENCE MATERIALS IN NRC PUBLICATIONS

NRC Reference Material

As of November 1999, you may electronically access NUREG-series publications and other NRC records at the NRC's Public Electronic Reading Room at http://www.nrc.gov/reading-rm.html. Publicly released records include, to name a few, NUREG-series publications; *Federal Register* notices; applicant, licensee, and vendor documents and correspondence; NRC correspondence and internal memoranda; bulletins and information notices; inspection and investigative reports; licensee event reports; and Commission papers and their attachments.

NRC publications in the NUREG series, NRC regulations, and Title 10, "Energy," in the *Code of Federal Regulations* may also be purchased from one of these two sources.

1. **The Superintendent of Documents**
   U.S. Government Publishing Office
   Washington, DC 20402-0001
   Internet: http://bookstore.gpo.gov
   Telephone: 1-866-512-1800
   Fax: (202) 512-2104

2. **The National Technical Information Service**
   5301 Shawnee Road
   Alexandria, VA 22161-0002
   http://www.ntis.gov
   1-800-553-6847 or, locally, (703) 605-6000

A single copy of each NRC draft report for comment is available free, to the extent of supply, upon written request as follows:

U.S. Nuclear Regulatory Commission
Office of Administration
Multimedia, Graphics and Storage & Distribution Branch
Washington, DC 20555-0001
E-mail: distribution.resource@nrc.gov
Facsimile: (301) 415-2289

Some publications in the NUREG series that are posted at the NRC's Web site address http://www.nrc.gov/reading-rm/doc-collections/nuregs are updated periodically and may differ from the last printed version. Although references to material found on a Web site bear the date the material was accessed, the material available on the date cited may subsequently be removed from the site.

Non-NRC Reference Material

Documents available from public and special technical libraries include all open literature items, such as books, journal articles, transactions, *Federal Register* notices, Federal and State legislation, and congressional reports. Such documents as theses, dissertations, foreign reports and translations, and non-NRC conference proceedings may be purchased from their sponsoring organization.

Copies of industry codes and standards used in a substantive manner in the NRC regulatory process are maintained at—

The NRC Technical Library
Two White Flint North
11545 Rockville Pike
Rockville, MD 20852-2738

These standards are available in the library for reference use by the public. Codes and standards are usually copyrighted and may be purchased from the originating organization or, if they are American National Standards, from—

American National Standards Institute
11 West 42nd Street
New York, NY 10036-8002
http://www.ansi.org
(212) 642-4900

Legally binding regulatory requirements are stated only in laws; NRC regulations; licenses, including technical specifications; or orders, not in NUREG-series publications. The views expressed in contractor-prepared publications in this series are not necessarily those of the NRC.

The NUREG series comprises (1) technical and administrative reports and books prepared by the staff (NUREG-XXXX) or agency contractors (NUREG/CR-XXXX), (2) proceedings of conferences (NUREG/CP-XXXX), (3) reports resulting from international agreements (NUREG/IA-XXXX), (4) brochures (NUREG/BR-XXXX), and (5) compilations of legal decisions and orders of the Commission and Atomic and Safety Licensing Boards and of Directors' decisions under Section 2.206 of NRC's regulations (NUREG-0750).

NUREG-2238

U.S.NRC
United States Nuclear Regulatory Commission
Protecting People and the Environment

Validation of a Computational Fluid Dynamics Method Using Vertical Dry Cask Simulator Data

Manuscript Completed: March 2020
Date Published: June 2020

Prepared by:

Abdelghani Zigh
Sergio Gonzalez

Office of Nuclear Regulatory Research

ABSTRACT

Applicants submit spent nuclear fuel dry storage cask designs to the U.S. Nuclear Regulatory Commission (NRC) for certification under Title 10 of the *Code of Federal Regulations* (10 CFR) Part 72, "Licensing Requirements for the Independent Storage of Spent Nuclear Fuel, High-Level Radioactive Waste, and Reactor-Related Greater Than Class C Waste." The NRC staff performs its technical review of these designs in accordance with 10 CFR Part 72 and NUREG-1536, "Standard Review Plan for Spent Fuel Dry Storage Systems at a General License Facility—Final Report," Revision 1, issued July 2010. To ensure that the cask and fuel material temperatures of the dry cask storage system remain within the allowable limits or criteria for normal, off-normal, and accident conditions, the NRC staff performs a thermal review as part of the technical review.

Recent applications increasingly have conducted thermal-hydraulic analyses using computational fluid dynamics (CFD) codes (e.g., ANSYS Fluent) to demonstrate the adequacy of the thermal design. The applicants also want to license casks with decay heat close to 50 kilowatts, resulting in a peak cladding temperature (PCT), close (i.e. small margins) to the temperature limit of 400 degrees Celsius suggested in Interim Staff Guidance 11, "Cladding Considerations for the Transportation and Storage of Spent Fuel," issued November 2003. These PCT predictions presented by the applicants usually are not supported by an uncertainty quantification calculation to assure the thermal reviewer that the calculated temperature margin is adequate. As such, the NRC Office of Nuclear Material Safety and Safeguards asked the NRC Office of Nuclear Regulatory Research to perform validation studies of the ANSYS Fluent CFD code to assist it in making regulatory decisions to provide reasonable assurance of adequate protection for storage casks and transportation packages. The validation studies were based on experimental data documented in NUREG/CR-7250, "Thermal-Hydraulic Experiments Using a Dry Cask Simulator," issued October 2018 [6].

NUREG/CR-7250 documents a series of tests conducted using a single, prototypic-geometry boiling-water reactor fuel assembly inside a pressure vessel and enclosure to mimic the thermal-hydraulic responses of both aboveground and underground dry storage casks. This simplified test assembly was shown to be similar to prototypic systems through dimensional analysis. The data were collected over a broad range of parameters, including simulated decay power and internal helium pressure.

Previous submissions by applicants and vendors to the NRC have generally employed CFD using finite volume to demonstrate regulatory compliance for the thermal performance of dry cask storage systems. Additionally, when demonstrating compliance, it is valuable to quantify the uncertainty in the simulation result as a function of the computational mesh and simulation inputs. This CFD validation included uncertainty quantification, using American Society of Mechanical Engineers (ASME) Verification and Validation (V&V) 20-2009, "Standard for Verification and Validation in Computational Fluid Dynamics and Heat Transfer" [2]. Additionally, the validation used CFD best practice guidelines [13] to create the CFD model.

This report discusses validation and uncertainty quantification of a CFD model using the experimental data from NUREG/CR-7250. Air mass flow rate, and PCT were used as the primary variables of interest (i.e., target variables) in this validation. Uncertainty quantification follows the procedures outlined in ASME V&V 20-2009. Sources of uncertainty examined in the analysis include simulation input uncertainty, numerical errors (i.e., iterative, discretization, and round-off), and experimental errors.

The CFD results and experimental data for PCT and air mass flow rate agreed very favorably for the collected cases within the calculated validation uncertainty, which includes the combination of simulation and experimental uncertainty. The simulation uncertainty consists of model input uncertainty and numerical errors. The results show that an ANSYS Fluent thermal model using NUREG-2152 [13] CFD best practice guidelines can demonstrate the safety of the storage of spent nuclear fuel. This report also looks at the quality of the data collected in the DCS experiment documented NUREG/CR-7250 [6] using the calculated validation uncertainty. The low values of the validation uncertainty indicate that the experiment undertaken in this program is considered a CFD-grade experiment. The DCS experiment was designed to minimize the validation uncertainty—a key factor and the basis for thermal model validation. Consequently, a well-validated thermal model will enable thermal reviewers to have confidence in the predictions, even with decreased margins. This document shows that a best estimate analysis is a method that includes a model with design basis, implemented with uncertainty quantification.

TABLE OF CONTENTS

LIST OF FIGURES

LIST OF TABLES

EXECUTIVE SUMMARY

The thermal performance of commercial nuclear spent fuel dry storage casks is often evaluated through detailed numerical analysis. The cask system vendors complete these modeling efforts, often using computational fluid dynamics (CFD) analysis codes, to demonstrate performance and regulatory compliance. They are part of an application for a Certificate of Compliance (for a cask system design) from the U.S. Nuclear Regulatory Commission (NRC). The NRC staff then independently verifies the calculations. Carefully measured data sets generated from testing full-sized casks or smaller cask analogs (i.e., scale testing) are widely recognized as vital for validating these models. Some of the descriptions, and text in this section are taken from ASME V&V 20-2009 [2], NUREG/CR-7260 [7], Bestion et al., "Requirement for CFD-Grade Experiments for Nuclear Reactor Thermal-Hydraulics," issued in 2019 [3], and Bestion et al., "Review of Uncertainty Methods for Computational Fluid Dynamics Application to Nuclear Reactor Thermal Hydraulics," issued in 2016 [4].

Advances in dry storage cask designs have significantly increased the maximum thermal load allowed in a cask, in part by increasing the efficiency of internal conduction pathways and by increasing the internal convection through greater canister helium pressure. These same canister cask systems rely on ventilation between the canister and the overpack to convect heat away from the canister to the environment for both aboveground and underground configurations. While several testing programs have been conducted previously, these earlier validation attempts did not capture the effects of elevated helium pressures or accurately portray the external convection of aboveground and underground canister dry cask systems.

The purpose of this investigation is to validate the ANSYS Fluent CFD code using the experimental data documented in NUREG/CR-7250, "Thermal-Hydraulic Experiments Using a Dry Cask Simulator," issued October 2018 [6], to test the validity of the modeling presently used to determine cladding temperatures and air mass flow rates in vertical dry casks. Fuel cladding temperatures are critical to evaluate cladding integrity throughout the storage cycle. To produce these data sets under well-controlled boundary conditions, the dry cask simulator was built to study the thermal-hydraulic response of fuel under a variety of heat loads, internal vessel pressures, and external configurations.

As described in NUREG/CR-7250 [6]:

> Over 40 unique data sets were collected and analyzed for these efforts, as described in NUREG/CR-7250 [6]. Fourteen data sets for the aboveground configuration were recorded for powers and internal pressures ranging from 0.5 to 5.0 kilowatts (kW) and 0.3 to 800 kilopascals (kPa) absolute, respectively as shown in Table 4-1. Similarly, 14 data sets were logged for the underground configuration, starting at ambient conditions and concluding with thermal-hydraulic steady state as shown in Table 4-4. Over 13 tests were conducted using a custom-built wind machine. This addition to the dry cask experimental database signifies a substantial addition of first-of-a-kind, high-fidelity transient and steady-state thermal-hydraulic data sets suitable for CFD model validation.
>
> An electrically heated, but otherwise prototypic, boiling-water reactor Incoloy-clad test assembly was placed inside a representative storage basket and cylindrical pressure vessel representing a vertical canister system. The symmetric single assembly geometry with well-controlled boundary conditions simplified the interpretation of results. Simulated decay power was scaled to mimic the desired range of prototypic dimensionless groups. One unique aspect of the test apparatus was the capability to

> pressurize the simulated canister to a wide range of absolute pressures, from sub-atmospheric (0.3 kPa) to the upper range of prototypic values (800 kPa). Two different arrangements of ducting were used to mimic conditions for aboveground and underground storage configurations for vertical dry cask systems with canisters. A wind machine tested the effect of wind speed on the peak cladding temperature (PCT) and induced air mass flow rate in the underground configuration.

The power levels tested were 0.5, 1.0, 2.5, and 5.0 kW. These simulated decay power values were scaled to mimic the desired range of prototypic dimensionless groups such as Rayleigh, Nusselt, and Reynolds numbers for both internal (i.e., helium flow) and external flow (i.e., air flow). Transverse and axial temperature profiles were measured throughout the test assembly. The induced air mass flow rate was measured for both the aboveground and underground configurations without wind effect. In addition, the impact of crosswind conditions on the underground configuration was quantified. The impact of crosswind speed ranging between 0–5.4 meters per second (12 miles per hour) on the change of PCT and induced air mass flow rate was investigated for the underground case.

CFD models were built for each of these configurations and tested under the same conditions to support the validation study. Steady-state and transient simulations were performed at different decay heat power values and canister helium pressures. PCT, temperature profiles for different wall structures (i.e., channel box, basket, and pressure vessel), and air mass flow rate from the CFD predictions were compared to the experimental data.

Uncertainty quantification (UQ) was performed using American Society of Mechanical Engineers (ASME) Verification and Validation (V&V) 20-2009, “Standard for Verification and Validation in Computational Fluid Dynamics and Heat Transfer” [2], for the target variables of interest, including PCT and air mass flow rate. Sources of uncertainty that were examined in the analysis include simulation input, numerical errors (i.e., iterative, discretization, and round-off), and experimental errors.

The CFD results and experimental data for PCT and air mass flow rate agreed very favorably within the calculated validation uncertainty, as illustrated in Chapter 4, for all the cases. The validation uncertainty includes the combination of simulation and experimental uncertainty. The simulation uncertainty includes simulation input and numerical uncertainties. The results demonstrate that an ANSYS Fluent thermal model that was developed based on CFD best practice guidelines, as documented in NUREG-2152, “Computational Fluid Dynamics Best Practice Guidelines for Dry Cask Applications, Final Report,” issued March 2013 [13], can be used to demonstrate the safety of dry cask storage system design.

The NRC uses ASME V&V 20-2009 [2] methods to evaluate uncertainties in CFD. As found in NUREG/CR-7260, “CFD Validation of Dry Cask Storage Systems,” issued May 2019 [7]:

> UQ starts by clearly identifying the various sources of uncertainties using a phenomena identification and ranking table (PIRT). The deficiencies or inaccuracies of CFD simulations can be attributed to a wide number of errors and uncertainties. These errors and uncertainties consist of two main broad categories. The first category is related to modeling physics, while the second is concerned with the numerical aspect of the solution. The first category includes simplification of physical complexity, boundary and initial conditions, and physical boundary conditions. The second category includes computer programming, round-off, spatial discretization, temporal discretization, and iterative convergence. When performing validation simulations, it is mandatory to

> quantify and reduce the different errors and uncertainties originating from these sources. Despite all these errors and inaccuracies, CFD still remains a reliable method to simulate dry cask thermal response accurately with low margins when best practice guidelines are used. Best practice guidelines, such as those in NUREG-2152 [13] and ASME V&V 20-2009 [2], are an excellent source for the CFD user to avoid errors and quantify uncertainties.

In the current validation, the geometry was well prescribed; consequently, geometrical input was not the main source of the validation error (i.e., fluid gaps), as found in NUREG/CR-7260, "CFD Validation of Vertical Dry Cask Storage System," issued May 2019 [7].

ASME V&V 20-2009 [2] clearly states that the scope of V&V is the quantification of the degree of accuracy of the simulation of a specified validation variable at a specified validation point for cases in which the conditions of the actual experiment are simulated. As reported in Bestion et al., "Requirement for CFD-Grade Experiments for Nuclear Reactor Thermal-Hydraulics," issued by the "Organization for Economic Co-operation and Development, Nuclear Energy Agency, Committee on the Safety of Nuclear Installations, Working Group on Analysis and Management of Accidents, CFD group", 2019 [3]:

> Practically, ASME V&V 20-2009 affirms that, "The ultimate goal of V&V is to determine the degree to which a model is an accurate representation of the real world." This standard is strongly based on the use of experimental data for V&V and consequently for UQ. With this approach, the ASME standard puts a strong link between V&V and UQ.

Also, as reported in Bestion et al., "Review of Uncertainty Methods for Computational Fluid Dynamics Application to Nuclear Reactor Thermal Hydraulics," Organization for Economic Co-operation and Development, Nuclear Energy Agency, Committee on the Safety of Nuclear Installations, Working Group on Analysis and Management of Accidents, CFD group, 2016 [4]:

> The ASME standard methodology for uncertainty analysis underlines the role of V&V in the process of evaluating the confidence in CFD results. Uncertainties must be evaluated step by step, using clearly defined numerical aspects of the model such as time and space discretization (time step and mesh convergence) or physical models (turbulence models, physical assumptions) with associated evaluation of error.
>
> The ASME standard conforms to NRC regulatory practices, procedures, and methods for licensing dry cask systems as embodied in Title 10 of the *Code of Federal Regulations* and other pertinent documents, such as Regulatory Guide 1.203, "Transient and Accident Analysis Methods," and NUREG-0800, "NRC Standard Review Plan for the Review of Safety Analysis Reports for Nuclear Power Plants: LWR Edition" [16].

Looking at validation experiments for CFD application to dry cask simulation for both design and safety studies, it appears that available data often suffer from a lack of local measurements (e.g., fuel and different dry cask wall temperature profiles and pressures, induced air mass flow rate), an insufficient number of measured flow variables, a lack of well-defined initial and boundary conditions, and a lack of information on experimental uncertainty. A working group on CFD applications to nuclear safety of the Organisation for Economic Co-operation and Development, Nuclear Energy Agency, Committee on the Safety of Nuclear Installations (CSNI), and the Working Group on Analysis and Management of Accidents established some requirements for CFD-grade experiments able to properly validate the single-phase CFD tools [3]. This report evaluates the quality of experiment used for the validation, based on the validation uncertainty as defined by ASME V&V 20-2009 [2] and the work presented in Bestion

et al. [3]. The discussion on this topic establishes whether this is a CFD-grade experiment. CFD-grade experiments should be able to validate a CFD model, and the main concern is to minimize the validation uncertainty on some selected figures of merit or target variables, such as PCT and air mass flow rate.

Clear objectives should be first defined in an experimental program designed to validate a computational method. The success of the validation hinges on the constant collaboration between the experimentalist and the CFD specialist. This discussion should define the test section geometry, initial and boundary conditions, and the requirement for measurement uncertainty. There needs to be agreement on what to measure, where it will be measured, and with which measurement technique. Acceptance criteria may be defined on the sensitivity of the measured parameters to the process of interest, or on the required accuracy of some selected physical quantity, or both. Preliminary code simulations are necessary to define appropriate model boundaries and measurement locations, with sensitivity tests to determine the uncertainty of initial and boundary conditions and of measured field parameters. Iterations may be necessary to optimize the design.

In this experimental program, the collaboration between experimentalists at Sandia National Laboratories and NRC CFD specialists was successful. The program used CFD to perform similarity analysis and adequately choose the decay heat powers through many iterations to properly scale the model to match the conditions and thermal performance of a prototypic dry cask. Also, CFD predictions were used to check the initial shakedown tests for all the configurations. Consequently, the experimental data collected in this program were geared to obtain a CFD-grade experiment. The main objective of this experiment was the minimization of the validation uncertainty and hence the improvement of the CFD thermal model. When a thermal model is well validated, the dry cask applicants and thermal reviewers will have confidence in the predicted margins, even when minimized, without exceeding the set limit. This report shows that a well-crafted, best estimate thermal model uses the design basis following CFD best practice guidelines and complemented by UQ. Such a model will have enough information for dry cask applicants and thermal reviewers about the margins that can be considered safe for applications and certifications.

ABBREVIATIONS AND ACRONYMS

ASME	American Society of Mechanical Engineers
BC	boundary condition
BWR	boiling-water reactor
CFD	computational fluid dynamics
CFR	*Code of Federal Regulations*
CYBL	Cylindrical Boiling Facility
DCS	dry cask simulator
GCI	grid convergence index
MAWP	maximum allowable working pressure
NRC	U.S. Nuclear Regulatory Commission
$\dot{m}_{air}$	Air mass flow rate flowing through the air vents
PCT	peak cladding temperature
SIMPLE	Semi-Implicit Method for Pressure-Linked Equations
UQ	uncertainty quantification
V&V	verification and validation

1 INTRODUCTION

The thermal performance of commercial nuclear spent fuel dry storage casks is evaluated through detailed analytical modeling. The vendor undertakes these modeling efforts to demonstrate performance and regulatory compliance, which are independently verified by the U.S. Nuclear Regulatory Commission (NRC). Most commercial dry casks in use today store the fuel in an aboveground configuration, although underground storage has grown in recent years. Both horizontally and vertically oriented aboveground dry cask systems are currently in use. Figure 1-1 shows a diagram for a typical vertical aboveground system. Cooling of the assemblies located inside the sealed canister is enhanced by the induced flow of air drawn in at the bottom of the cask and exiting out at the top of the cask. Descriptions, text and figures in this section of the experiment are taken from NUREG/CR-7250.

Source : www.nrc.gov/reading-rm/doc-collections/fact-sheets/storage-spent-fuel-fs.html

Figure 1-1 Typical Vertical Aboveground Storage Cask System

Figure 1-2 shows a diagram for a vertical underground system. For this underground configuration, air is drawn in from the top periphery and channeled to the bottom of the cavity through a narrow annulus, where it then flows upward along the wall of the canister and exits out the top center vent.

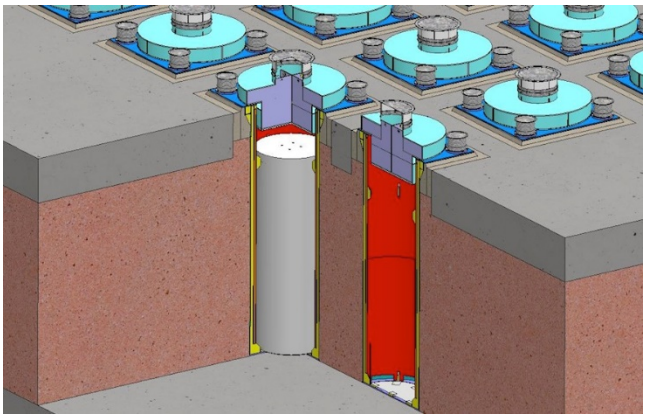

Source : www.holtecinternational.com/productsandservices/wasteandfuelmanagement/hi-storm/

Figure 1-2 Typical Vertical Underground Storage Cask System

Recent advances in dry storage cask designs have significantly increased the maximum thermal load allowed in a cask, in part by increasing the efficiency of internal conduction pathways and by increasing the internal convection through greater canister helium pressure. These vertical canister cask systems rely on ventilation between the canister and the overpack to convect heat away from the canister to the environment for both aboveground and underground configurations. While several testing programs have been previously conducted, these earlier validation attempts did not capture the effects of elevated helium pressures or accurately portray the external convection of aboveground and underground canister dry cask systems. Thus, the enhanced performance of modern dry storage casks cannot be fully validated using previous studies.

1.1 Objective

The purpose of this investigation was to validate the ANSYS Fluent computational fluid dynamics (CFD) code against the results obtained from a dry cask simulator (DCS) that was built to study the thermal-hydraulic response of fuel under a variety of heat loads, internal vessel pressures, and external configurations, as well as to perform uncertainty quantification (UQ) analysis using American Society of Mechanical Engineers (ASME) Verification & Validation (V&V) 20-2009, "Standard for Verification and Validation in Computational Fluid Dynamics and Heat Transfer" [2].

1.2 Dry Cask Simulator

This section summarizes the DCS by describing the various subsystems, construction, and methods used for this testing. NUREG/CR-7250, "Thermal-Hydraulic Experiments Using a Dry Cask Simulator," issued October 2018 [6], provides further details, including but not limited to, instrumentation equipment and its corresponding layout. The description and figures below of the experiment are taken from NUREG/CR-7250.

As described in NUREG/CR-7250 [6]:

1.2.1 General Construction

Figure 1-3 and Figure 1-4 show the general design details of the DCS. An existing electrically heated but otherwise prototypic boiling-water reactor (BWR) Incoloy-clad test assembly was placed inside a representative storage basket and cylindrical pressure vessel that represents the canister. The symmetric single assembly geometry with well-controlled boundary conditions (BCs) simplified the interpretation of results. Detailed information about this assembly can be found in earlier work done by Sandia National Laboratories (SNL) and documented in NUREG-CR-7143 [8]. Various configurations of outer concentric ducting mimicked conditions for aboveground and underground storage configurations of vertical, dry cask systems with canisters. Radial and axial temperature profiles were measured for a wide range of decay power and canister pressures. Of particular interest was the evaluation of the effect of increased helium pressure on heat load for both the aboveground and underground configurations. The effect of wind speed was also measured for the underground configuration to study the effect of a continuous crosswind on the thermal and hydraulic response of the system. Figure 1-5 shows the layout for this configuration. Air mass flow rates were calculated from measurements of the induced air velocities in the external ducting.

The DCS for the aboveground configuration consists of a BWR assembly, channel box, basket, canister/pressure vessel, outer shell (shell1), and shell1-insulation as shown in Figure 1-3 and Figure 1-4. The underground configuration consists of an additional shell2 and shell2-insulation, as depicted in Figure 1-3 and Figure 1-4.

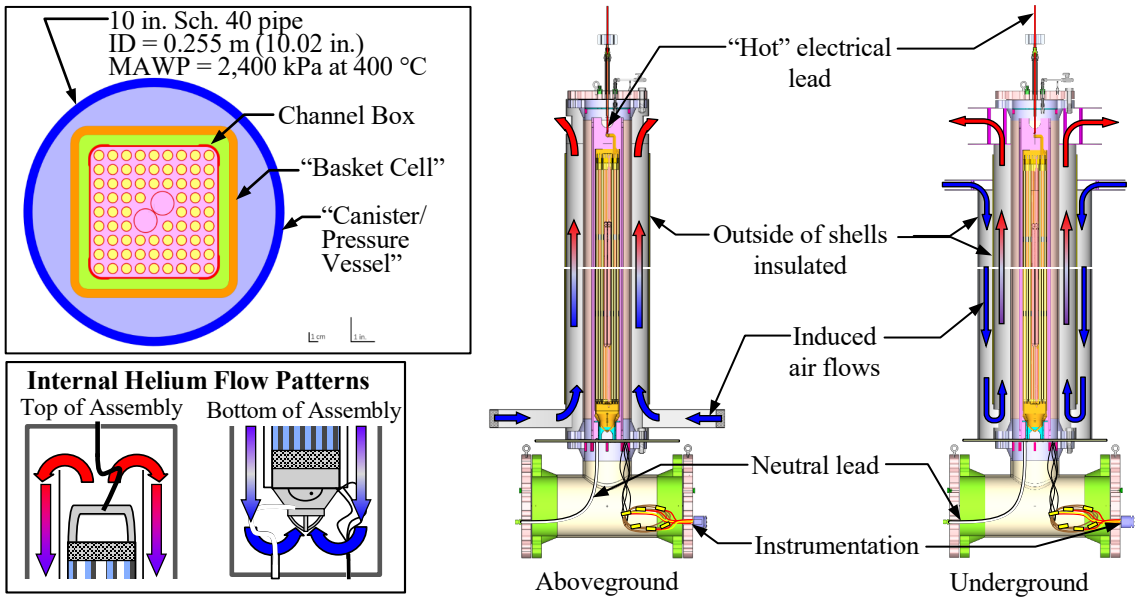

Figure 1-3 General Design Showing the Plan View (upper left), the Internal Helium Flow (lower left), and the External Air Flow for the Aboveground (middle) and Underground Configuration (right). (source: NUREG/CR-7250 [6])

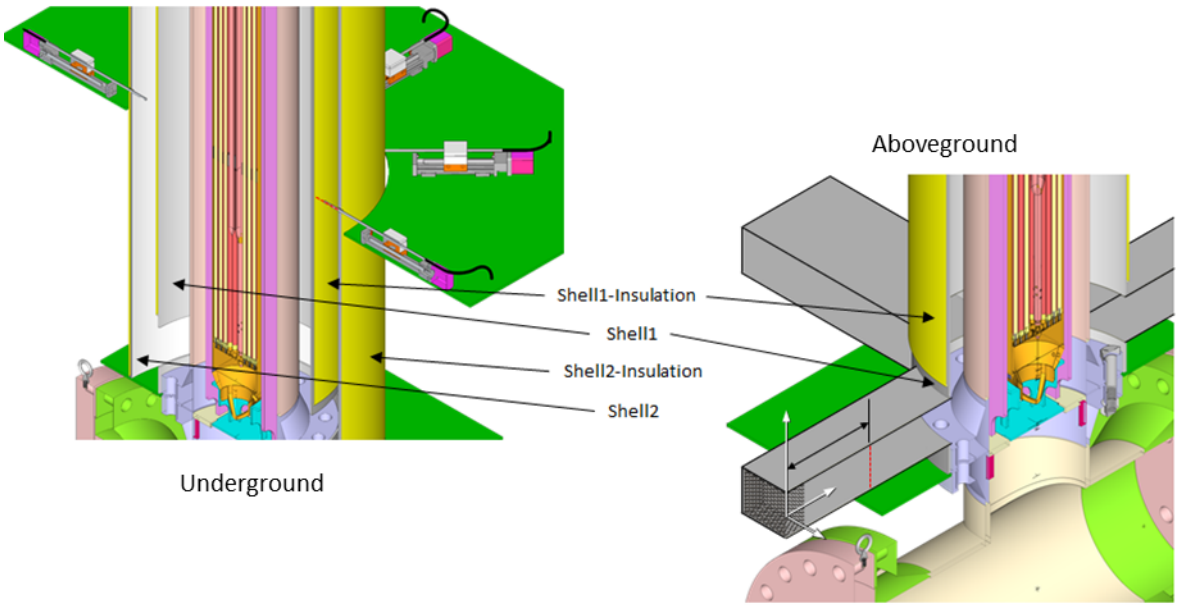

Figure 1-4 Shells around Pressure Vessels for Aboveground and Underground Configurations. (source: NUREG/CR-7250 [6])

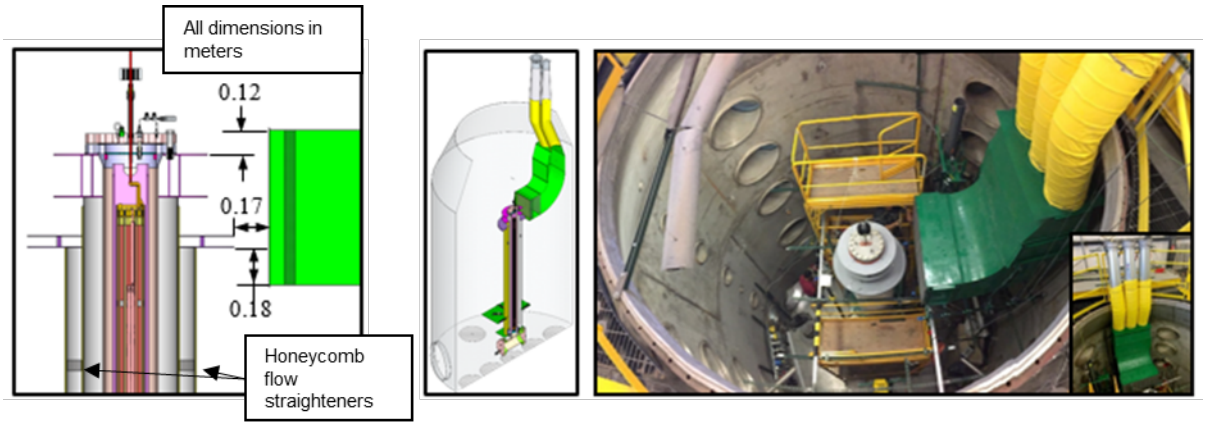

Figure 1-5 Layout of the Underground Cask with Wind Machine for Crosswind Testing. (source: NUREG/CR-7250 [6])

Figure 1-6 shows the major carbon steel components used to fabricate the pressure vessel. The 4.572-meter (m) (180-inch (in.))-long vertical test section was made from 0.254-m (10-in.) Schedule 40 pipes welded to Class 300 flanges. The 0.356 × 0.254-m (14×10-in.) Schedule 40 reducing tee was needed to facilitate the routing of over 150 thermocouples through the pressure vessel. Blind flanges with threaded access ports for thermocouples and power lead pass-through were bolted to the top of the vertical test stand section and the sides of the reducing tee. The maximum allowable working pressure (MAWP) was 2,400 kilopascal (kPa) at 400 degrees Celsius (C) (752 °F). Bar stock tabs were welded inside the 0.254-m (10-in.) flange on the tee to support the test assembly and on top of the test section to allow an insulated top BC.

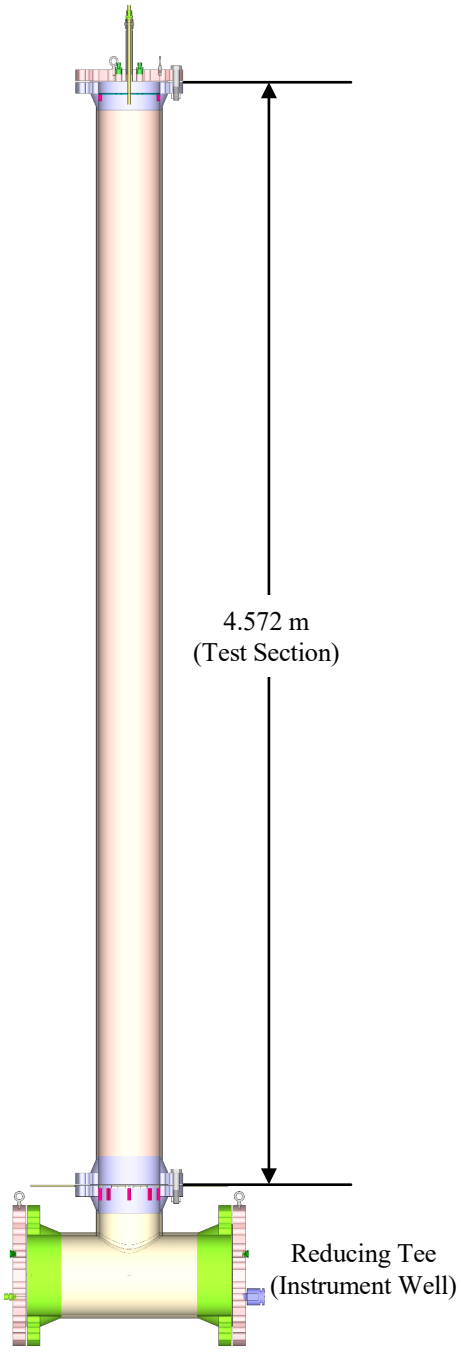

Figure 1-6 Carbon Steel Pressure Vessel. (source: NUREG/CR-7250 [6]).

The test configurations were assembled and operated inside the Cylindrical Boiling (CYBL) test facility, which is the same facility used for earlier fuel assembly studies [6]. CYBL is a large stainless-steel containment vessel repurposed from earlier flooded containment/core retention studies sponsored by the U.S. Department of Energy. Since then, CYBL has served as an excellent general use engineered barrier for the isolation of high-energy tests. The outer vessel is 5.1 m in diameter and 8.4 m tall (16.7 feet in diameter and 27.6 feet tall) and constructed with 9.5-millimeter (mm) (0.375-in.)-thick

stainless-steel walls. Figure 1-7 shows a scaled diagram of the CYBL facility with the aboveground version of the test DCS inside.

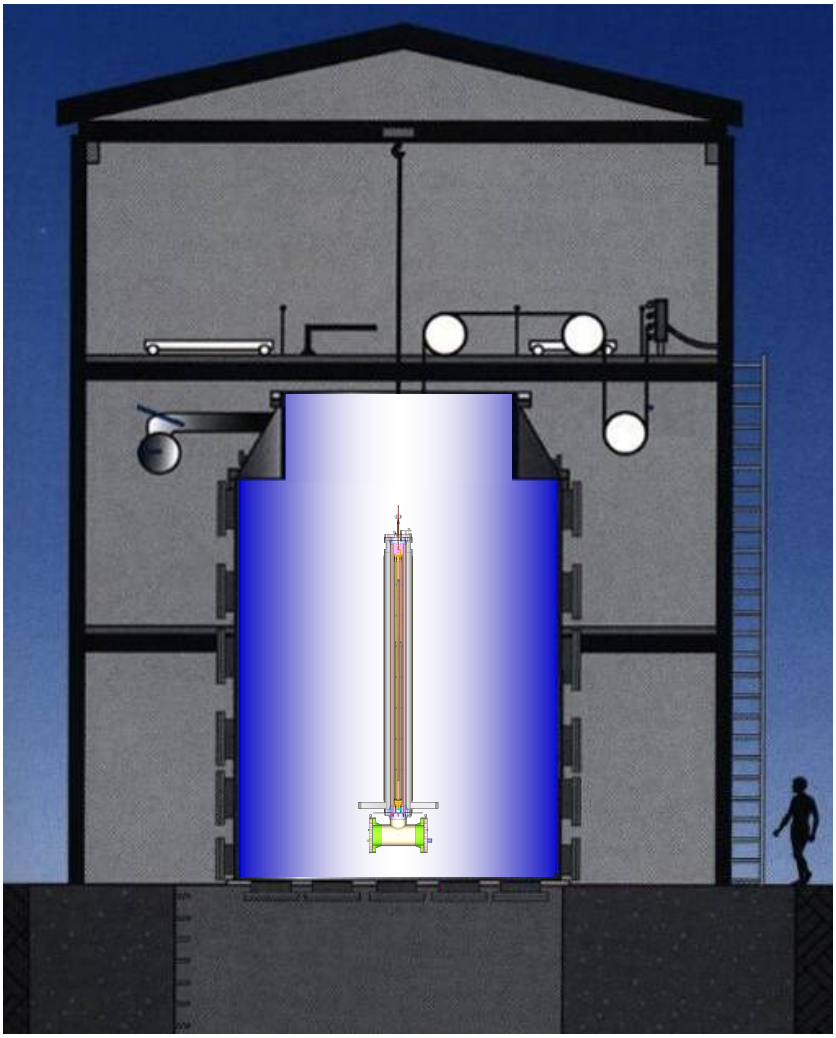

Figure 1-7 CYBL Facility Housing the Aboveground Version of the BWR Cask Simulator. (source: NUREG/CR-7250 [6]).

1.2.2 Flow Straightening

To obtain the most stable and repeatable measurements possible, a honeycomb element was inserted into the inlets of both the aboveground and underground configurations. This honeycomb served to align the flow in the desired direction and reduce any flow disturbances on the hot wire measurements. As shown in Figure 1-8, a plastic honeycomb element was chosen with a cell diameter, wall thickness, and flow length of 3.8, 0.1, and 51.6 mm (0.150, 0.004, and 2.030 in.), respectively. This type of flow-straightening element was found to provide the greatest reduction in hot wire fluctuations while introducing the smallest pressure drop to the system. The effective frictional coefficient for this honeycomb material was found to be

D = 2.7x10^{6} m^{-2} for porous media in CFD simulations.

Detailed information and derivation of the frictional coefficient (i.e. D) is in NUREG-2152 [13] and NUREG-2208 [15].

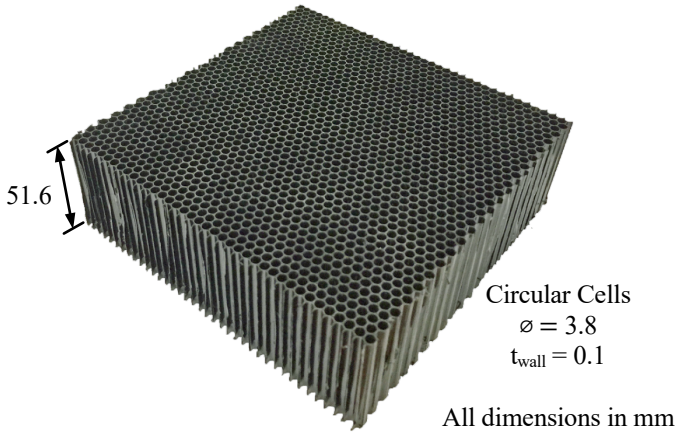

Figure 1-8 Photograph of the Honeycomb Element Used for Flow Straightening. (source: NUREG/CR-7250 [6])

1.2.3 Design of the Heated Fuel Bundle

The highly prototypic fuel assembly was modeled after a 9×9 BWR assembly. Commercial components were purchased to create the assembly, including the top and bottom tie plates, spacers, water rods, channel box, and all related assembly hardware (see Figure 1-9). Incoloy heater rods were substituted for the fuel rod pins for heated testing. Due to fabrication constraints, the diameter of the Incoloy heaters was slightly smaller than prototypic pins, 10.9 mm versus 11.2 mm. The slightly simplified Incoloy mock fuel pins were fabricated based on drawings and physical examples from the nuclear component supplier. Table 1-1 lists the dimensions of the assembly components. This report refers to the lower (full) section as fully populated and to the upper (partial) section as partially populated. NUREG/CR-7250 [6] includes further details on the BWR assembly geometry.

Table 1-1 Dimensions of Assembly Components in the 9×9 BWR

Description	Lower (Full) Section	Upper (Partial) Section
Number of pins	74	66
Pin diameter (mm)	10.9	10.9
Pin pitch (mm)	14.4	14.4
Pin separation (mm)	3.48	3.48
Water rod outer diameter (main section) (mm)	24.9	24.9
Water rod inner diameter (mm)	23.4	23.4
Nominal channel box inner diameter (mm)	134	134
Nominal channel box outer diameter (mm)	139	139

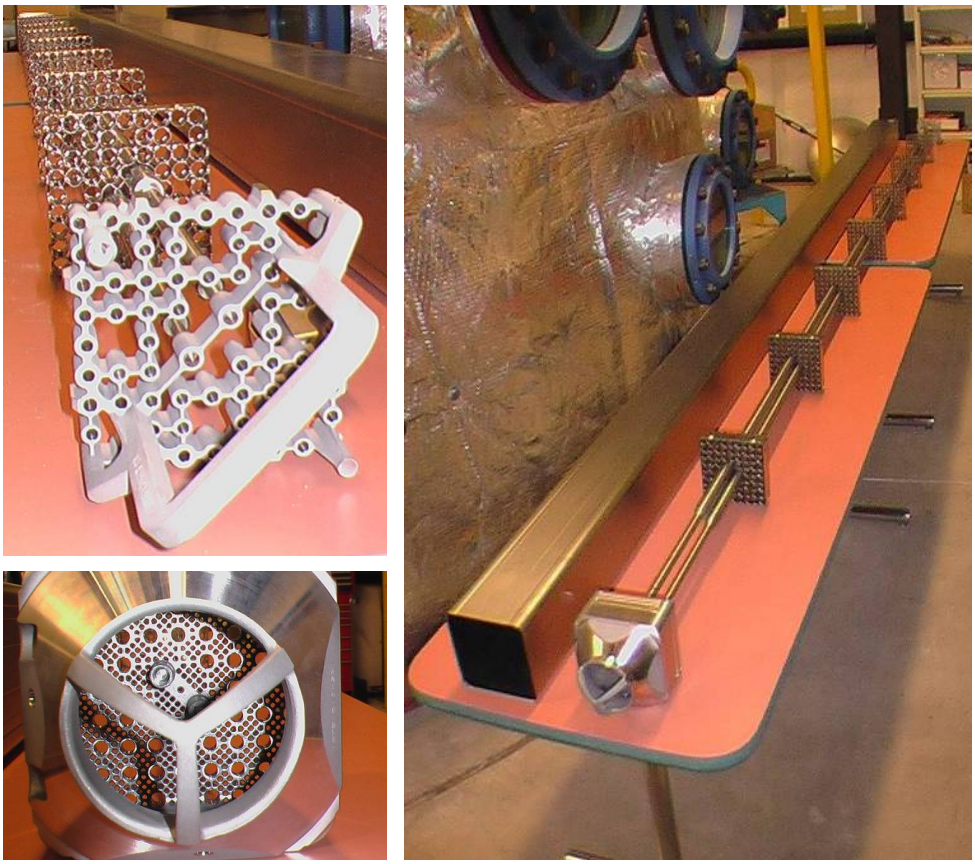

Figure 1-9 Typical 9×9 BWR Components Used to Construct the Test Assembly, Including Top Tie Plate (upper left), Bottom Tie Plate (bottom left), and Channel Box and Spacers Assembled onto the Water Rods (right). (source: NUREG/CR-7250 [6])

1.2.4 Test Plan

A total of fourteen tests were conducted where the DCS achieved steady state for various assembly powers and pressures using the aboveground configuration. The power levels

tested were 0.5, 1.0, 2.5, and 5.0 kW. The vessel pressures tested were sub-atmospheric (0.3 kPa), 100, 450, and 800 kPa absolute. Similarly, a total of fourteen tests were conducted where the DCS achieved steady state for various assembly powers and vessel pressures using the underground configuration. Like the aboveground cases, the power and pressure levels tested with the underground configuration were (0.5, 1.0, 2.5 and 5.0) kW, and (sub-atmospheric (0.3 kPa), 100, 450 and 800) kPa absolute respectively.

A scaling analysis in Durbin et al. "Description of Dry Cask Simulator for Measuring Internal and External Thermal-Hydraulic Performance," issued June 2016 [5] and NUREG/CR-7250, "Thermal-Hydraulic Experiments Using a Dry Cask Simulator CFD Validation of Vertical Dry Cask Storage System", issued October 2018 [6], showed that elevated powers up to 5.0 kW were warranted to drive the induced air flow to prototypic levels. NUREG/CR-7250 [6] has detailed information about the dimensional and scaling analyses performed for this experiment.

Past analysis in NUREG-2174, "Impact of Variation in Environmental Conditions on the Thermal Performance of Dry Storage Casks," issued March 2016 [14], showed that only in underground casks was the thermal response affected by crosswind due to vent blockage. As such, lower mass flow rate to cool the cask is available, leading to a higher peak cladding temperature (PCT).

Two types of crosswind tests were conducted. In both types of test, the DCS was first allowed to reach thermal steady state for the given test conditions and zero crosswind. For the first type of crosswind testing, after reaching steady state, the wind machine was then started using constant crosswind speed for 12 to 18 hours. Six extended duration tests of the first type were conducted for (1.0 kW, 100 kPa) and (5.0 kW, 100 kPa) using a crosswind speed of 1.4, 2.7, and 5.3 meters per second (m/s).

For the second type of crosswind testing, the wind speed was changed at 1-hour intervals to more efficiently probe the effect of crosswind speed on the induced air mass flow rate. Thermal steady state was not reestablished. The effect of crosswind velocity (from 0.5 to 5.4 m/s) on the induced air flow rate was measured for three powers (1.0 kW, 2.5 kW, and 5.0 kW) and three helium pressures (100 kPa, 450 kPa, and 800 kPa).

1.3 Computational Fluid Dynamics Model

ANSYS Fluent version 18 was used to create a three-dimensional CFD thermal model, as illustrated in Figure 1-10 and Figure 1-11, to model the thermal response of the DCS. The model's geometry and mesh were created and built using Gambit version 2.4. CFD guidelines in NUREG-2152, "Computational Fluid Dynamics Best Practice Guidelines for Dry Cask Applications," issued March 2013 [13], were followed to create the DCS thermal model. Description of boundary conditions and model input is described in Chapter 2.

Figure 1-10 illustrates a cross section of the aboveground and underground case models. Both models used 1/4th symmetry BCs to reduce the computational effort. These models did not include the inside of the CYBL facility. Convective and radiative heat BCs were applied at the external walls of the DCS for the aboveground and underground configurations, as shown in Figure 1-10. A quiescent environment was assumed for the surroundings to model the domain outside these two configurations shown in Figure 1-10.

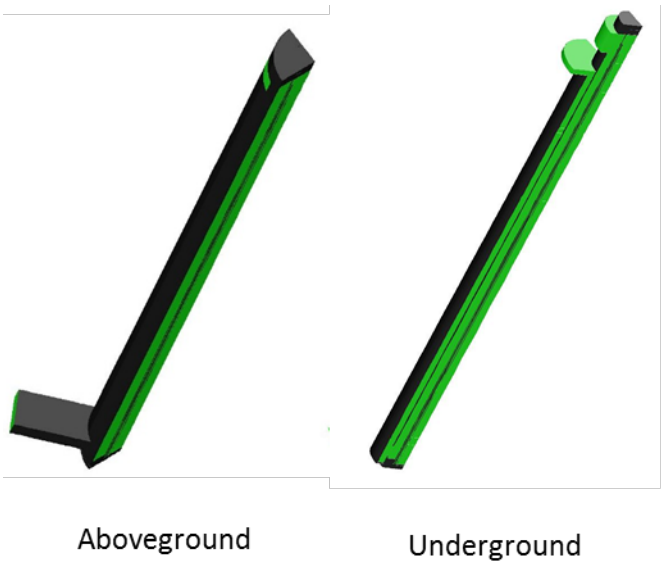

Figure 1-10 CFD Models for the Aboveground and Underground Configurations

To model the wind effects for the underground case, a half symmetry model was used to properly account for the existing BCs, as shown in Figure 1-11. In this case, the CYBL facility was part of the model, due to the wind supply outside the underground DCS configuration. The model specified the environment outside of CYBL as a quiescent medium. Convection and radiation BCs were used on the outer CYBL facility walls. Chapter 2 further discusses the details on building the CFD model.

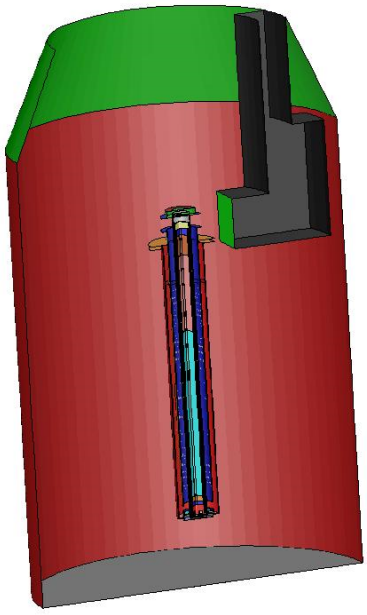

Figure 1-11 CFD Model for the Underground Configuration with Crosswind Conditions

1.4 Uncertainty Quantification

ASME V&V 20-2009 [2] established steps to assess the degree of accuracy of computational simulations. The accuracy of the method is obtained by comparing the experiment and the simulation of a local or global variable. From the validation process provided in ASME V&V 20-2009, the criteria for a CFD-grade experiment can be established, as also discussed in ASME V&V 20-2009. A CFD-grade experiment should be able to validate CFD model with a minimization of the validation uncertainty on some selected figures of merit variable. As Interim Staff Guidance (ISG)-11, "Cladding Considerations for the Transportation and Storage of Spent Fuel," issued November 2003 [12], used PCT as a criterion to assess the safety of a dry cask, this report also uses it as the figure of merit or the target variable to assess the validation uncertainty. In turn, the validation uncertainty will be used to qualify the experiment as CFD-grade or not. The derivations, and text below are taken from ASME V&V 20-2009 [2], NUREG/CR-7260 [7], and Bestion et al., "Requirement for CFD-Grade Experiments for Nuclear Reactor Thermal-Hydraulics," issued in 2019 [3].

As found in NUREG/CR-7260, "CFD Validation of Dry Cask Storage Systems," issued May 2019 [7]:

> The validation comparison error E in any validation process is defined as the difference between the solution denoted by S, and the experimental data denoted by D:
>
> $$\mathrm{E} = \mathrm{S} - \mathrm{D}$$
>
> If T represents the true solution, then the errors in the solution and experiment are:
>
> $$\delta_{\mathrm{S}} = \mathrm{S} - \mathrm{T}$$
>
> $$\delta_{\mathrm{D}} = \mathrm{D} - \mathrm{T}$$
>
> Then E can be written as:
>
> $$\mathrm{E} = (\mathrm{S} - \mathrm{T}) - (\mathrm{D} - \mathrm{T}) = \delta_{\mathrm{S}} - \delta_{\mathrm{D}}$$
>
> The simulation error δ_S consists of three categories including the modeling error δ_{model} due to physical modeling input, with approximations and assumptions; the numerical solution error δ_{num} stemming from the numerical algorithm and the discrete mesh used to solve the partial differential equations; and the input data errors δ_{input} resulting from the simulation input parameters (e.g., initial conditions, BCs, properties). E is thus the overall result of all the errors coming from the experimental data and the simulation.
>
> $$\mathrm{E} = \delta_{\mathrm{model}} + \delta_{\mathrm{input}} + \delta_{\mathrm{num}} - \delta_{\mathrm{D}}$$
>
> The unknown error δ_{model} produced by the modeling is isolated:
>
> $$\delta_{\mathrm{model}} = \mathrm{E} - (\delta_{\mathrm{input}} + \delta_{\mathrm{num}} - \delta_{\mathrm{D}})$$
>
> The corresponding standard uncertainties for the input, numerical, and experimental errors are $\mathrm{u}_{\mathrm{input}}$, $\mathrm{u}_{\mathrm{num}}$ and u_{D}.
>
> The validation standard deviation of the combination error $\delta_{\mathrm{input}} + \delta_{\mathrm{num}} - \delta_{\mathrm{D}}$ is denoted as u_{val} and if the three errors are mutually independent then:
>
> $$\mathrm{u}_{\mathrm{val}} = \sqrt{\mathrm{u}_{\mathrm{input}}^2 + \mathrm{u}_{\mathrm{num}}^2 + \mathrm{u}_{\mathrm{D}}^2}$$
>
> $$\delta_{\mathrm{model}} = \mathrm{E} \pm \mathrm{u}_{\mathrm{val}}$$
>
> If also δ_{model} is considered independent, then:

$$u_E = \sqrt{u_{model}^2 + u_{input}^2 + u_{num}^2 + u_D^2}$$

The ASME standard gives solutions to evaluate every term of the comparison error (E) and the validation uncertainty ($\mathbf{u_{val}}$). The validation comparison error E sign and its magnitude are known once the validation comparison is made. The validation uncertainty can be estimated through the determination of the simulation uncertainty $u_{simulation}$ and the experimental uncertainty u_D. The simulation uncertainty consists of the numerical simulation uncertainty u_{num} and the input uncertainty u_{input}. However, there is no established method to estimate the physical modelling uncertainty u_{model}.

Propagation methods are mainly used to evaluate code result uncertainties coming from input parameters. Uncertainties of numerical solutions are given by the solution verification step or grid convergence index (GCI) method based on the Richardson extrapolation method. The standard indicates how to use the E and $\boldsymbol{u_{val}}$. These quantities give the accuracy of the model used through:

$$u_{model} = \sqrt{u_E^2 - u_{val}^2}$$

From these equations, the following criteria can be concluded:

- If $|\mathbf{E}| >> \mathbf{u_{val}}$, $\mathbf{u_{model}} \cong \mathbf{u_E}$, then $\mathbf{u_{val}}$ is relatively small and the modeling error is larger than the validation uncertainty. In this case, the comparison between the code predictions and the experimental data can provide useful and precise information on the quality of the physical model. Consequently, the model can be improved or calibrated using the data from the experiment to achieve less uncertainty for the result.

- If $|\mathbf{E}| < \mathbf{u_{val}}$, the larger validation uncertainty implies that the model accuracy cannot be improved if the combination δ_{input}, δ_{num} and δ_D cannot be reduced. In this case, the standard indicates that this does not prove that the model is of good or bad quality, but this kind of experiment will not be useful in improving the model.

- If $|\mathbf{E}| = \mathbf{u_{val}}$, the modeling error is within the noise level imposed by the input, numerical, and experimental uncertainties, and the possibility of model improvement is a challenge.

- If model uncertainty $\mathbf{u_{model}}$ is known or expected, sensitivity analyses on sensitive modeling parameters can investigate the impact this model uncertainty can have on target variables such as PCT and $\mathbf{u_{val}}$.

  - If $\mathbf{u_{model}} < \mathbf{u_{val}}$, the experiment is not very informative.

  - If $\mathbf{u_{model}} > \mathbf{u_{val}}$, the experiment can show whether the expected model uncertainty is reached.

A CFD-grade experiment is one that can be used to validate the physical model. This means that the experiment provides a relatively low uncertainty of validation $\mathbf{u_{val}}$ and allows a good determination of the model uncertainty $\mathbf{u_{model}}$. Therefore, an experiment that minimizes both $\boldsymbol{\delta_{input}}$ and $\boldsymbol{\delta_D}$ also minimizes $\mathbf{u_{val}}$ and provides more information on the accuracy of the model. A CFD-grade experiment should provide the lowest values of

δ_{input} and δ_{D} (i.e., low $\mathbf{u_{val}}$). In parallel, the CFD user or specialist should strive to minimize the numerical error $\mathbf{u_{num}}$ or at least follow well-established methods to quantify it correctly.

However, the capability for an experiment to provide information on the uncertainty of model parameters may not be the concern of a dry cask safety analysis. The final goal is often to compare a parameter of interest, such as PCT, to a safety criterion to assess whether the dry cask is safe in the situation for which it is designed. Very often, and due to the lack of geometrical details inside the cask, as in the case of fluid gaps as described in the cask demonstration [7], it is much more difficult to know all necessary boundary and initial conditions and flow field variables in the region of interest with low uncertainty or high confidence. As a result, $\mathbf{u_{input}}$ may be large. Such experiments should at least provide enough information to quantify the accuracy of CFD code predictions for the relevant parameters of interest in the safety analysis, such as some local temperatures or PCTs. In turn, this accuracy prediction can assess whether a reliable conclusion for the safety case can be made. The experiment should target a predetermined code uncertainty for the selected target variable, such as PCT, air mass flow rate, or other variables. Thus, instead of providing data to allow quantifying the uncertainty on some specific model parameters, the goal is the prediction of the uncertainty on the target variable of interest. This uncertainty is the result of the propagation of various sources of uncertainty from $\boldsymbol{\delta_{input}}$, $\boldsymbol{\delta_{num}}$, and $\boldsymbol{\delta_{D}}$. As such, the minimization of these sources of error remains the objective of the V&V and UQ process.

Another important requirement is the collaboration between the experiment designer and the code user from the start of the experimental project. The collaboration should target the models in the dry cask application, as shown in NUREG-2152 [13]. Code users and safety analysts can then reveal the goal of the experiment, in terms of model validation. Among these modeling goals that can be targeted and investigated are the type of turbulence model that governs the flow field, state laws for the fluid of interest, or porous media parameters if a porous media model is used. A list of modeling challenges, including BCs for dry cask applications, appears in NUREG-2152 and NUREG-2208, "Validation of Computational Fluid Dynamics Methods Using Prototypic Light Water Reactor Spent Fuel Assembly Thermal-Hydraulic Data," issued March 2017 [15]. In this important initial step, CFD code users can perform pre-calculations to help define the mockup in terms of geometrical design, range of flow variables, choice of BCs, and scaling analyses. This collaboration can also be used to define the plan of the experiment. As such, a CFD-grade experiment should first be characterized by an exchange between experimentalists and code users from the beginning of the design of the experiment to the end of the project.

The preliminary specification of fluid and solid volumes of interest and of inlet and outlet fluid surfaces is of prime importance in selecting where initial and BCs must be known. A CFD-grade experiment should specify the BCs, initial conditions, and model domain in a way that they can be used as simulation input data with the required accuracy.

A general requirement may be to define a priori acceptance criteria before designing an experiment. If the only objective is to validate a CFD code on a specific flow configuration, the acceptance criterion may be to minimize the validation uncertainty (i.e., experimental, numerical, and input uncertainties) on a specific target variable. In dry cask applications, examples may be the following:

- If the objective is to validate a CFD code for PCT, the acceptance criterion may be that the validation uncertainty related to this PCT should not exceed a given value.

- If the objective is to predict the canister wall heat transfer in a ventilated cask, the acceptance criterion may be that the validation uncertainty related to a predetermined temperature difference ΔT between the air inlet and outlet should not exceed a given value.

- If the objective is to predict the air mass flow rate in a ventilated cask, the acceptance criterion may be that the validation uncertainty related to a measured mass flow rate in the air flow passage should not exceed a given value.

In the last few years, dry cask applicants requested licenses for cask designs close to 50 kW or higher. The analyses accompanying these applications presented CFD thermal analysis cases with PCT very close to the ISG-11 allowable limit of 400 degrees C, with margins as small as 10–20 degrees C (18–36 degrees Fahrenheit (F)). As such, in this validation exercise, the calculated validation uncertainty $\mathbf{u_{val}}$ will be compared to these margins to determine whether the experiment can be classified as CFD grade.

2 COMPUTATIONAL FLUID DYNAMICS MODEL

This section summarizes the different model choices, solver settings, and thermophysical properties used in the DCS analysis.

2.1 Models, Solver Settings, and Boundary Conditions

In accordance with CFD best practice guidelines [13], hex mesh was used throughout all the control volume regions. In the air flow region, a y+ close to unity was used to appropriately use the low Reynolds k-ε turbulence model. The low Reynolds k-ε turbulence model does not use wall functions to bridge the turbulence model to the wall's BC of turbulent kinetic energy and its dissipation as is done in the standard k-ε turbulence model. The conservation equations for k and ε are integrated all the way to the wall, using finer meshing close to the wall. CFD best practice guidelines [13] were used for the expansion ratio for successive volume meshing and mesh skewness.

The BCs and model's inputs in the CFD model were representative of those present during the experiment. Porous media was used to model the inlet flow honeycomb straighteners at the inlet duct. Equivalent frictional and inertial losses in the porous model were calculated using existing flow area contractions and expansions. The outer surfaces bounding the control volume were allowed to interact with the surroundings ambient using both convection and radiation heat transfer. A natural or turbulent heat transfer correlation was used to obtain the heat transfer coefficient at these external surfaces, depending on the flow regime. The heat transfer correlations used at external walls were implemented through a subroutine linked to the main ANSYS Fluent program.

Helium gas inside the pressure vessel was assumed to be laminar, while the external air region was assumed to behave according to the low Reynolds k-ε turbulence model, using a full buoyancy effect. Calculations of Rayleigh and Reynolds numbers for helium flow inside the pressure vessel showed that the flow regime is in the laminar regime. However, Rayleigh and Reynolds numbers estimated that the air flow outside the pressure vessel is in the transitional regime. Helium and air were modeled using the ideal gas law. Both transient and steady solutions were performed in this work. The model used temperature-dependent thermophysical properties for solid materials and fluids. Material properties, including density, thermal conductivity, weight, specific heat, and emissivity, came from SAND2017-13058R, "Materials and Dimensional Reference Handbook for the Boiling Water Reactor Dry Cask Simulator," issued November 2017 [9].

The turbulence model for the air flow channel did not use any wall function models. All the conservation equations were integrated all the way to the wall and used second-order upwind discretization. Radiation heat transfer was modeled using the discrete ordinates model with second order upwind discretization. A pressure solver using the Semi-Implicit Method for Pressure-Linked Equations (SIMPLE) linked the conservation of momentum equation to the continuity equation. The least square cell-based method was used for gradient discretization. Body force weighted was used for pressure interpolation. The grid was refined until a grid-independent solution was obtained to minimize the discretization error.

The air inlet and outlet vents were modeled using pressure inlet and outlet BCs consecutively. A zero value for the static relative pressure was used at the inlet and outlet vents. The operating density was evaluated at the inlet pressure and temperature conditions,

corresponding to the ambient. The vents characterization was obtained using CFD best practice guidelines [13].

Table 2-1 shows the solver settings used in ANSYS Fluent.

Table 2-1 CFD Solver Settings

CFD Solver Settings:	Input Value:
Solver Code	ANSYS Fluent v18.0
Solver Type	Pressure Based
Viscous	Laminar (inside canister), Turbulent (air flow)
Turbulent	Low-Reynolds k-ε Model
Radiation	Discrete Ordinates, Gray Model
Pressure-Velocity Coupling Scheme	SIMPLE
Time Discretization	Steady State, Transient (second order)
Spatial Discretization:	
Gradient	Green-Gauss Node Based
Pressure	Second Order Upwind
Momentum	Second Order Upwind
Energy	Second Order Upwind
Discrete Ordinates	Second Order Upwind

Table 2-2 summarizes the BCs for all configurations.

Table 2-2 BCs for Each Configuration

	Aboveground/Underground DCS BCs	Wind Case BCs
Inlet vent	Pressure inlet	N/A
Outlet vent	Pressure outlet	N/A
DCS outer walls	Convection + Radiation	N/A
CYBL surrounding walls	N/A	Convection + radiation
CYBL top wall	N/A	Pressure boundary
Wind machine	N/A	Velocity inlet
Surrounding environment	Inside CYBL ambient air	Outside CYBL ambient air

Table 2-3 gives the settings for the Discrete Ordinates radiation model. Sensitivity runs for higher radiation parameter values than in Table 2-3 showed almost unchanged results for the temperature values. The difference in the result was minimal—less than the iterative convergence uncertainty as discussed in Section 3.1 of this report. As such, the input uncertainty analysis did not include the UQ for DO radiation parameters. The ANSYS Fluent User's Guide, issued January 2017 [1], includes detailed information about the Discrete Ordinates radiation model.

Table 2-3 Radiation Model Settings

DOs, Gray Model Inputs:	Input Value:
Theta Divisions	4
Phi Divisions	4
Theta Pixels	4
Phi Pixels	4
Energy Iterations per Radiation Iteration	10

NUREG-2208 [15] validated the use of porous media and showed that such an approach gave comparable results to the explicit model, which included fuel rods and grid spacers. Furthermore, SAND2019-6079R, "Modeling Validation Exercises Using the Dry Cask Simulator," issued May 2019 [10], confirms that the porous media representation compares very favorably with the aboveground DCS experimental data in NUREG/CR-7250 [6]. SAND2019-6079R [10] stated that NRC porous model offered results that best fit overall to the experimental data when compared with other models including CFD models that used explicit fuel representation. Furthermore, in the CFD models submitted to the NRC for review, all dry cask applicants currently favor the use of the porous media representations of the fuel assemblies, as it simplifies the configuration and saves on processing time.

The use of the porous media model for fuel rods requires the representation of these fuel rods with an equivalent frictional and inertial hydraulic loss. An equivalent thermal conductivity representing both radiation and conduction inside the assembly, along with an equivalent density and specific heat capacity, were used to represent the fuel assemblies in the model.

The combination of radiation and conduction heat transfer within the assembly is represented by an effective thermal conductivity (k_{eff}). To determine the appropriate k_{eff} for the porous media model, a two-dimensional CFD model representing the detailed cross section of an assembly, explicitly showing fuel and water rods, was used to obtain k_{eff} for different temperature BCs. Radial and axial components of the effective conductivity were calculated as shown in TRW Environmental Safety Systems, Inc., "Spent Nuclear Fuel Effective Thermal Conductivity," dated July 11, 1996 [11], and used as input for the porous media model as a function of temperature.

2.2 Porous Media Radial and Axial Thermal Conductivity

The TRW report [11] describes the k_{eff} approach in detail. In NUREG-2208 [15], calculations in the TRW report were confirmed with the developed model using CFD ANSYS Fluent, which was then used to obtain the k_{eff} for the BWR 9x9 assembly. Table 2-4 through Table 2-11 summarize the input values for the BWR fully populated and partially populated sections for the radial and axial component of the effective conductivity used in this study. The radial k_{eff} values for both helium and air were evaluated. Helium was used when the pressure vessel was pressurized between 100 to 800 kPa and air was introduced to the pressure vessel for the sub-atmospheric (i.e. 0.3 kPa) pressure cases through leakage paths.

While the canister was filled with helium during the sub-atmospheric pressure scenario, air was prevalent; thus, this scenario used the effective thermal conductivity for air. Another important aspect was the emissivity as a function of height throughout the fuel assembly, which played an important role in calculating the effective thermal conductivity. SAND2017-13058R [9] includes the measured wall emissivity values. The final effective thermal conductivity was implemented

to the CFD thermal model through a subroutine that was linked with the main ANSYS Fluent program as a function of temperature and height. The subroutine consisted of an interpolation routine for k_{eff} using channel wall emissivity and temperature as shown in Table 2-4 through Table 2-11.

Table 2-4 BWR Fully Populated Cladding Region Porous Model—Radial k_{eff} (helium)

Emissivity	Temperature (Kelvin)	k_{eff} (W/m*K)
0.2	291	0.4484
	410	0.6318
	516	0.8373
	625	1.0916
	750	1.4183
0.6	290	0.4633
	409	0.6725
	514	0.9184
	621	1.2373
	740	1.6652

Table 2-5 BWR Fully Populated Cladding Region Porous Model—Axial k_{eff} (helium)

Temperature (Kelvin)	k_{eff} (W/m*K)
273	2.0846
400	2.4077
600	2.8906
800	3.3538
1000	3.8058
1100	4.0296

Table 2-6 BWR Partially Populated Cladding Region Porous Model—Radial k_{eff} (helium)

Temperature (Kelvin)	k_{eff} (W/m*K)
285	0.4427
400	0.6641
500	0.9297
600	1.2780
700	1.7411

Table 2-7 BWR Partially Populated Cladding Region Porous Model—Axial k_{eff} (helium)

Temperature (Kelvin)	k_{eff} (W/m*K)
273	1.8833
400	2.1775
600	2.6166
800	3.0375
1000	3.4482
1100	3.6515

Table 2-8 BWR Fully Populated Cladding Region Porous Model—Radial k_{eff} (air)

Emissivity	Temperature (Kelvin)	k_{eff} (W/m*K)
0.2	290	0.1152
	412	0.2048
	545	0.3486
	662	0.5180
	805	0.7779
0.6	286	0.1307
	402	0.2555
	529	0.4804
	637	0.7554
	761	1.1660

Table 2-9 BWR Fully Populated Cladding Region Porous Model—Axial k_{eff} (air)

Temperature (Kelvin)	k_{eff} (W/m*K)
273	2.01
400	2.3141
600	2.7668
800	3.2027
1000	3.6312
1100	3.8419

Table 2-10 BWR Partially Populated Cladding Region Porous Model—Radial k_{eff} (air)

Temperature (Kelvin)	k_{eff} (W/m*K)
160	0.1109
375	0.2892
500	0.5067
600	0.7684

Table 2-11 BWR Partially Populated Cladding Region Porous Model—Axial k_{eff} (air)

Temperature (Kelvin)	k_{eff} (W/m*K)
273	1.8051
400	2.0773
600	2.4841
800	2.8759
1000	3.2609
1100	3.4506

2.3 Porous Media Equivalent Density, Specific Heat, and Frictional Coefficients

Porous media equivalent density and heat capacity based on the area ratio as a function of temperature was calculated. Table 2-12 through Table 2-14 show the corresponding values. NUREG-2208 [15] includes further details on how to calculate these values.

Table 2-12 Fuel Region Porous Media Equivalent Density for Helium and Air

Assembly Type	Porous Media Equivalent Density with Helium (kg/m^3)	Porous Media Equivalent Density with Air (kg/m^3) for sub-atmospheric (i.e. 0.3 kPa) cases
Fully Populated Region	1795	1795
Partially Populated Region	1609	1610

Table 2-13 Fuel Region Porous Media Equivalent Specific Heat Capacity for Helium and Air for the Fully Populated Region

Temperature (K)	Porous Media Equivalent Heat Capacity for Helium (J/kg*K)	Porous Media Equivalent Heat Capacity for Air (J/kg*K) for sub-atmospheric (i.e. 0.3 kPa) cases
200	635	635
400	716	716
600	780	780
800	818	843
1000	851	862

Table 2-14 Fuel Region Porous Media Equivalent Specific Heat Capacity for Helium and Air for the Partially Populated Region

Temperature (K)	Porous Media Equivalent Heat Capacity for Helium (J/kg*K)	Porous Media Equivalent Heat Capacity for Air (J/kg*K) for sub-atmospheric (i.e. 0.3 kPa) cases
200	634	633
400	714	714
600	778	778
800	816	840
1000	849	860

The assembly fuel rod region porous media equivalent frictional and inertial hydraulic losses were based on the previous analysis documented in NUREG-2208 [15]. To accomplish this, a comparison of a dry cask thermal response of a detailed explicit assembly to a porous media assembly was performed. The final friction coefficient, D value with units of ($1/m^2$), was obtained by comparing the mass flow rate of both the detailed and porous media assemblies. The D value is an input to porous media friction in the ANSYS Fluent software. The shear stress method [15] was used to calculate the porous media friction coefficient (D). This coefficient will be a function of both the pressure and the power (decay heat) existing in the assembly. NUREG-2152 [13] and NUREG-2208 [15] contain a detailed explanation for the D value. Table 2-15 summarizes the values used for this study.

Table 2-15 Fuel Region Porous Media Friction Coefficients

Power (kW)	Pressure (kPa)	Fully Populated Region ($1/m^2$)	Partially Populated Region ($1/m^2$)
5	800	547,621	220,420
2.5	800	549,788	223,614
1	800	553,702	224,276
0.5	800	548,373	220,820
5	450	521,189	208,967
2.5	450	531,401	212,937
1	450	535,105	213,951
0.5	450	531,894	205,897
5	100	440,019	185,496
2.5	100	451,461	188,543
1	100	458,445	190,401
0.5	100	455,873	189,644
1	0.3	397,371	174,218
0.5	0.3	397,737	174,377

Figure 1.4 and Figure 1.5 show where the honeycomb mesh was used in the DCS experiment to obtain uniform flow before hotwire measurements for both the aboveground and underground configurations. As the mesh was not explicitly modeled, the frictional and inertial pressure loss of the air flow through the inlet vents (entering, going through, and exiting the honeycomb

straighteners) were calculated. The calculated frictional and inertial flow resistance were used to define a porous media to model the presence of the honeycomb screen. An equivalent frictional D value of 2.7×10^{6} m^{-2} was obtained. NUREG-2152 [13] and NUREG-2208 [15] explain the D value in detail.

3 UNCERTAINTY QUANTIFICATION

Uncertainty quantification for the CFD models was obtained using ASME V&V 20-2009 [2] for the target variables of interest: PCT and air mass flow rate. Sources of uncertainty examined in the analysis include simulation input, numerical errors (i.e., iterative, discretization, and round-off), and experimental errors. ASME V&V 20-2009 explains the method used in this calculation in detail. NUREG/CR-7260 [7] undertakes similar work, which this report followed very closely.

UQ for PCT and air mass flow rate was performed for a total of 16 cases (i.e., 8 for aboveground and 8 for underground). These cases include (800 kPa, 5.0 kW), (800 kPa, 0.5 kW), (450 kPa, 2.5 kW), (100 kPa, 5.0 kW), (100 kPa, 2.5 kW), (100 kPa, 0.5 kW), (0.3 kPa, 1.0 kW), and (0.3 kPa, 0.5 kW) for both aboveground and underground configurations as illustrated in Table 4-1 thru Table 4-6. This chapter illustrates the UQ for the (800 kPa, 5.0 kW) aboveground case. The results sections and Appendix A include the UQ for the other cases.

As found in NUREG/CR-7260, “CFD Validation of Dry Cask Storage Systems,” issued May 2019 [7]:

3.1 Numerical Uncertainty

> Numerical uncertainty has three major sources: computer round-off error, iterative convergence uncertainty, and discretization uncertainty. Discretization uncertainty can be spatial or temporal but because this simulation is steady state, temporal uncertainty is not of concern. Because computer round-off error is extremely small compared to other sources, it is not considered here.

3.1.1 Iterative Uncertainty

> It is generally known among CFD practitioners that CFD models need to run until they are properly converged. A solution is converged when residuals and target variable monitors no longer vary with additional iterations. However, some solutions are stable and converge better and more easily than others, depending on the physics and the solver settings chosen. Some solutions converge as they are supposed to and change very little with each additional iteration; but some solutions are much “noisier,” and their solution can vary significantly within a range of values. This variation can be due to numerical instability in the solution, or due to physically based unsteady flow patterns in a steady-state solution.
>
> Once the solution reaches something resembling convergence, the output in question should be recorded for the last 2,000 to 3,000 iterations to determine the range of values over which the output changes. This range represents the iterative convergence uncertainty of a solution.

The PCT values for the baseline solution were recorded in each case for 2,000 iterations. Figure 3-1 represents the PCT iteration error, and Figure 3-2 shows the air inlet mass flow rate iteration error. The average PCT value was found to be 659.77 ± 0.008 kelvin (K) (728 ± 0.0144 degrees F) within a 95-percent confidence level, or within two standard deviations of the average value. The average air inlet mass flow rate was found to be $0.01525 \pm 1.5036\times10^{-7}$ kilograms/second (kg/s) ($0.03355 \pm 3.3079\times10^{-7}$ pounds/second (lb/s)) within a 95-percent confidence level, or within two standard deviations of the average value.

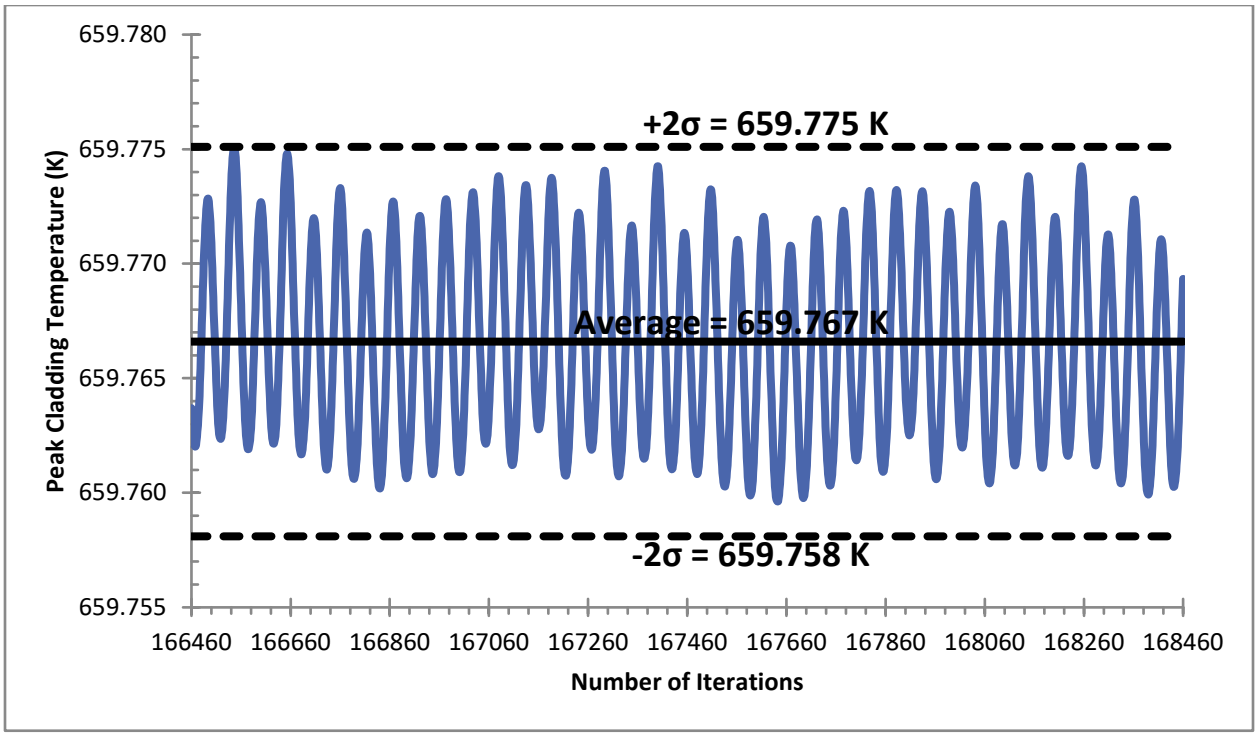

Figure 3-1 Iterative Convergence of PCT for the (800 kPa, 5 kW) Aboveground Case

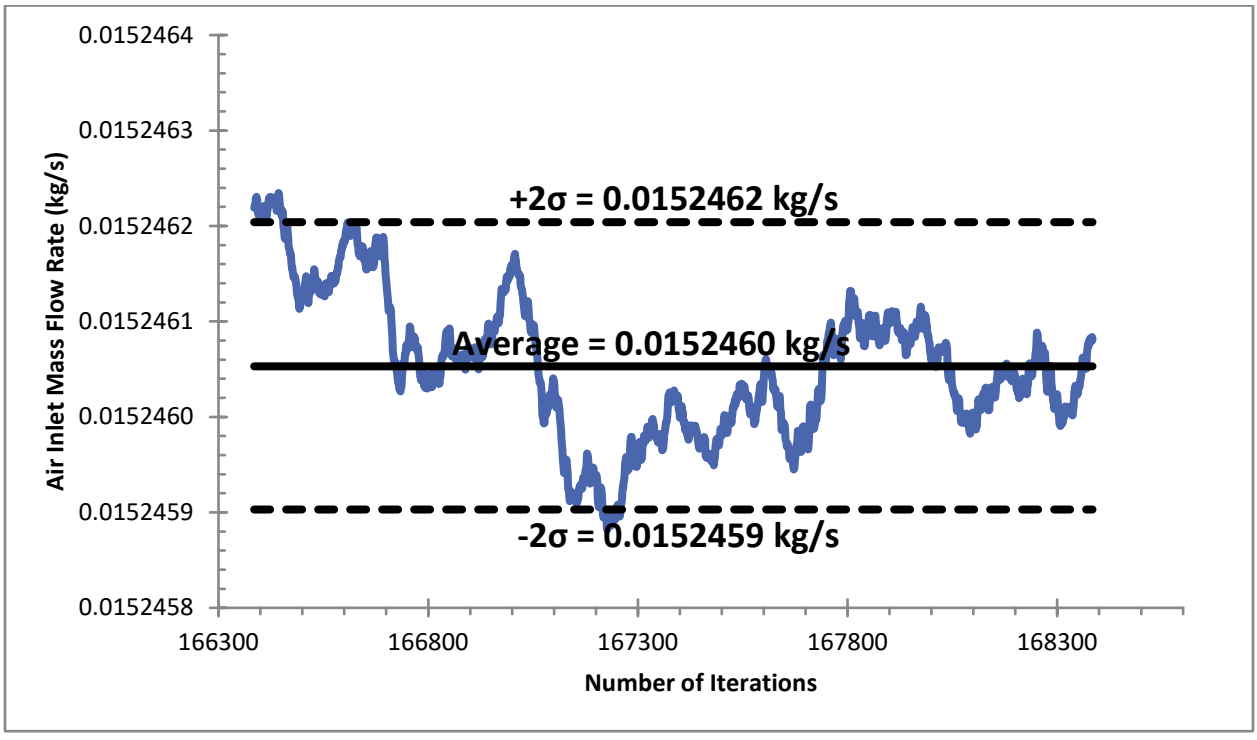

Figure 3-2 Iterative Convergence of $\dot{m}_{air}$ for the (800 kPa, 5 kW) Aboveground Case

The distribution of values gathered during the iterative convergence testing was plotted against a normal distribution to determine whether two standard deviations can safely be used as the 95-percent confidence level for the iterative convergence uncertainty. The data closely follow a normal distribution, as shown in Figure 3-3 and Figure 3-4, so this is a valid assumption.

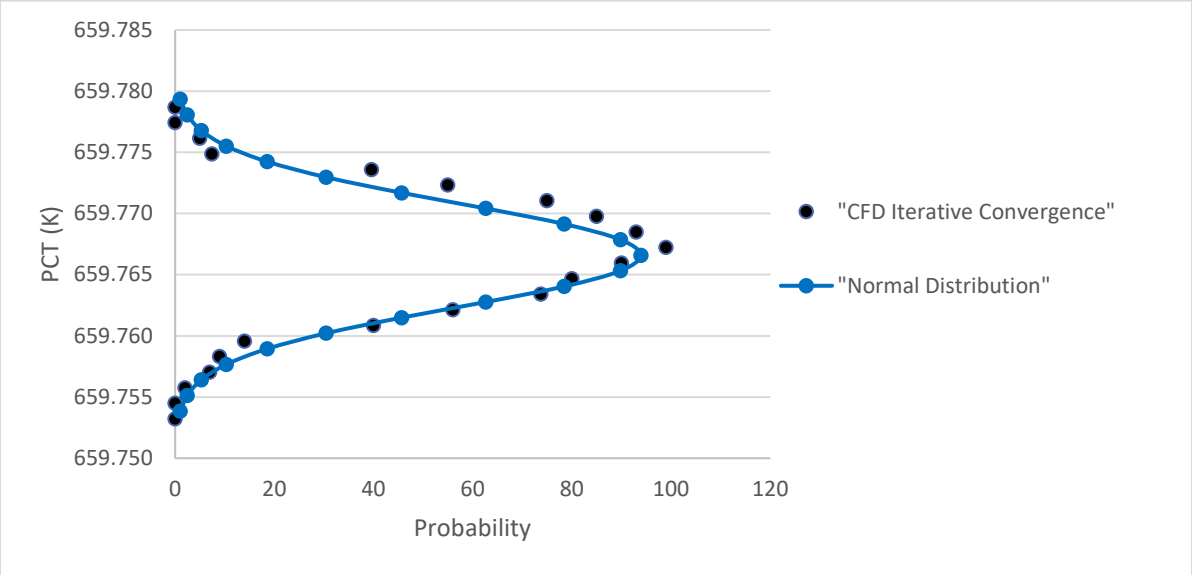

Figure 3-3 Normal Distribution and PCT Iterative Convergence for the (800 kPa, 5 kW) Aboveground Case

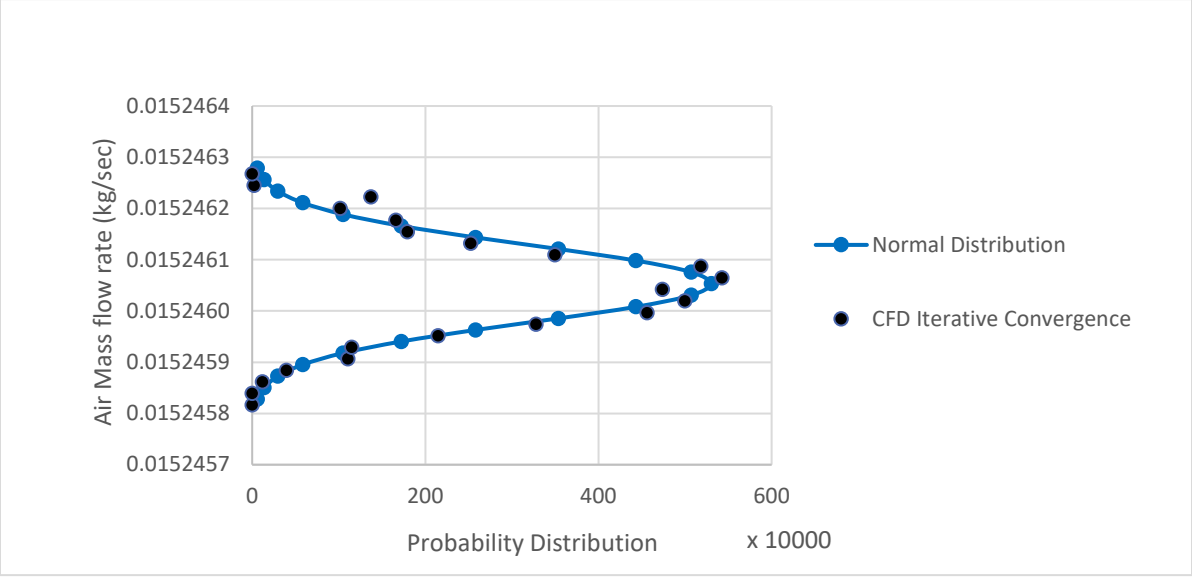

Figure 3-4 Normal Distribution and $\dot{m}_{air}$ Iterative Convergence Comparison for the (800 kPa, 5 kW) Aboveground Case

The iterative uncertainties of ±0.008 K (±0.0144 degrees F) and 1.5036×10^{-7} kg/s (± 3.3079×10^{-7} lb/s) are very small compared to the temperature and air mass flow rate ranges of interest, as well as other sources of error in this analysis.

3.1.2 Discretization Uncertainty

The GCI, as outlined in ASME V&V 20-2009 [2], recommends using at least three grids to determine the uncertainty of a solution with respect to the mesh. This case uses a fine, a medium, and a coarse mesh, where each level of refinement is accomplished by doubling the mesh resolution (Table 3-1).

Table 3-1 GCI Mesh Sizes

Mesh #	GCI Mesh Size	Three-Dimensional Cells
1	Fine	823,280
2	Medium	353,598
3	Coarse	160,108

The GCI, which is the 95-percent confidence level uncertainty in the solution as a result of the mesh, can be calculated for the finest of three meshes as follows:

$$GCI_{fine} = \frac{F_s * |\varphi_2 - \varphi_1|}{r_{21}^p - 1}$$

Where ϕ is the solution result, and 1, 2, and 3 represent the fine, medium, and coarse meshes respectively. F_s is an empirically derived factor of safety, which is 1.25 for an asymptotically converging set of three or more meshes. r_{21} is the refinement ratio of fine mesh cells to medium mesh cells, r_{32} is the refinement ratio of medium mesh cells to coarse mesh cells. The order of accuracy "*p*" can be calculated as follows:

$$p = \frac{\ln\left(\frac{\varphi_3 - \varphi_2}{\varphi_2 - \varphi_1}\right) + q(p)}{\ln(r_{21})}$$

Where *q*(*p*) is defined as:

$$q(p) = ln\ \frac{r_{21}^p - s}{r_{32}^p - s}$$

And *s* is defined as:

$$s = 1 * sign\frac{\varphi_3 - \varphi_2}{\varphi_2 - \varphi_1}$$

Because the medium mesh is used for all evaluations outside of the grid refinement study, it is also useful to calculate the GCI of the medium mesh, as follows:

$$GCI_{medium} = GCI_{fine} * r_{21}^p$$

Calculating the GCI using this Richardson Extrapolation method only works when the successive refinement results in a solution that asymptotically converges towards a fixed value at a cell size of zero.

To achieve a meaningful GCI, ASME V&V 20-2009 [2] highly recommends using a systematic grid refinement (i.e., constant refinement ratio throughout the computational volume), geometrically similar cells in each refinement level, and structured cells where possible. This was a challenge, as it is for many problems. A grid refinement ratio higher than 1.3 was used as recommended by ASME V&V 20-2009. A systematic grid refinement was achieved for a majority of the refinements but not for all. Additionally, to apply the GCI method, the grid refinement should be in the asymptotic region. It should also be noted that the calculated value of order of accuracy *p* should not be significantly different than the formal value of *p* (i.e., the order of the method). If any of these conditions are not met, an F_s of 3 should be used.

If either asymptotic behavior did not demonstrate asymptotic convergence with the three meshes used, particularly in areas of strong temperature gradients, ASME V&V 20-2009 [2] suggests that four or more mesh resolutions should be used to convincingly demonstrate asymptotic response in difficult problems. However, the computational resources necessary to perform another refinement of mesh resolution were prohibitive.

At measurement locations that did not obey asymptotic convergence, GCI was calculated from just two mesh resolutions: the medium mesh and the coarse mesh. In this situation, ASME V&V 20-2009 suggests using a factor of safety of 3.0 to account for the greater uncertainty associated with using only two mesh refinement levels, and an order of convergence $p = 1$. This allows the GCI to be calculated everywhere in the mesh so that the discretization uncertainty can be included in the overall uncertainty when comparing simulation results to experimental measurements at all the temperature measurement locations.

For the PCT and air mass flow rate that obey asymptotic convergence, the three-mesh method was used to determine the discretization uncertainty. At locations where grid refinement did not obey asymptotic convergence, the two-mesh method was used.

Table 3-2 and Table 3-3 illustrate the GCI calculations for the PCT and air mass flow rate for the aboveground (800 kPa, 5 kW) case. In this case F_s equal to 3 was used, as the calculated order of accuracy p was different than the formal order of accuracy.

Table 3-2 GCI Values for PCT for the (800 kPa, 5 kW) Aboveground Case

GCI for PCT:	**Three Mesh GCI**	**Two Mesh GCI**
Refinement Ratio, r_{21}	1.33	
Refinement Ratio, r_{32}	1.3	
Factor of Safety, Fs	3	
Coarse Mesh	659 K (726.5 °F)	
Medium Mesh	659.8 K (728 °F)	
Fine Mesh	659.9 K (728.2 °F)	
Order of Convergence, *p*	6.19	1
GCI	0.6 K (1 °F)	1.8 K (3.3 °F)

Table 3-3 GCI Values for $\dot{m}_{air}$ for the (800 kPa, 5 kW) Aboveground Case

GCI for air mass flow rate:	3-Mesh GCI	2-Mesh GCI
Refinement Ratio, r_{21}	1.33	
Refinement Ratio, r_{32}	1.3	
Factor of Safety, Fs	3	
Coarse Mesh	1.52×10^{-2} kg/s (3.34×10^{-2} lb/s)	
Medium Mesh	1.53×10^{-2} kg/s (3.35×10^{-2} lb/s)	
Fine Mesh	1.53×10^{-2} kg/s (3.36×10^{-2} lb/s)	
Order of Convergence, *p*	2.5	1
GCI	1.44×10^{-4} kg/s (3.16×10^{-4} lb/s)	2.93×10^{-4} kg/s (6.45×10^{-4} lb/s)

3.1.3 Overall Numerical Uncertainty on Peak Cladding Temperature and Air Mass Flow Rate

Table 3-4 presents the overall numerical uncertainty from all sources for the (800 kPa, 5 kW) aboveground scenario. When computing the total numerical uncertainty, it is not sufficient to use the root mean square addition of iterative convergence error and discretization error, because the two errors are correlated [2]. Instead, they must be combined using simple addition. Appendix A to this report tabulates the results for other scenarios.

Table 3-4 Overall Numerical Uncertainty for PCT and $\dot{m}_{air}$ for the (800 kPa, 5 kW) Aboveground Case

	PCT	Air inlet mass flow rate ($\dot{m}_{air}$)
Computer Round-off	± 0.0 K (± 0.0°F)	0 kg/s (± 0 lb/s)
Iterative Convergence	± 0.008 K (± 0.014°F)	1.50×10^{-7} kg/s (± 3.31×10^{-7} lb/s)
Discretization (GCI)	± 1.8 K (± 3.3°F)	2.93×10^{-4} kg/s (± 6.45×10^{-4} lb/s)
Numerical Uncertainty	± 1.8 K (± 3.3°F)	2.93×10^{-4} kg/s (± 6.46×10^{-4} lb/s)

3.2 Input Uncertainty

The input uncertainty method used was the finite difference method (also variously called the sensitivity coefficient method, perturbation method, mean value method, and possibly others). This is a local approach to determining the input uncertainty, whereby an independent input variable (e.g., total decay heat) is changed by a small amount, and the effect that this variable has on the solution is recorded. If the uncertainty of the input is known, then the resulting uncertainty on the solution due to the uncertainty of the input can be calculated using the following equation:

$$u_{input}{}^2 = \sum_{i=1}^{n} \left(\frac{\partial S}{\partial X_i} u_{X_i} \right)^2$$

Where:

u_{input} =	Total input uncertainty
S =	Simulation result
u_{X_i} =	Corresponding standard uncertainty in input parameter X_i
X_i =	Input parameter
n =	Number of inputs in the sensitivity study
$\partial S/\partial X_i$ =	Sensitivity coefficient

Each input variable was perturbed both up and down by its uncertainty value, so two separate cases were run for each input variable, in addition to the baseline case.

This method only works in the local neighborhood around the baseline solution, and only as long as the solution is fairly linear with respect to the inputs in that neighborhood. There are more complex global methods of determining uncertainty (e.g., Monte Carlo, Latin Hypercube), but they typically require more knowledge of the probability distribution of the input variables than are generally available and, with a large number of input variables, require hundreds or perhaps thousands of cases to achieve statistical significance. Table 3-5 and Table 3-6 provide the range for each parameter and the total input uncertainty for the PCT and air mass flow rate, respectively.

Twelve input variables were used to quantify the uncertainty for the PCT and inlet air mass flow rate. The geometry in this validation was well described and controlled, as such fluid gaps were not among the input variables to quantify the uncertainty. This simulation has a large number of inputs, so several other variables could also have been evaluated, but the uncertainty in these input values was deemed to be of minor importance to the overall simulation uncertainty. Table 3-5 and Table 3-6 list the input variables that were evaluated, along with their associated contribution to the uncertainty on PCT and air mass flow rate, respectively.

The input variables were assumed to be uncorrelated, so the total input uncertainty was calculated as the root mean square of all the individual input uncertainties in each column. Table 3-5 and Table 3-6 describe each input variable, its baseline value, and its associated uncertainty for the PCT and air mass flow rate, respectively.

Table 3-5 Input Uncertainty of PCT for the (800 kPa, 5 kW) Aboveground Case

Input Parameters	Units:	Baseline Input Value:	Uncertainty of Input:	Lower PCT Output (K):	Upper PCT Output (K):	Uncertainty of PCT ± (K)
External Heat Transfer Coefficient	% h	h	0.3	660.2	659.4	0.4
Ambient Temperature	(K)	300	3	657.8	661.7	2.0
Kaowool Emissivity	(-)	0.9	0.1	660.1	659.8	0.2
Carbon Steel Emissivity	(-)	0.67	0.07	666.9	653.2	6.9
Zirc Emissivity	% ε-zirc	ε-zirc	0.20	662.4	657.6	2.4
Fuel Bundle Porous Resistance	% D-fuel	D-fuel	0.1	658.1	661.0	1.5
Fuel Radial Thermal Conductivity	% K-eff-rad	K-eff-rad	0.1	666.1	654.4	5.8
Fuel Axial Thermal Conductivity	% K-eff-ax	K-eff-ax	0.20	660.0	659.6	0.2
Helium Pressure	Pa	800,000	1000	659.8	659.7	0.0
Ambient Pressure	Pa	84,000	110	659.8	659.7	0.1
Total Decay Heat	Watts	5000	75	656.3	663.2	3.5
Honeycomb Porous Resistance	% D-H	D-H	0.100	659.5	660.0	0.3
			Total Input Uncertainty (K):			**10.2**

Table 3-6 Input Uncertainty of $\dot{m}_{air}$ for the (800 kPa, 5 kW) Aboveground Case

Input Parameters	Units:	Baseline Input Value:	Uncertainty of Input:	Lower $\dot{m}_{air}$ (kg/sec)	Upper $\dot{m}_{air}$ (kg/sec)	Uncertainty of $\dot{m}_{air}$ ± (kg/sec)
External Heat Transfer Coefficient	% h	h	0.3	1.53×10^{-2}	1.52×10^{-2}	4.45×10^{-5}
Ambient Temperature	(K)	300	3	1.55×10^{-2}	1.50×10^{-2}	2.52×10^{-4}
Kaowool Emissivity	(-)	0.9	0.1	1.53×10^{-2}	1.52×10^{-2}	2.25×10^{-5}
Carbon Steel Emissivity	(-)	0.67	0.07	1.53×10^{-2}	1.52×10^{-2}	8.00×10^{-5}
Zirc Emissivity	% ε-zirc	ε-zirc	0.20	1.52×10^{-2}	1.53×10^{-2}	3.20×10^{-5}
Fuel Bundle Porous Resistance	% D-fuel	D-fuel	0.1	1.52×10^{-2}	1.53×10^{-2}	3.10×10^{-5}
Fuel Radial Thermal Conductivity	% K-eff-rad	K-eff-rad	0.1	1.52×10^{-2}	1.52×10^{-2}	3.65×10^{-5}
Fuel Axial Thermal Conductivity	% K-eff-ax	K-eff-ax	0.20	1.52×10^{-2}	1.52×10^{-2}	1.00×10^{-6}
Helium Pressure	Pa	800,000	1000	1.52×10^{-2}	1.52×10^{-2}	1.00×10^{-6}
Ambient Pressure	Pa	84,000	110	1.52×10^{-2}	1.53×10^{-2}	1.65×10^{-5}
Total Decay Heat	Watts	5000	75	1.51×10^{-2}	1.53×10^{-2}	9.85×10^{-5}
Honeycomb Porous Resistance	% D-H	D-H	0.100	1.57×10^{-2}	1.48×10^{-2}	4.31×10^{-4}
					Total Input Uncertainty (kg/sec):	5.21×10^{-4}

3.3 Simulation Uncertainty Quantification

The total simulation uncertainty is a combination of the numerical uncertainty and the input uncertainty, presented in Table 3-7. These calculations of simulation uncertainty were repeated for all the cases for PCT and air mass flow rate. These simulation uncertainties are the basis for the errors calculated on the baseline simulation result, which are compared to experimental results with associated experimental uncertainties.

Table 3-7 Simulation Uncertainty for PCT and $\dot{m}_{air}$ for the (800 kPa, 5 kW) Aboveground Case

	PCT	$\dot{m}_{air}$
Numerical Uncertainty	± 1.5 K (2.7 °F)	±2.93x10^{-4} kg/s (6.45x10^{-4} lb/s)
Input Uncertainty	±10.3 K (18.4 °F)	±5.21x10^{-4} kg/s (11.46x10^{-4} lb/s)
Simulation Uncertainty	±10.4 K (18.7 °F)	±1.2x10^{-3} kg/s (2.63x10^{-3} lb/s)

3.4 Experimental Uncertainty

The uncertainty and error inherent in an experimental result are critical for accurately interpreting the data. Therefore, this section provides estimates of the uncertainties in the experimental measurements. The general description of the method used and an explanation of the source of each reported measurement uncertainty are described NUREG/CR-7250 [6].

As described in NUREG/CR-7250 [6]:

> The overall standard uncertainty of an indirect measurement *y*, dependent on *N* indirect measurements x_i, is defined below. The standard uncertainty associated with an indirect measurement is analogous to the standard deviation of a statistical population.
>
> $$u^2 = \sum_{i=1}^{N} \left(\frac{\partial y}{\partial x_i} u_i \right)^2$$
>
> Here, *u* is used to define the standard uncertainty of a measurement. The expanded uncertainty, *U*, is reported in NUREG/CR-7250 [6] and defines the bounds that include 95 percent of the possible data. The expanded uncertainty is assumed to be defined as the product of the standard uncertainty and the Student's *t*-value. All uncertainty measurements are assumed to be based on a Student's *t*-distribution with no fewer than 30 measurements. The associated *t*-value for 95-percent intervals is 2.0 for 29 degrees of freedom. Therefore, the equation below shows the definition of the expanded uncertainty as used in the following sections for a 95-percent confidence interval.
>
> *U = t-value u*

Table 3-8 summarizes the expanded uncertainty for each measurement used in this report. NUREG/CR-7250 [6] includes further details.

Table 3-8 Summary of the Expanded Uncertainty Determined for Each Measurement

Measurement, x	Units	Expanded Uncertainty, U_x
Peak Cladding Temperature	K	7
Ambient Temperature	K	3
Ambient Pressure	kPa, abs	1.1×10^{-1}
Helium Pressure	kPa, abs	1
Vacuum	kPa, abs	3.0×10^{-1}
Voltage	V	3.8×10^{-1}
Current	A	3.8×10^{-1}
Power	kW	7.5×10^{-2}
Forced Air Mass Flow Rate	Kg/s	5.9×10^{-4}
Induced Air Mass Flow Rate (Aboveground)	Kg/s	1.5×10^{-3}
Induced Air Mass Flow Rate (Underground)	Kg/s	1.1×10^{-3}
Induced Air Mass Flow Rate (Crosswind)	Kg/s	1.3×10^{-3}
Normalized Air Mass Flow Rate, ($\dot{m}/\dot{m}_o$)	_	5.6×10^{-2}
Crosswind Speed	m/s	4.9×10^{-2}

3.5 Validation Uncertainty Quantification

The total validation uncertainty is a combination of the numerical uncertainty, the input uncertainty, and the experimental uncertainty, presented in Table 3-9. These calculations of validation uncertainty were repeated for all the cases for PCT and air mass flow rate.

Table 3-9 Total Validation Uncertainty for PCT and $\dot{m}_{air}$ for the (800 kPa, 5 kW) Aboveground Case

	PCT	$\dot{m}_{air}$
Numerical Uncertainty	± 1.5 K (2.7 °F)	$\pm 2.93 \times 10^{-4}$ kg/s ($6.45 \text{Ex} 10^{-4}$ lb/s)
Input Uncertainty	±10.3 K (18.45 °F)	$\pm 5.21 \times 10^{-4}$ kg/s (11.46×10^{-4} lb/s)
Experimental Uncertainty	± 7 K (12.6 °F)	$\pm 1.510^{-3}$ kg/s (3.3×10^{-3} lb/s)
Validation Uncertainty	± 12.5 K (22.6°F)	$\pm 1.90 \times 10^{-3}$ kg/s (4.19×10^{-3} lb/s)

4 RESULTS AND DISCUSSIONS

4.1 Aboveground Dry Cask Simulator Computational Fluid Dynamics Model Validation Results

For the aboveground DCS configuration, CFD analyses were performed for 14 cases in which the DCS achieved steady state for various assembly powers and pressures. The power levels tested were 0.5, 1.0, 2.5, and 5.0 kW. The vessel pressures tested were sub-atmospheric (i.e., 0.3 kPa), 100, 450, and 800 kPa absolute. CFD was performed for all 14 cases. On the other hand, UQ for PCT and air mass flow rate was performed for eight cases, including (800 kPa, 5 kW), (800 kPa, 0.5kW), (450 kPa, 2.5 kW), (100 kPa, 5 kW), (100 kPa, 2.5 kW), (100 kPa, 0.5 kW), (0.3 kPa, 1 kW), and (0.3 kPa, 0.5 kW) cases.

This section presents four cases (800 kPa, 5 kW), (800 kPa, 0.5 kW), (100 kPa, 5 kW), and (100 kPa, 0.5 kW). Appendices A1 and B1 present the other four cases.

Table 4-1 through Table 4-3 summarize the aboveground results for PCT and air mass flow rate, including the UQ.

Table 4-1 PCT and $\dot{m}_{air}$ for Aboveground Cases

P (kPa)	Power (kW)	CFD		Experiment		Δ (CFD-Experiment)	
		PCT (K)	$\dot{m}_{air}$ (kg/s)	PCT (K)	$\dot{m}_{air}$ (kg/s)	Δ PCT (K)	Δ $\dot{m}_{air}$ (kg/s)
800	0.5	360	2.19×10^{-2}	359	2.21×10^{-2}	1	-2.25×10^{-4}
800	1	405	3.05×10^{-2}	410	3.1×10^{-2}	-5	-4.58×10^{-4}
800	2.5	517	4.57×10^{-2}	521	4.69×10^{-2}	-4	-1.15×10^{-3}
800	5	659	6.1×10^{-2}	659	6.26×10^{-2}	0	-1.61×10^{-3}
450	0.5	367	2.31×10^{-2}	367	2.41×10^{-2}	0	-9.75×10^{-4}
450	1	422	3.13×10^{-2}	426	3.28×10^{-2}	-4	-1.50×10^{-3}
450	2.5	545	4.74×10^{-2}	545	4.76×10^{-2}	0	-2.48×10^{-4}
450	5	691	6.51×10^{-2}	689	6.55×10^{-2}	2	-4.2×10^{-4}
100	0.5	376	2.58×10^{-2}	376	2.64×10^{-2}	0	-6.06×10^{-4}
100	1	435	3.55×10^{-2}	434	3.53×10^{-2}	1	1.92×10^{-4}
100	2.5	563	5.28×10^{-2}	570	5.31×10^{-2}	-7	-3.2×10^{-4}
100	5	707	6.92×10^{-2}	715	6.89×10^{-2}	-8	3.4×10^{-4}
0.3	0.5	448	2.57×10^{-2}	458	2.53×10^{-2}	-10	4.27×10^{-4}
0.3	1	536	3.48×10^{-2}	549	3.51×10^{-2}	-13	-3.22×10^{-4}

Table 4-2 PCT Uncertainty Quantification for Aboveground Cases

P (kPa)	Power (kW)	PCT (K)		Δ PCT (K) (CFD-Experiment)	Uncertainty (K)		
		CFD	Experiment		Experiment	Simulation	Validation
800	0.5	360	359	1	7	8	10.6
800	1	405	410	-5	7		
800	2.5	517	521	-4	7		
800	5	659	659	0	7	10.4	12.5
450	0.5	367	367	0	7		
450	1	422	426	-4	7		
450	2.5	545	545	0	7	8.7	11.1
450	5	691	689	2	7		
100	0.5	376	376	0	7	10.3	12.4
100	1	435	434	1	7		
100	2.5	563	570	-7	7	9.3	11.7
100	5	707	715	-8	7	11.7	13.6
0.3	0.5	448	458	-10	7	16.7	18.1
0.3	1	536	549	-13	7	13.8	15.5

Table 4-3 $\dot{m}_{air}$ Uncertainty Quantification for Aboveground Cases

P (kPa)	Power (kW)	$\dot{m}_{air}$ (kg/sec)		Δ $\dot{m}_{air}$ (kg/sec) (CFD-Experiment)	$\dot{m}_{air}$ Uncertainty (kg/sec)		
		CFD	Experiment		Experiment	Simulation	Validation
800	0.5	2.19×10^{-2}	2.21×10^{-2}	-2.25×10^{-4}	1.5×10^{-3}	9.31×10^{-4}	1.75×10^{-3}
800	1	3.05×10^{-2}	3.1×10^{-2}	-4.58×10^{-4}	1.5×10^{-3}		
800	2.5	4.57×10^{-2}	4.69×10^{-2}	-1.15×10^{-3}	1.5×10^{-3}		
800	5	6.1×10^{-2}	6.26×10^{-2}	-1.61×10^{-3}	1.5×10^{-3}	1.2×10^{-3}	1.90×10^{-3}
450	0.5	2.31×10^{-2}	2.41×10^{-2}	-9.75×10^{-4}	1.5×10^{-3}		
450	1	3.13×10^{-2}	3.28×10^{-2}	-1.50×10^{-3}	1.5×10^{-3}		
450	2.5	4.74×10^{-2}	4.76×10^{-2}	-2.48×10^{-4}	1.5×10^{-3}	5.23×10^{-4}	1.57×10^{-3}
450	5	6.51×10^{-2}	6.55×10^{-2}	-4.2×10^{-4}	1.5×10^{-3}		
100	0.5	2.58×10^{-2}	2.64×10^{-2}	-6.06×10^{-4}	1.5×10^{-3}	1.03×10^{-3}	1.80×10^{-3}
100	1	3.55×10^{-2}	3.53×10^{-2}	1.92×10^{-4}	1.5×10^{-3}		
100	2.5	5.28×10^{-2}	5.31×10^{-2}	-3.2×10^{-4}	1.5×10^{-3}	5.97×10^{-4}	1.6×10^{-3}
100	5	6.92×10^{-2}	6.89×10^{-2}	3.4×10^{-4}	1.5×10^{-3}	1.24×10^{-3}	1.93×10^{-3}
0.3	0.5	2.57×10^{-2}	2.53×10^{-2}	4.27×10^{-4}	1.5×10^{-3}	1.089×10^{-3}	1.84×10^{-3}
0.3	1	3.48×10^{-2}	3.51×10^{-2}	-3.22×10^{-4}	1.5×10^{-3}	1.02×10^{-3}	1.8×10^{-3}

Sections 4.1.1 through 4.1.4 show plots for temperature profiles as function of height for maximum fuel temperature including PCT in the assembly, channel box, basket, pressure vessel, shell1, and shell1-insulation. The PCT validation uncertainty bar is shown at all PCT locations.

4.1.1 Aboveground (800 kPa, 5 kW) Case

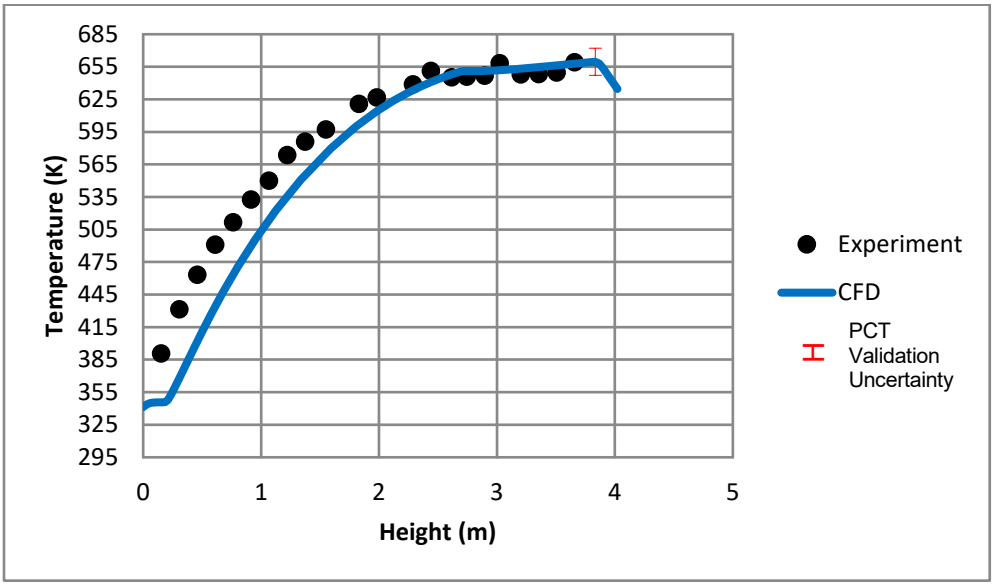

Figure 4-1 PCT for the Aboveground (800 kPa, 5 kW) Case

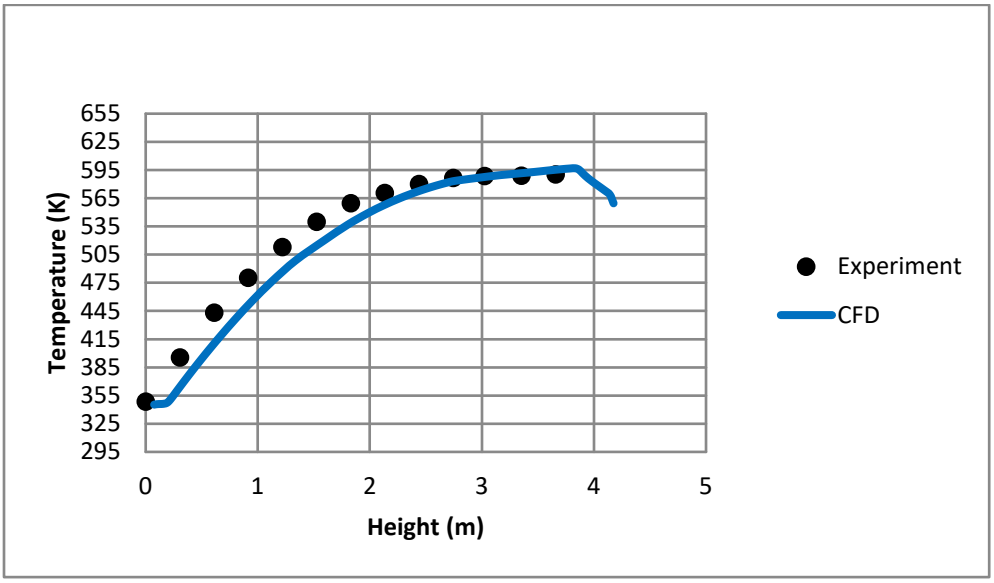

Figure 4-2 Channel Box Temperature for the Aboveground (800 kPa, 5 kW) Case

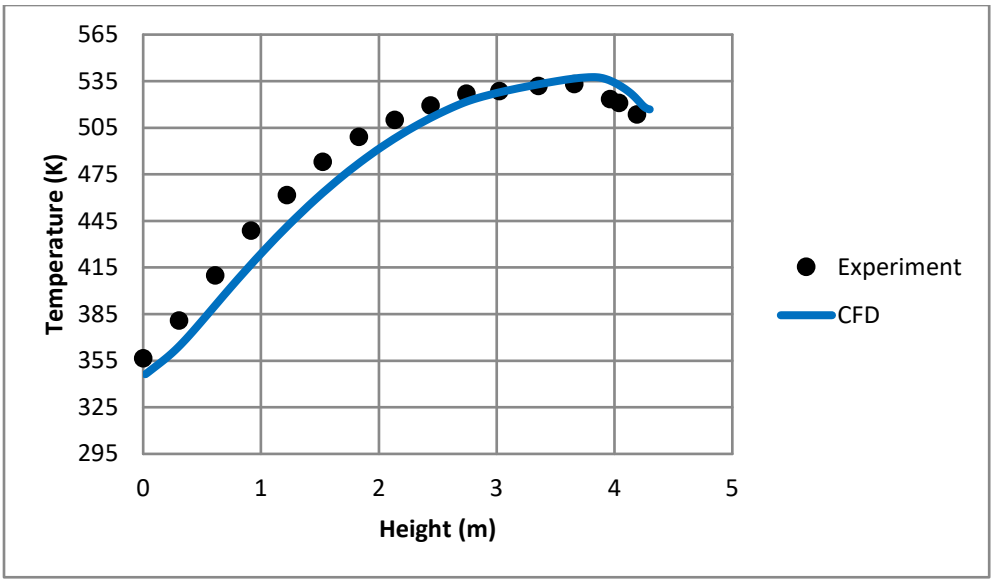

Figure 4-3 Basket Temperature for the Aboveground (800 kPa, 5 kW) Case

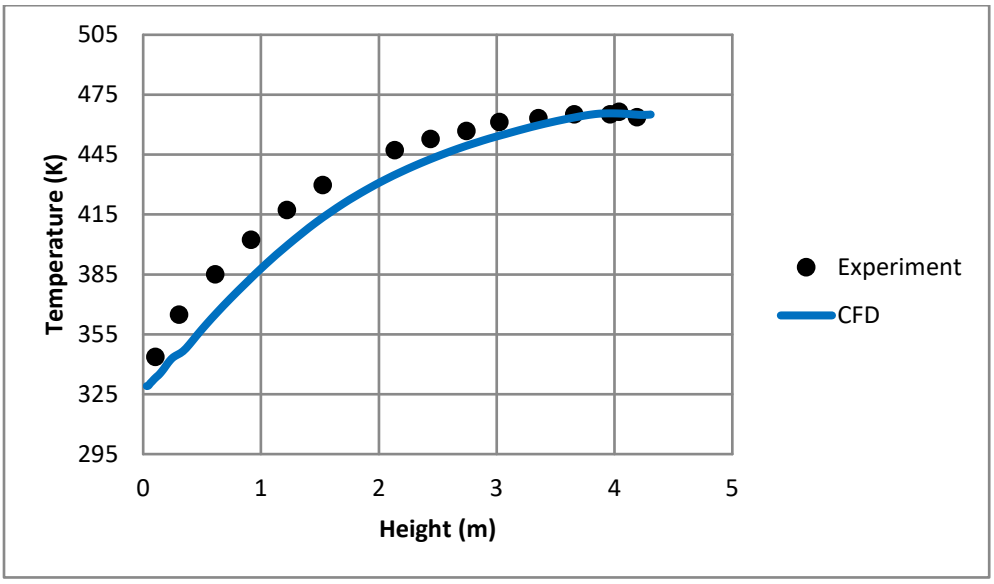

Figure 4-4 Pressure Vessel Temperature for the Aboveground (800 kPa, 5 kW) Case

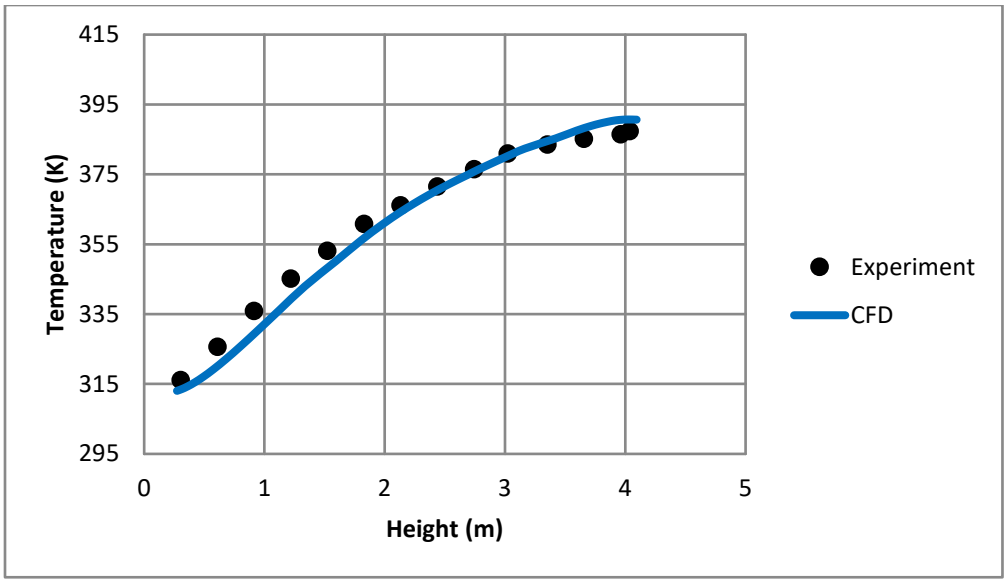

Figure 4-5 Shell1 Temperature for the Aboveground (800 kPa, 5 kW) Case

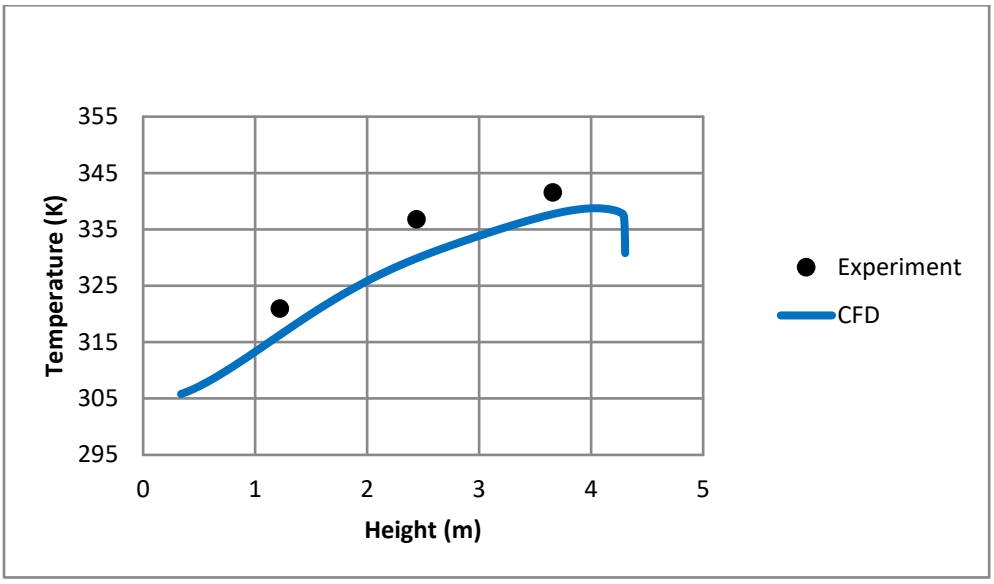

Figure 4-6 Shell1-Insulation Temperature for the Aboveground (800 kPa, 5 kW) Case

4.1.2 Aboveground (800 kPa, 0.5 kW) Case

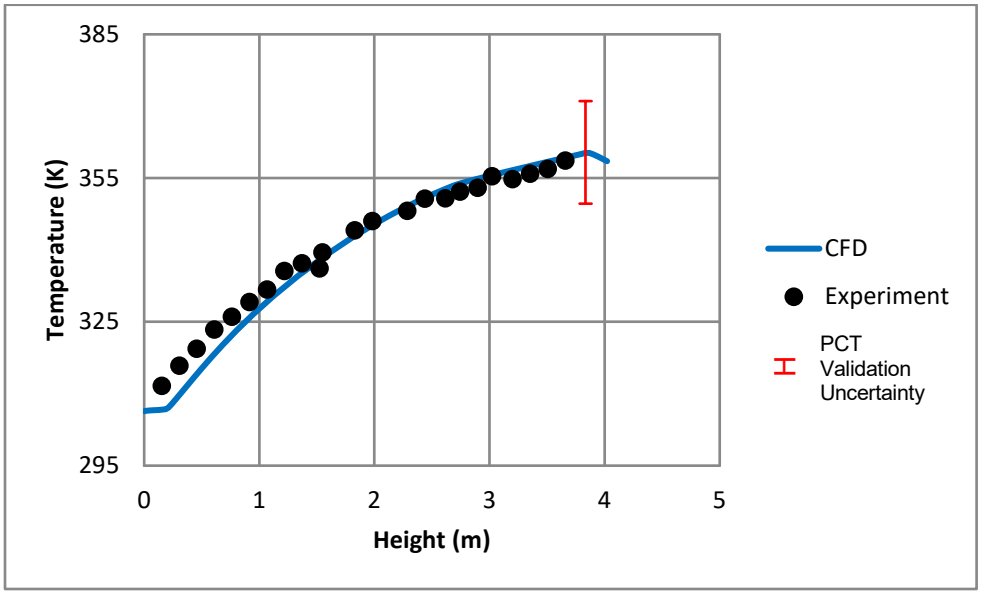

Figure 4-7 PCT for the Aboveground (800 kPa, 0.5 kW) Case

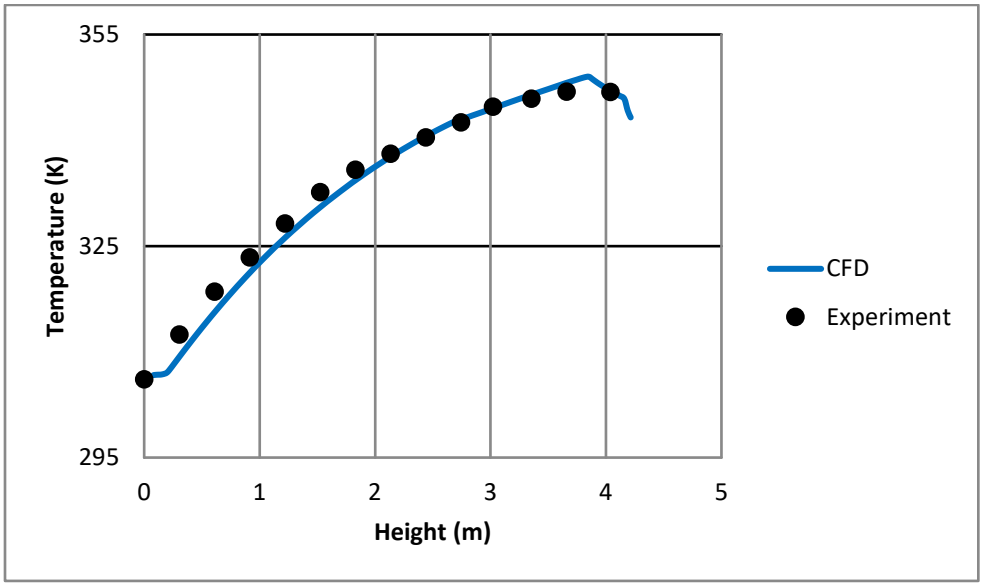

Figure 4-8 Channel Box Temperature for the Aboveground (800 kPa, 0.5 kW) Case

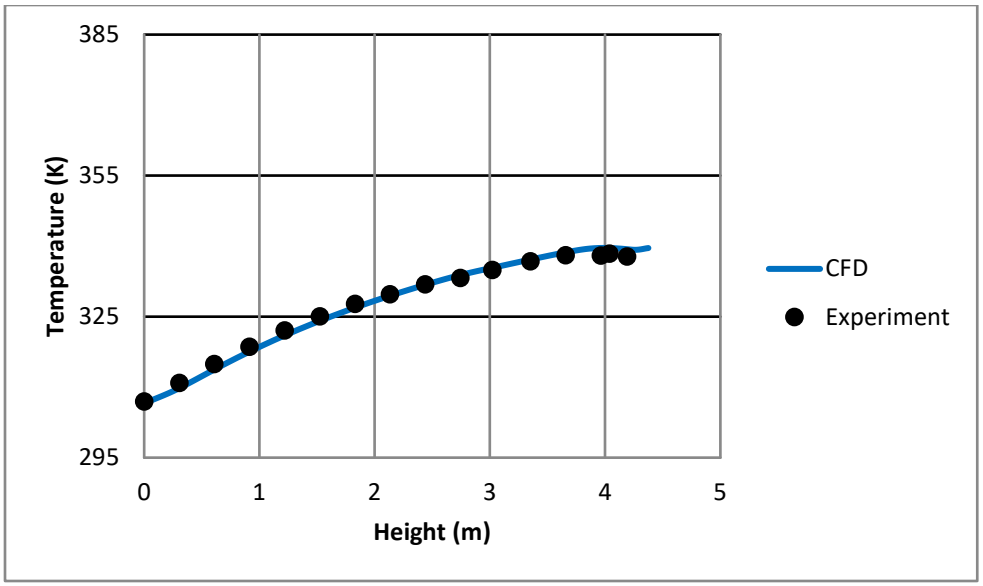

Figure 4-9 Basket Temperature for the Aboveground (800 kPa, 0.5 kW) Case

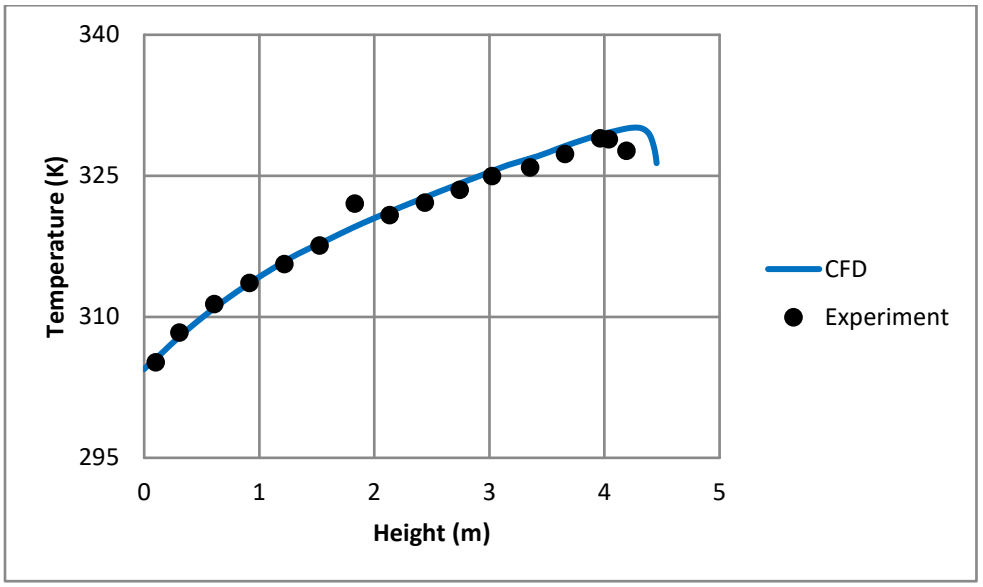

Figure 4-10 Pressure Vessel Temperature for the Aboveground (800 kPa, 0.5 kW) Case

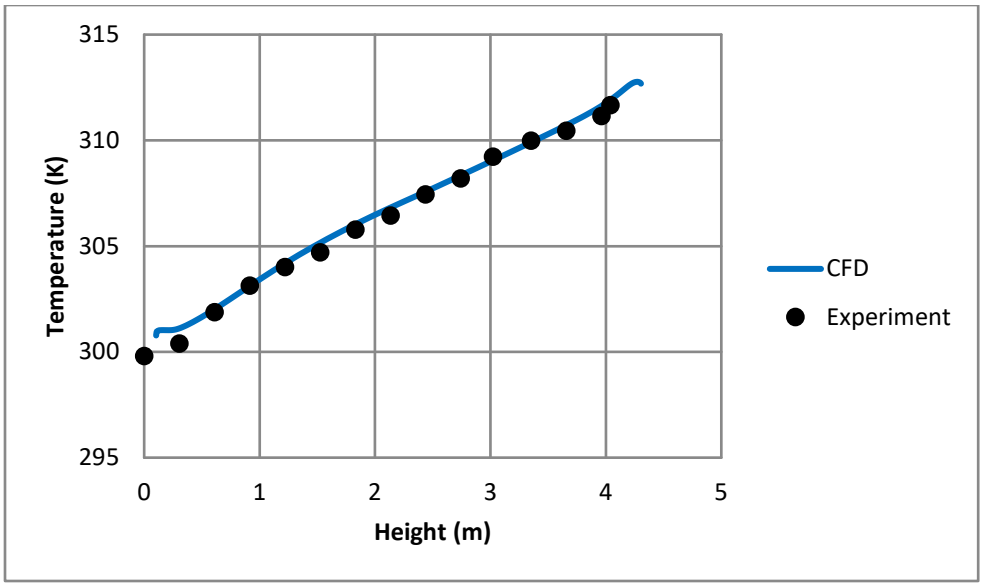

Figure 4-11 Shell1 Temperature for the Aboveground (800 kPa, 0.5 kW) Case

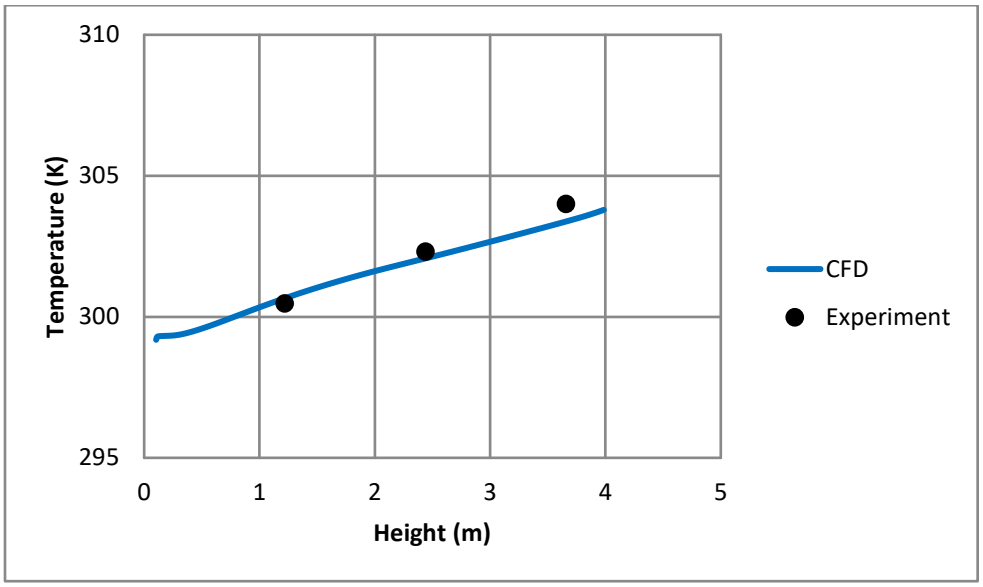

Figure 4-12 Shell1-Insulation Temperature for the Aboveground (800 kPa, 0.5 kW) Case

4.1.3 Aboveground (100 kPa 5 kW) Case

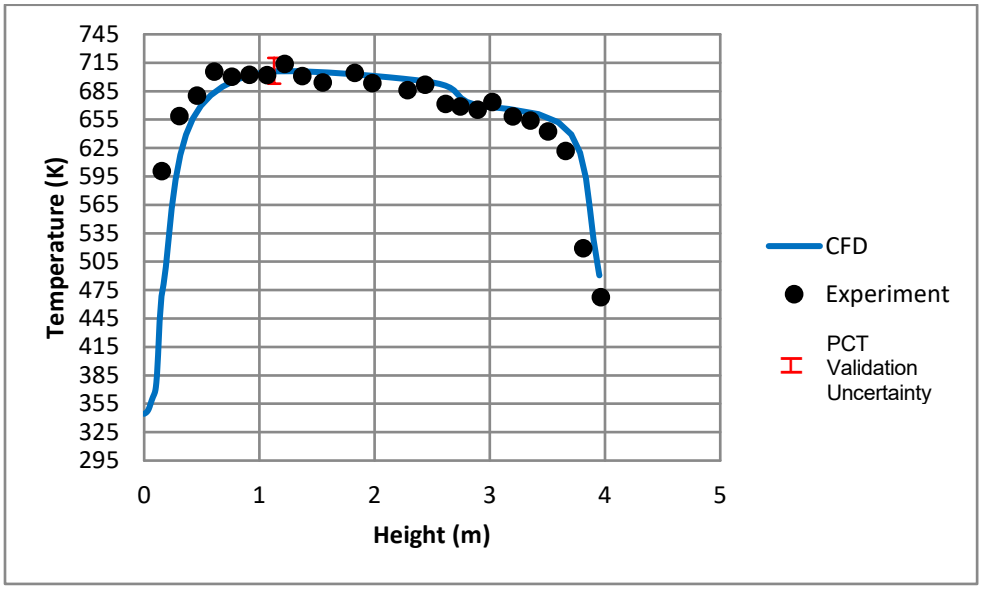

Figure 4-13 PCT for the Aboveground (100 kPa, 5 kW) Case

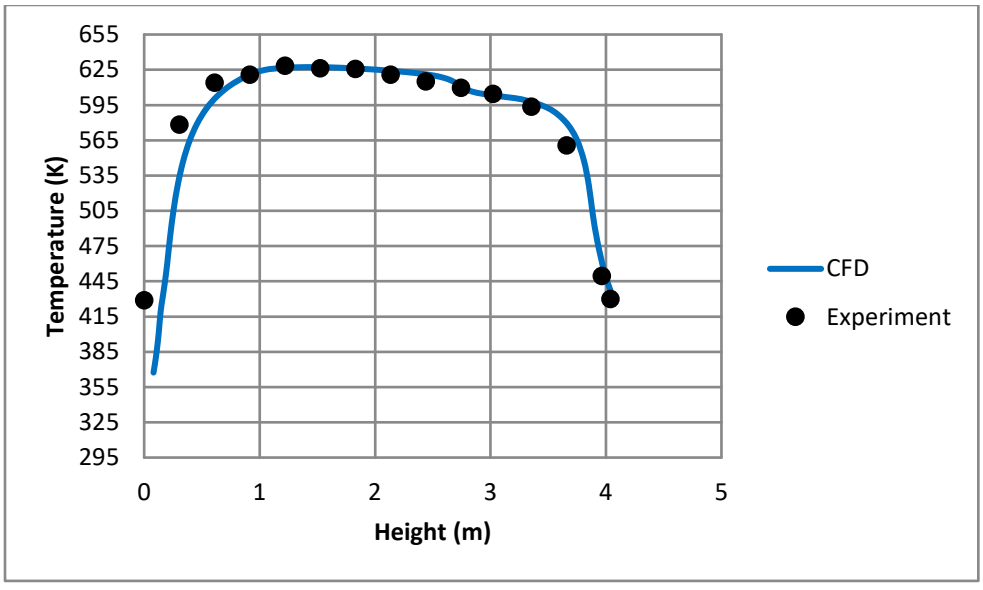

Figure 4-14 Channel Box Temperature for the Aboveground (100 kPa, 5 kW) Case

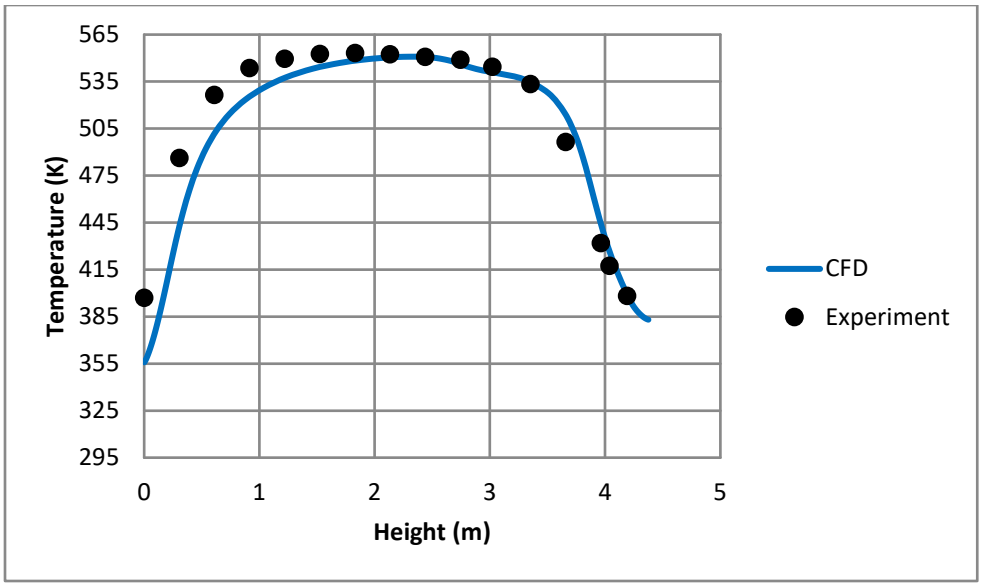

Figure 4-15 Basket Temperature for the Aboveground (100 kPa, 5 kW) Case

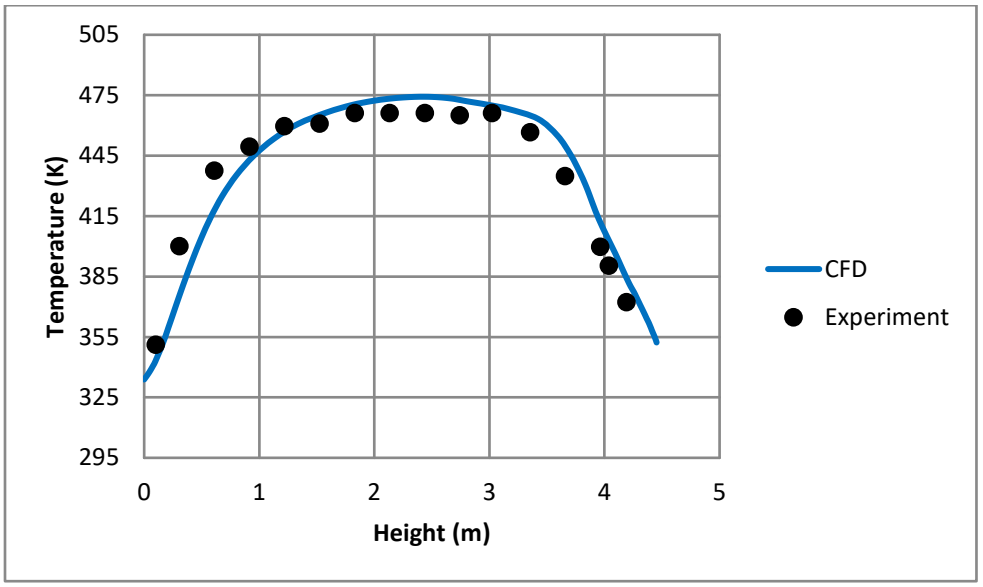

Figure 4-16 Pressure Vessel Temperature for the Aboveground (100 kPa, 5 kW) Case

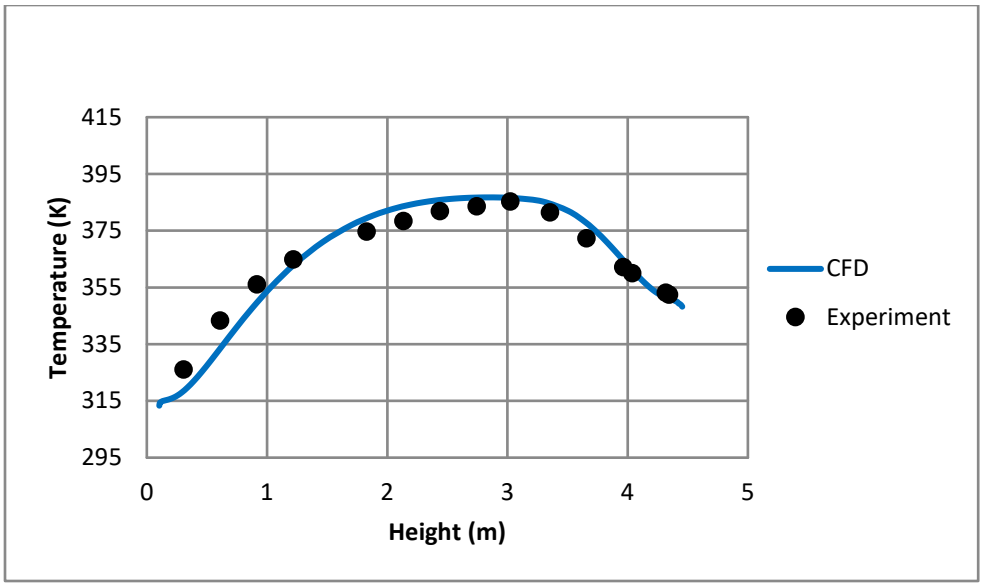

Figure 4-17 Shell1 Temperature for the Aboveground (100 kPa, 5 kW) Case

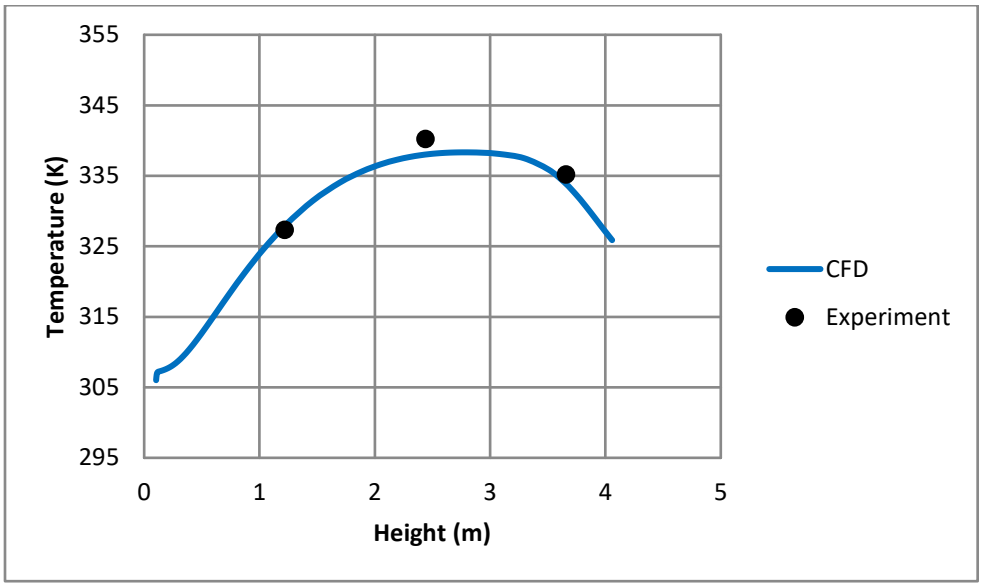

Figure 4-18 Shell1-Insulation Temperature for the Aboveground (100 kPa, 5 kW) Case

4.1.4 Aboveground (100 kPa, 0.5 kW) Case

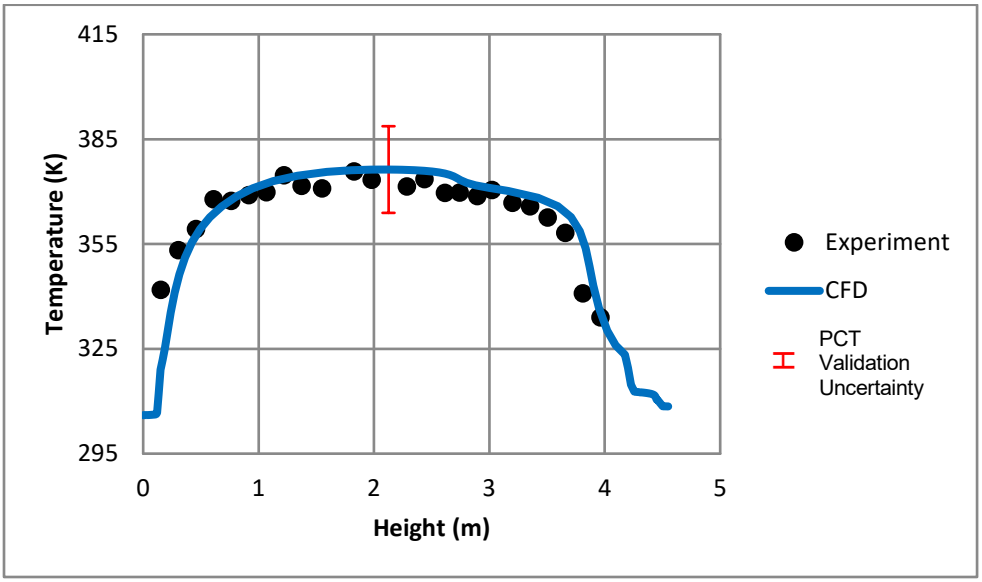

Figure 4-19 PCT for the Aboveground (100 kPa, 0.5 kW) Case

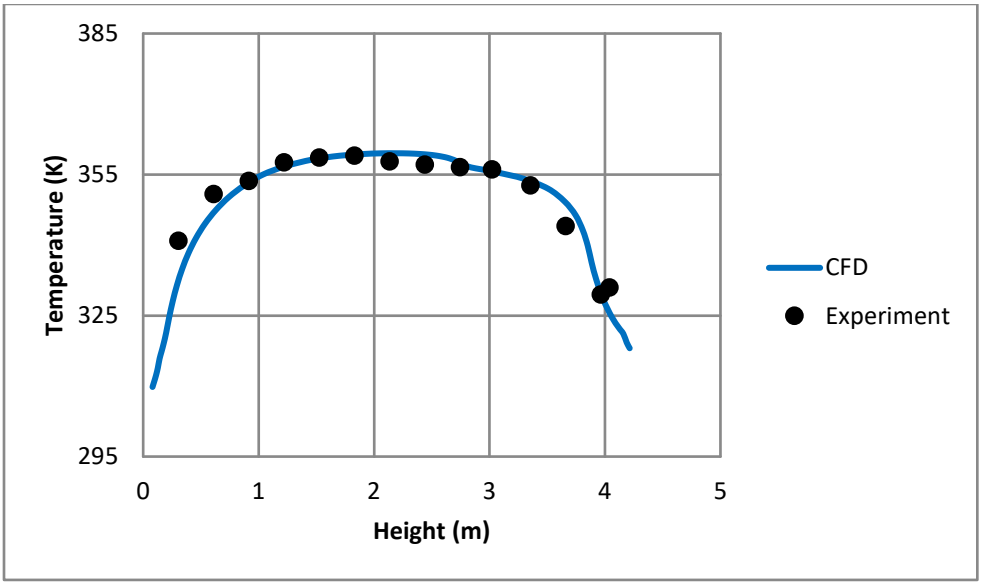

Figure 4-20 Channel Box Temperature for the Aboveground (100 kPa, 0.5 kW) Case

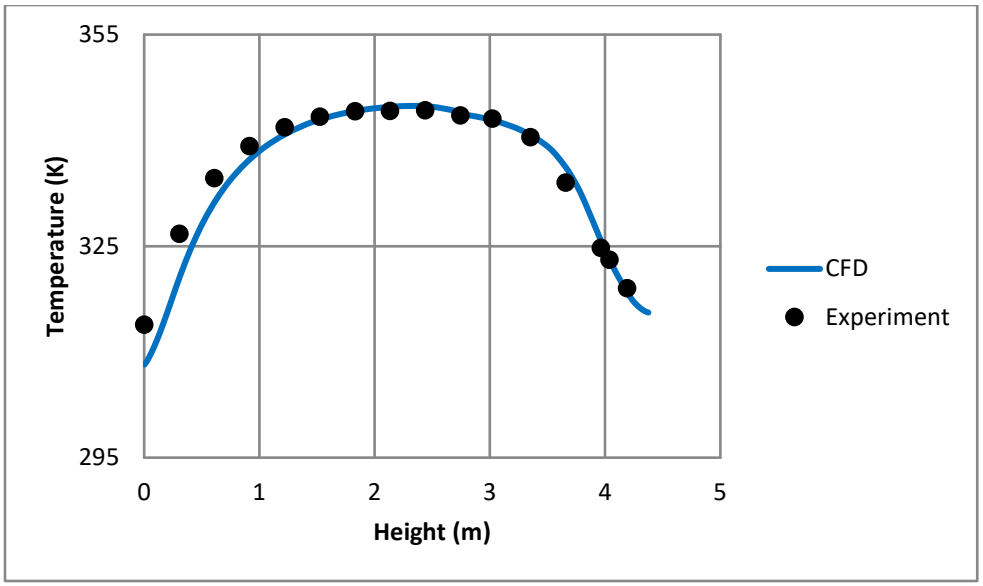

Figure 4-21 Basket Temperature for the Aboveground (100 kPa, 0.5 kW) Case

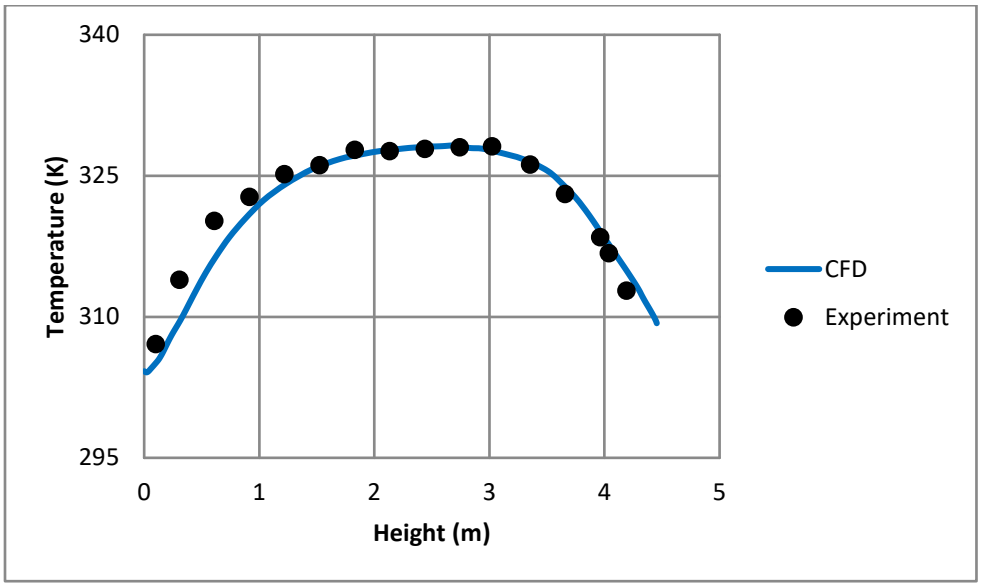

Figure 4-22 Pressure Vessel Temperature for the Aboveground (100 kPa, 0.5 kW) Case

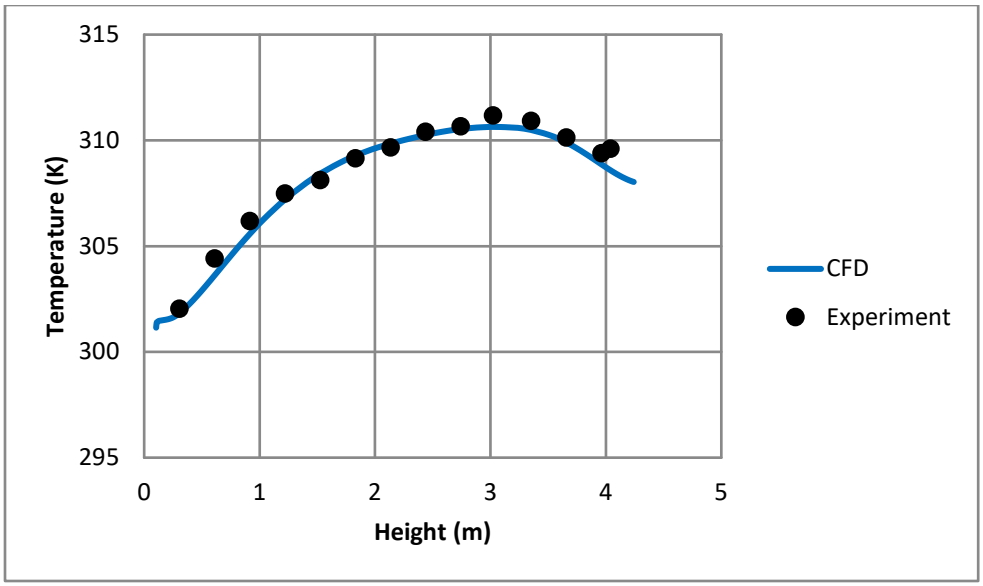

Figure 4-23 Shell1 Temperature for the Aboveground (100 kPa, 0.5 kW) Case

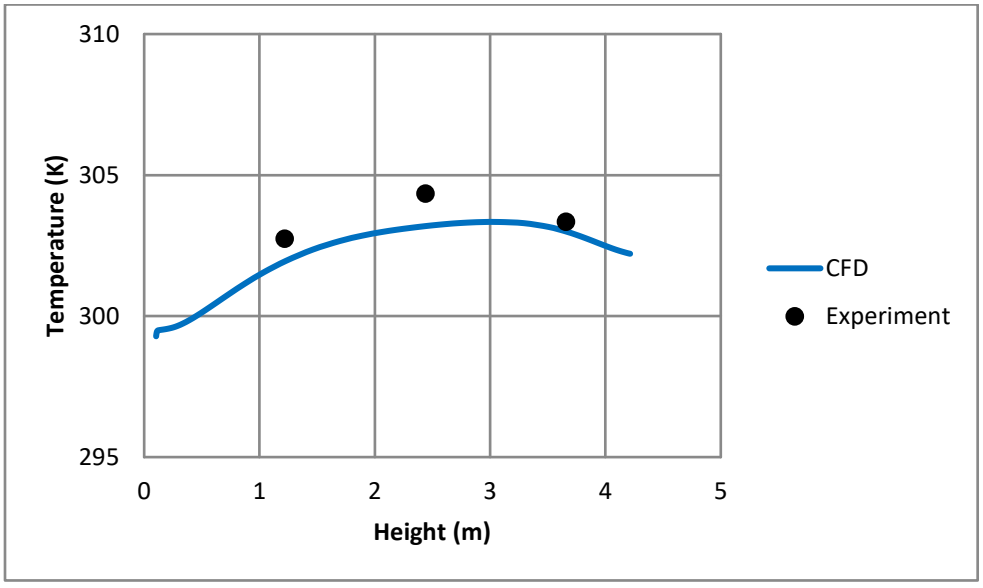

Figure 4-24 Shell1-Insulation Temperature for the Aboveground (100 kPa, 0.5 kW) Case

4.2 Underground Computational Fluid Dynamics Model Validation Results

CFD analyses were performed for 14 cases where the DCS achieved steady state for various assembly powers and pressures. The power levels tested were 0.5, 1.0, 2.5, and 5.0 kW. The vessel pressures tested were sub-atmospheric (i.e., 0.3 kPa), 100, 450, and 800 kPa absolute. CFD was performed for all these cases. On the other hand, the UQ for PCT and air mass flow rate was performed for eight cases, including (800 kPa, 5 kW), (800 kPa, 0.5 kW), (450 kPa, 2.5 kW), (100 kPa, 5 kW), (100 kPa, 2.5 kW), (100 kPa, 0.5 kW), (0.3 kPa, 1 kW), and (0.3 kPa, 0.5 kW).

This section presents four cases (800 kPa, 5 kW), (800 kPa, 0.5 kW), (100 kPa, 5 kW), and (100 kPa, 0.5 kW). Appendix B shows the other four cases.

Table 4-4 through Table 4-11 summarize the underground results of PCT and air mass flow rate, including UQ. Initially, like the aboveground case, the frictional factor for the honeycomb air flow straightener (i.e., D = 2.7×10^6 (m^{-2})) was used. Table 4-4 shows the results obtained for PCT and air mass flow rate. CFD analysis overpredicted the air mass flow rate for all the cases by as much as 12.8 percent. As such, a higher D-value was needed to model the honeycomb air flow straightener due to the compression effect and non-uniformity as discussed and explained in detail in NUREG/CR-7250.

A D-value of 3.6×10^6 (m^{-2}) was obtained based on a comparison between the experimental data and CFD numerical simulation for the highest air mass flow rate percentage error (i.e., 450 kPa, 0.5 kW) case. As such, this D-value was adopted for the rest of the underground CFD simulation cases.

Table 4-4 PCT and $\dot{m}_{air}$ for Underground Cases for D = 2.7×10^6 (m^{-2})

P (kPa)	Power (kW)	CFD		Data		Δ (CFD-Data)		
		PCT (K)	$\dot{m}_{air}$ (kg/s)	PCT (K)	$\dot{m}_{air}$ (kg/s)	Δ PCT (K)	Δ $\dot{m}_{air}$ (kg/s)	$\dot{m}_{air}$ % error
800	0.5	363	2.36×10^{-2}	363	2.18×10^{-2}	0	1.76×10^{-3}	7.5
800	1	405	3.33×10^{-2}	406	3.06×10^{-2}	1	2.70×10^{-3}	8.1
800	2.5	522	4.83×10^{-2}	524	4.57×10^{-2}	2	2.60×10^{-3}	5.4
800	5	661	6.55×10^{-2}	661	6.11×10^{-2}	0	4.42×10^{-3}	6.7
450	0.5	366	2.57×10^{-2}	366	2.24×10^{-2}	0	3.29×10^{-3}	12.8
450	1	420	3.45×10^{-2}	420	3.21×10^{-2}	0	2.43×10^{-3}	7.0
450	2.5	546	5.13×10^{-2}	546	4.88×10^{-2}	0	2.46×10^{-3}	4.8
450	5	694	7.00×10^{-2}	689	6.51×10^{-2}	5	4.90×10^{-3}	7.0
100	0.5	375	2.90×10^{-2}	374	2.64×10^{-2}	1	2.62×10^{-3}	9.0
100	1	434	3.96×10^{-2}	433	3.61×10^{-2}	1	3.49×10^{-3}	8.8
100	2.5	563	5.77×10^{-2}	563	5.33×10^{-2}	0	4.42×10^{-3}	7.7
100	5	707	7.51×10^{-2}	704	6.99×10^{-2}	3	5.24×10^{-3}	7.0
0.3	0.5	447	2.87×10^{-2}	454	2.59×10^{-2}	7	2.81×10^{-3}	9.8
0.3	1	535	3.91×10^{-2}	538	3.63×10^{-2}	3	2.76×10^{-3}	7.1

Table 4-5 PCT and $\dot{m}_{air}$ for Underground Cases for D = 3.6x10^6 (m^{-2})

P (kPa)	Power (kW)	CFD		Data		Δ (CFD-Data)		
		PCT (K)	$\dot{m}_{air}$ (kg/s)	PCT (K)	$\dot{m}_{air}$ (kg/s)	Δ PCT (K)	Δ $\dot{m}_{air}$ (kg/s)	$\dot{m}_{air}$ % error
800	0.5	364	2.15x10^{-2}	363	2.18x10^{-2}	1	3.26x10^{-4}	1.5
800	1	405	3.07x10^{-2}	406	3.06x10^{-2}	1	9.04x10^{-5}	0.3
800	2.5	522	4.50x10^{-2}	524	4.57x10^{-2}	2	7.20x10^{-4}	1.6
800	5	661	6.15x10^{-2}	661	6.11x10^{-2}	0	4.32x10^{-4}	0.7
450	0.5	367	2.35x10^{-2}	366	2.24x10^{-2}	1	1.13x10^{-3}	4.8
450	1	421	3.2x10^{-2}	420	3.21x10^{-2}	1	1.40x10^{-4}	0.4
450	2.5	548	4.79x10^{-2}	546	4.88x10^{-2}	2	8.80x10^{-4}	1.8
450	5	695	6.59x10^{-2}	689	6.51x10^{-2}	6	8.08x10^{-4}	1.2
100	0.5	376	2.67x10^{-2}	374	2.64x10^{-2}	2	3.08x10^{-4}	1.2
100	1	435	3.68x10^{-2}	433	3.61x10^{-2}	2	6.64x10^{-4}	1.8
100	2.5	564	5.41x10^{-2}	563	5.33x10^{-2}	1	8.36x10^{-4}	1.5
100	5	707	7.09x10^{-2}	704	6.99x10^{-2}	3	9.88x10^{-4}	1.4
0.3	0.5	447	2.65x10^{-2}	454	2.59x10^{-2}	7	5.60x10^{-4}	2.1
0.3	1	535	3.63x10^{-2}	538	3.63x10^{-2}	3	5.04x10^{-5}	0.1

Table 4-6 PCT Uncertainty Quantification for Underground Cases

P (kPa)	Power (kW)	PCT (K)		Δ PCT (K) (CFD-Data)	Uncertainty (K)		
		CFD	Data		Data	Simulation	Validation
800	0.5	364	363	1	7	8.9	11.3
800	1	405	406	1	7		
800	2.5	522	524	2	7		
800	5	661	661	0	7	10.5	12.6
450	0.5	367	366	1	7		
450	1	421	420	1	7		
450	2.5	548	546	2	7	9.5	11.8
450	5	695	689	6	7		
100	0.5	376	374	2	7	10.5	12.6
100	1	435	433	2	7		
100	2.5	564	563	1	7	9.3	11.6
100	5	707	704	3	7	11.7	13.6
0.3	0.5	447	454	7	7	16.8	18.2
0.3	1	535	538	3	7	14	15.7

Table 4-7 $\dot{m}_{air}$ Uncertainty Quantification for Underground Cases

P (kPa)	Power (kW)	$\dot{m}_{air}$ (kg/sec)		$\Delta \dot{m}_{air}$ (kg/sec) (CFD-Data)	Uncertainty (kg/sec)		
		CFD	Data		Data	Simulation	Validation
800	0.5	2.15×10^{-2}	2.18×10^{-2}	3.26×10^{-4}	1.1×10^{-3}	1.601×10^{-3}	1.95×10^{-3}
800	1	3.07×10^{-2}	3.06×10^{-2}	9.04×10^{-5}	1.1×10^{-3}		
800	2.5	4.5×10^{-2}	4.57×10^{-2}	7.20×10^{-4}	1.1×10^{-3}		
800	5	6.15×10^{-2}	6.11×10^{-2}	4.32×10^{-4}	1.1×10^{-3}	2.30×10^{-3}	2.55×10^{-3}
450	0.5	2.35×10^{-2}	2.24×10^{-2}	1.13×10^{-3}	1.1×10^{-3}		
450	1	3.20×10^{-2}	3.21×10^{-2}	1.40×10^{-4}	1.1×10^{-3}		
450	2.5	4.80×10^{-2}	4.88×10^{-2}	8.80×10^{-4}	1.1×10^{-3}	1.91×10^{-3}	2.20×10^{-3}
450	5	6.60×10^{-2}	6.51×10^{-2}	8.08×10^{-4}	1.1×10^{-3}		
100	0.5	2.67×10^{-2}	2.64×10^{-2}	3.08×10^{-4}	1.1×10^{-3}	1.57×10^{-3}	1.91×10^{-3}
100	1	3.68×10^{-2}	3.61×10^{-2}	6.64×10^{-4}	1.1×10^{-3}		
100	2.5	5.41×10^{-2}	5.33×10^{-2}	8.36×10^{-4}	1.1×10^{-3}	1.98×10^{-3}	2.26×10^{-3}
100	5	7.08×10^{-2}	6.99×10^{-2}	9.88×10^{-4}	1.1×10^{-3}	2.36×10^{-3}	2.61×10^{-3}
0.3	0.5	2.65×10^{-2}	2.59×10^{-2}	5.60×10^{-4}	1.1×10^{-3}	1.58×10^{-3}	1.93×10^{-3}
0.3	1	3.63×10^{-2}	3.63×10^{-2}	5.04×10^{-5}	1.1×10^{-3}	1.32×10^{-3}	1.71×10^{-3}

Sections 4.2.1 through 4.2.4 show temperature profiles as function of height for the assembly fuel region maximum temperature including the PCT, channel box, basket, pressure vessel, shell1, and shell2. The PCT validation uncertainty bar is shown at all PCT locations.

4.2.1 Underground (800 kPa, 5 kW) Case

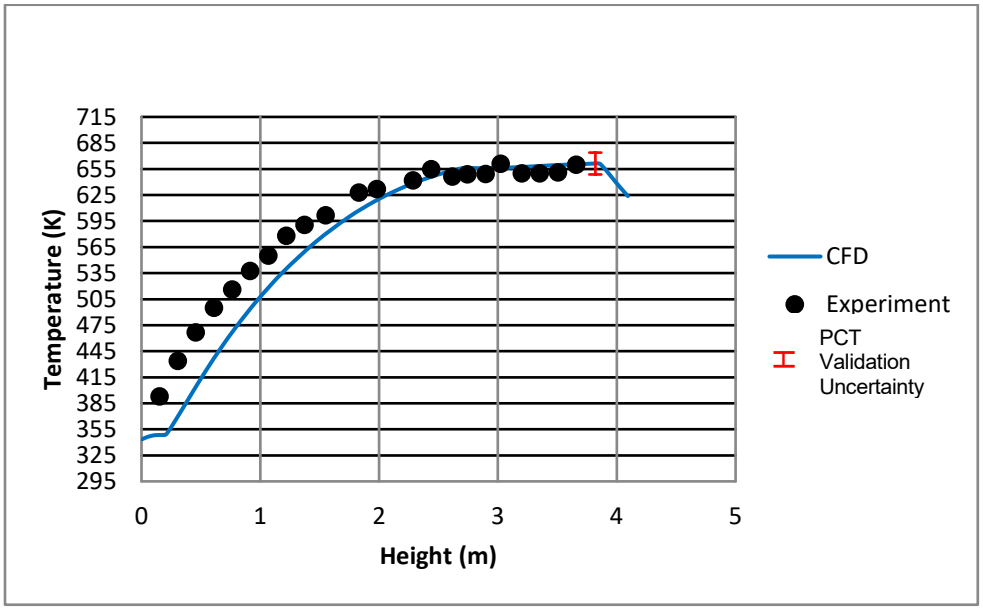

Figure 4-25 PCT for the Underground (800 kPa, 5 kW) Case

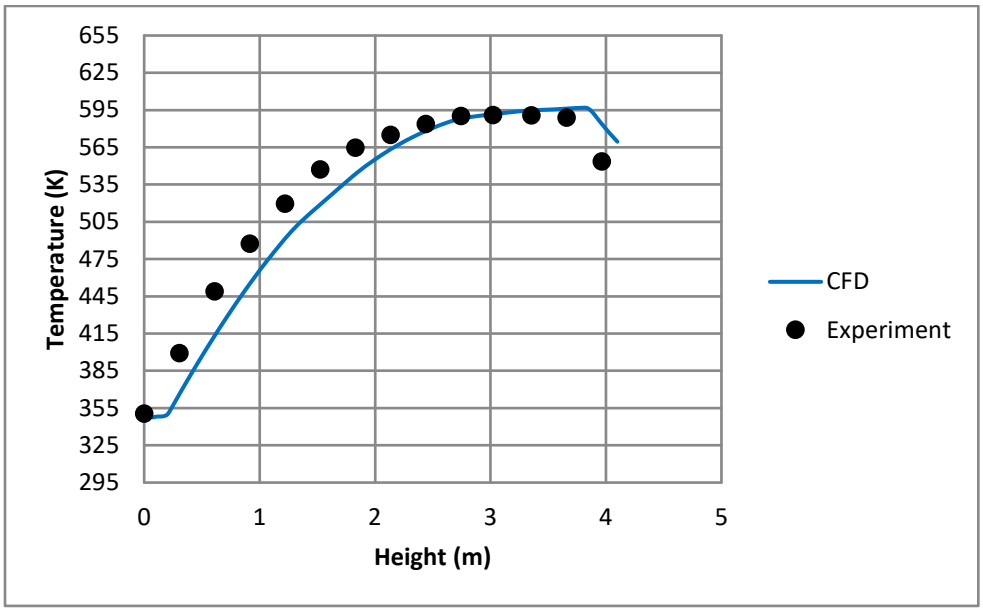

Figure 4-26 Channel Box Temperature for the Underground (800 kPa, 5 kW) Case

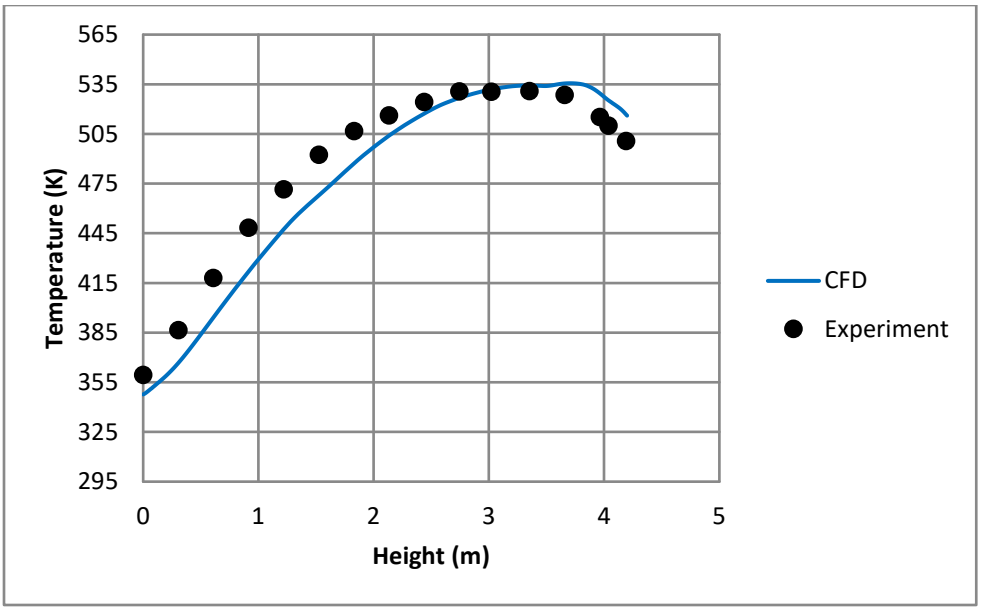

Figure 4-27 Basket Temperature for the Underground (800 kPa, 5 kW) Case

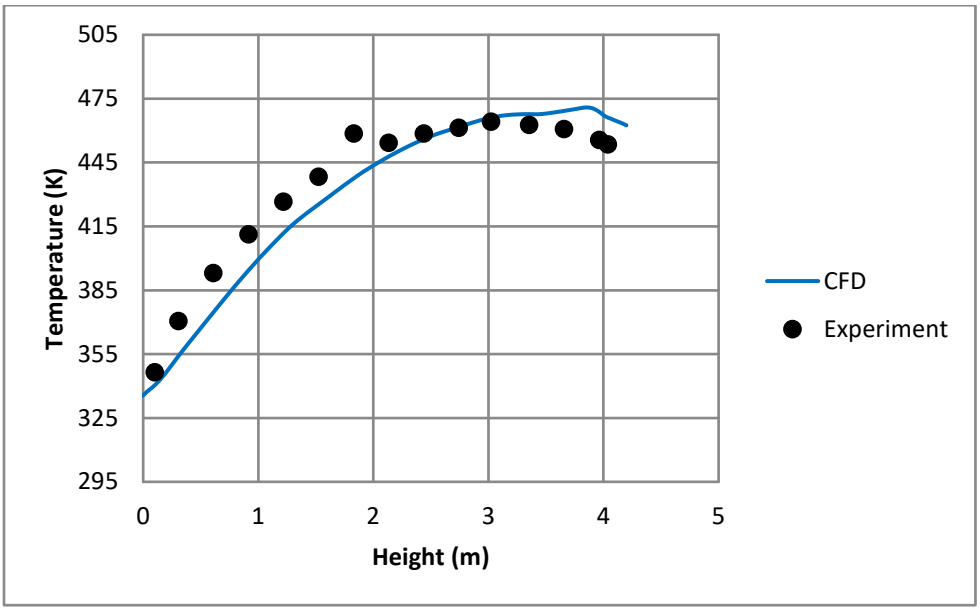

Figure 4-28 Pressure Vessel Temperature for the Underground (800 kPa, 5 kW) Case

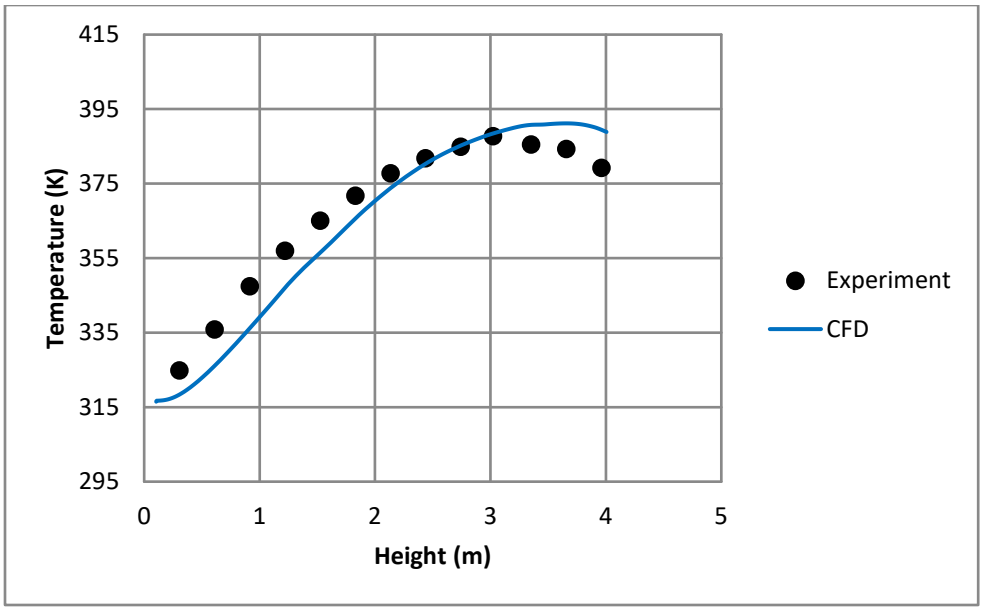

Figure 4-29 Shell1 Temperature for the Underground (800 kPa, 5 kW) Case

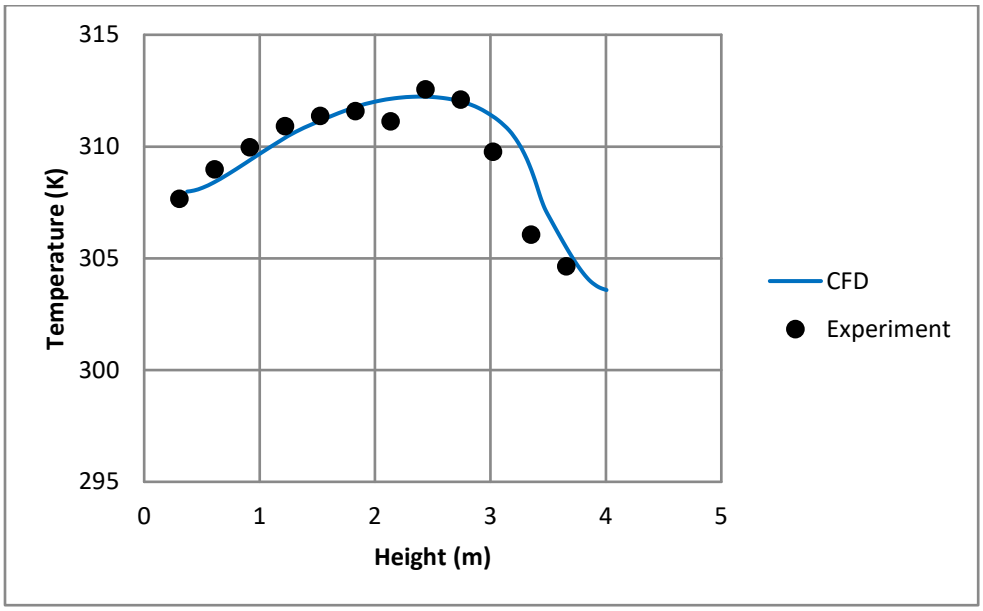

Figure 4-30 Shell2 Temperature for the Underground (800 kPa, 5 kW) Case

4.2.2 Underground (800 kPa, 0.5 kW) Case

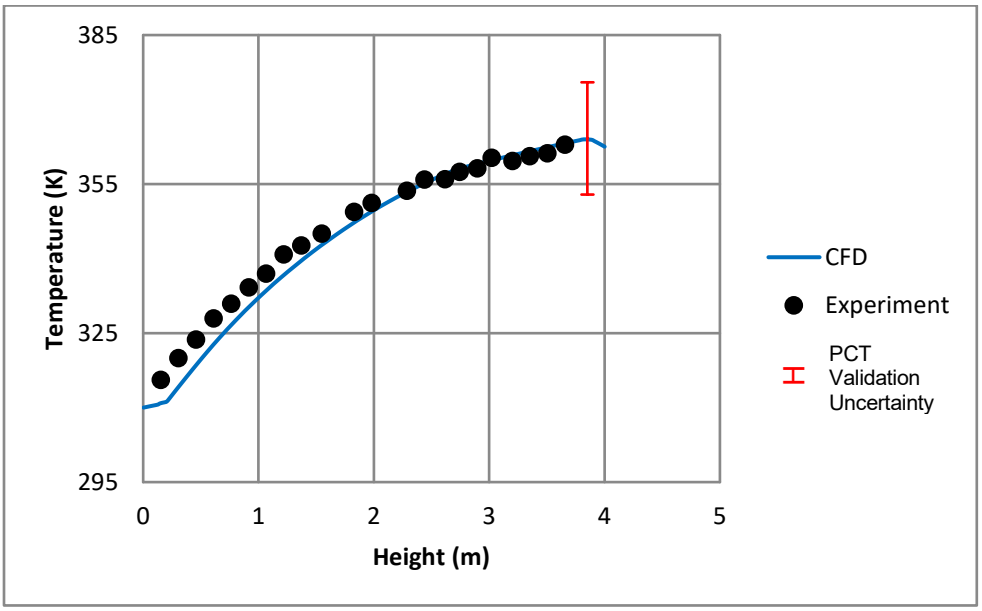

Figure 4-31 PCT for the Underground (800 kPa, 0.5 kW) Case

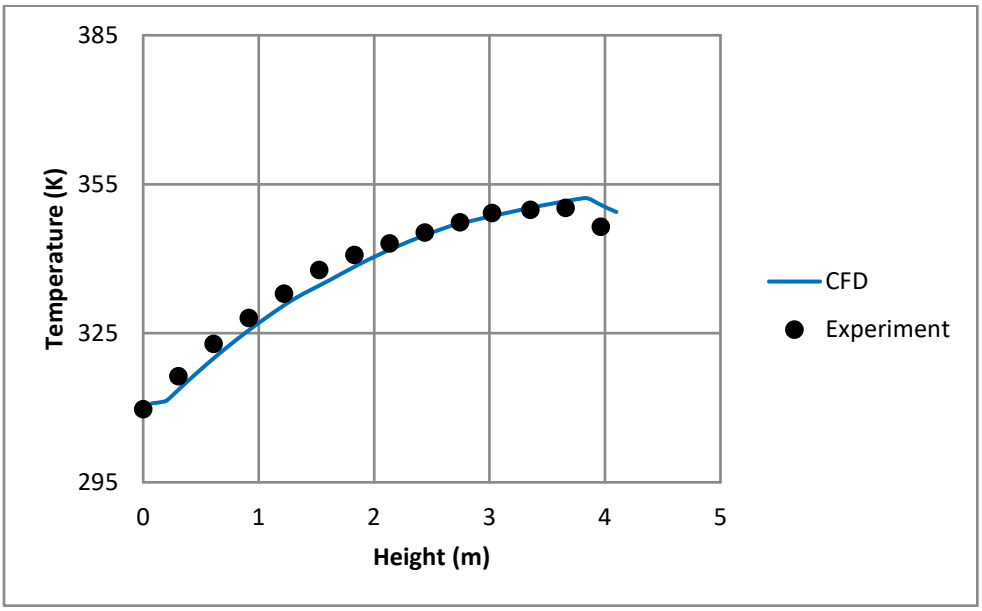

Figure 4-32 Channel Box Temperature for the Underground (800 kPa, 0.5 kW) Case

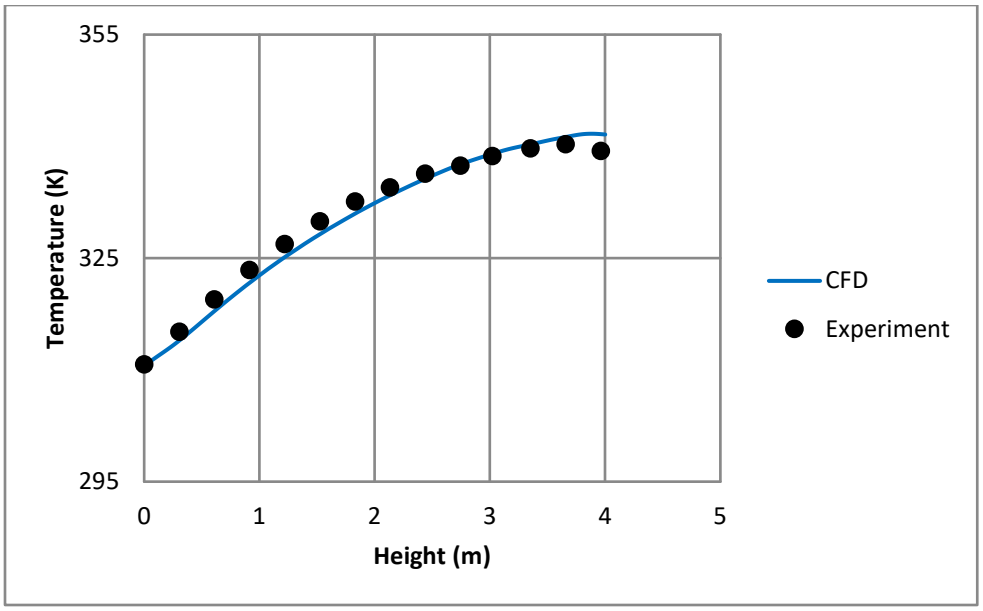

Figure 4-33 Basket Temperature for the Underground (800 kPa, 0.5 kW) Case

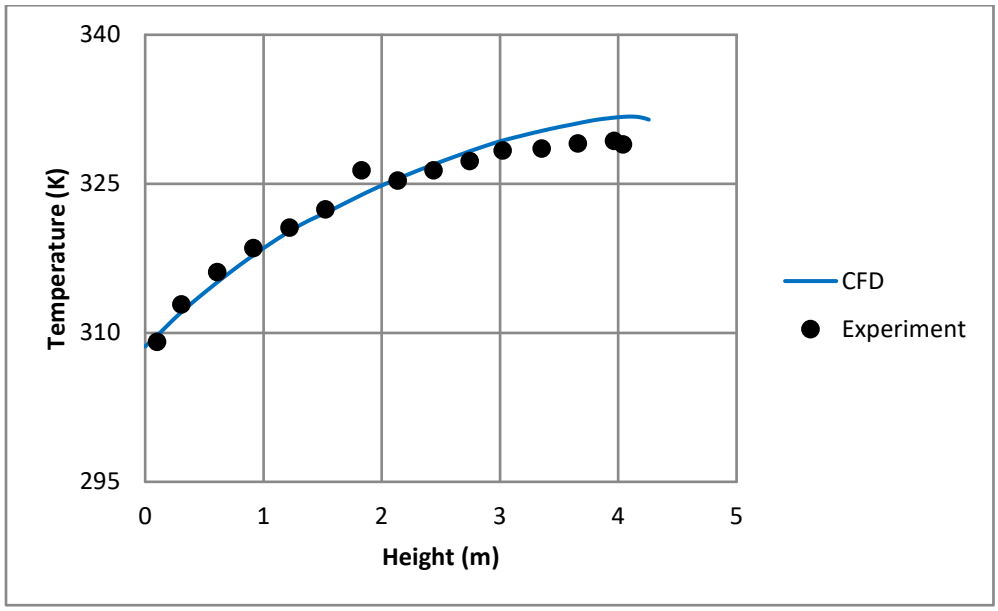

Figure 4-34 Pressure Vessel Temperature for the Underground (800 kPa, 0.5 kW) Case

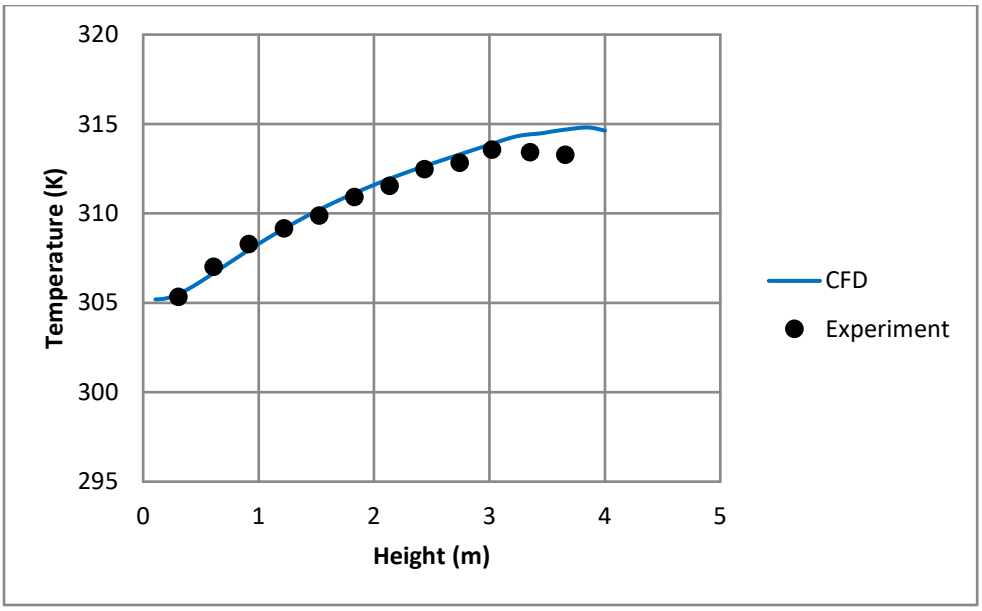

Figure 4-35 Shell1 Temperature for the Underground (800 kPa, 0.5 kW) Case

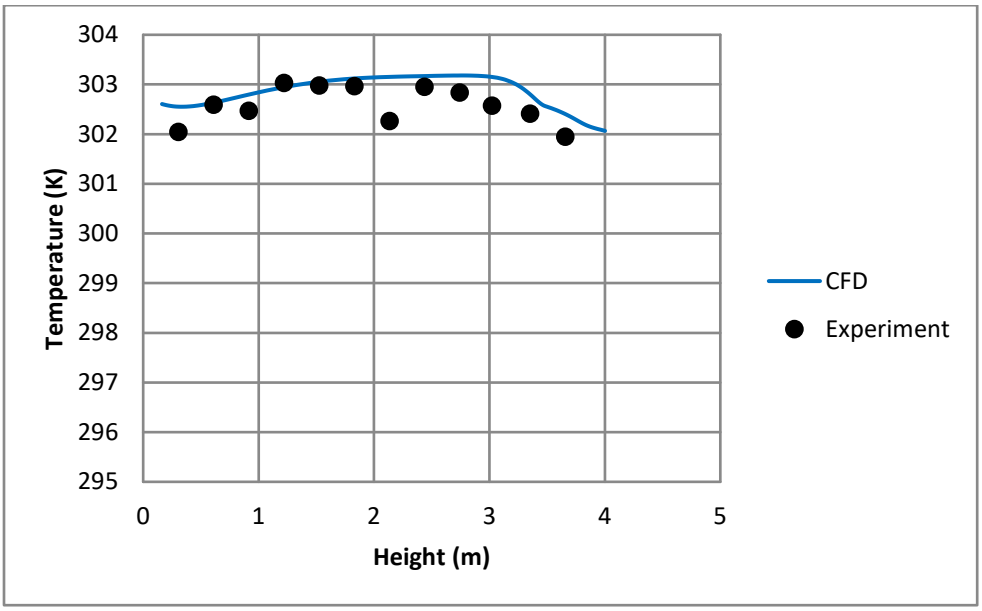

Figure 4-36 Shell2 Temperature for the Underground (800 kPa, 0.5 kW) Case

4.2.3 Underground (100 kPa, 5 kW) Case

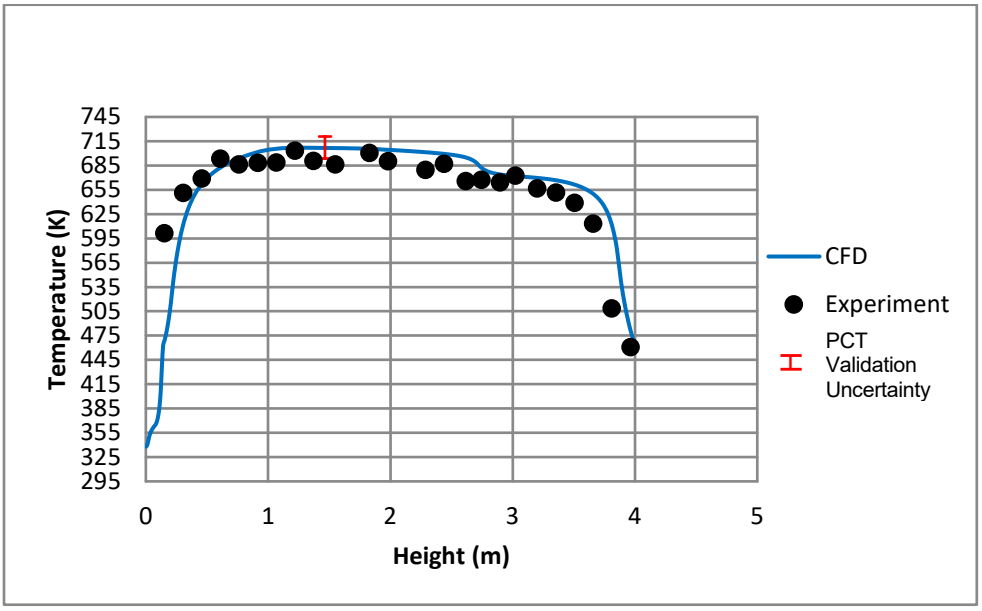

Figure 4-37 PCT for the Underground (100 kPa, 5 kW) Case

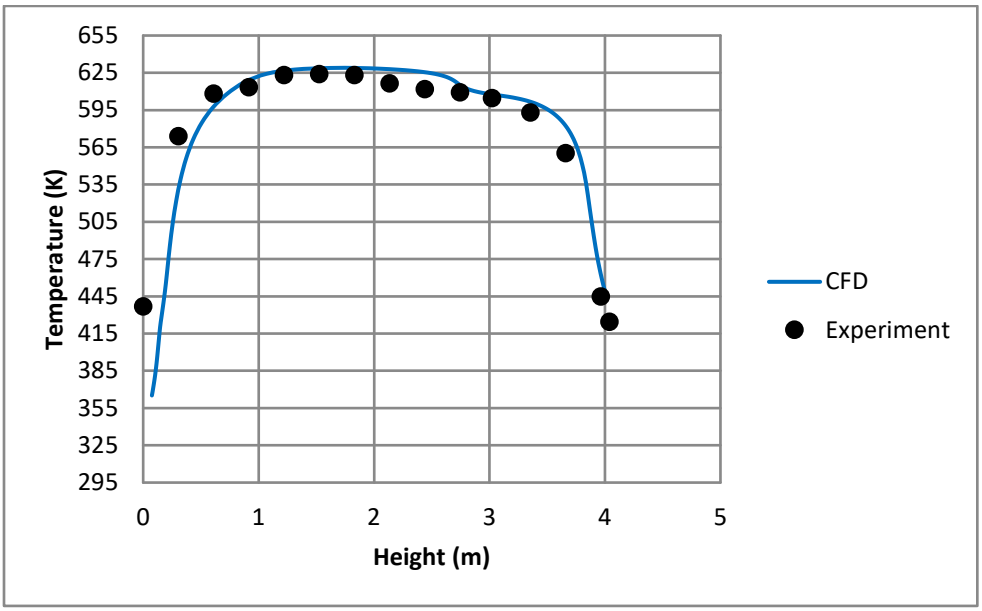

Figure 4-38 Channel Box Temperature for the Underground (100 kPa, 5 kW) Case

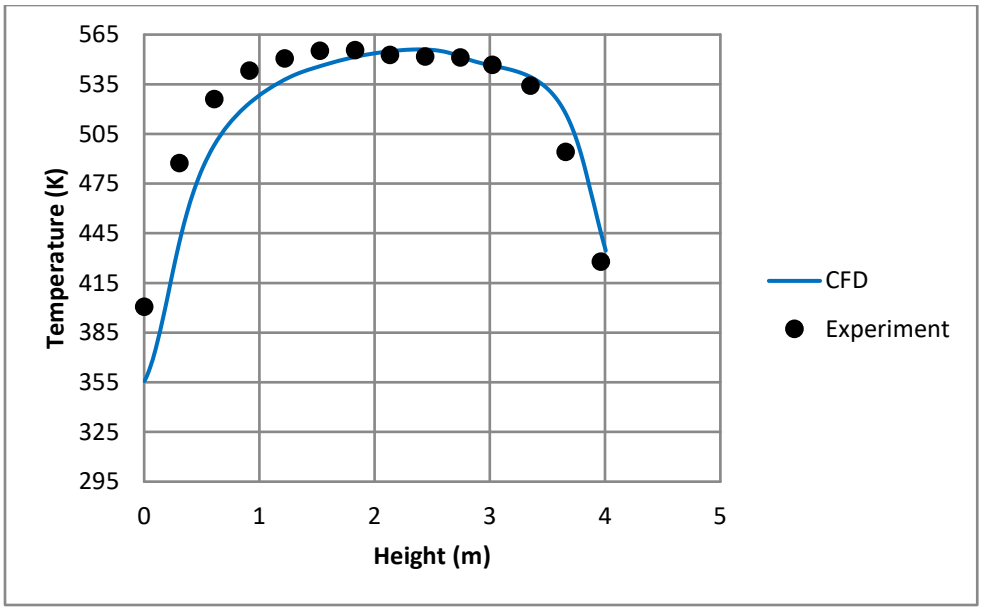

Figure 4-39 Basket Temperature for the Underground (100 kPa, 5 kW) Case

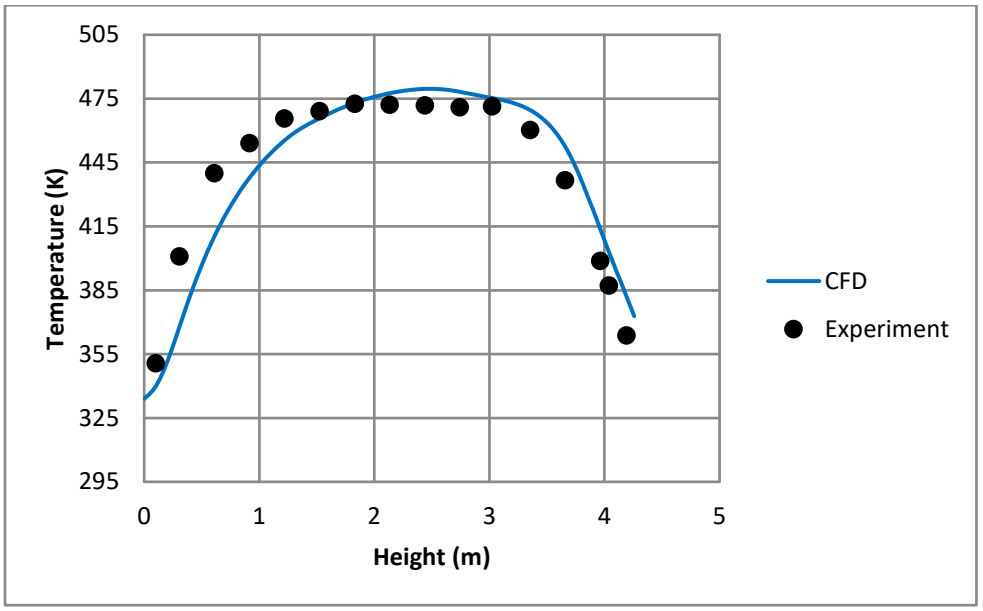

Figure 4-40 Pressure Vessel Temperature for the Underground (100 kPa, 5 kW) Case

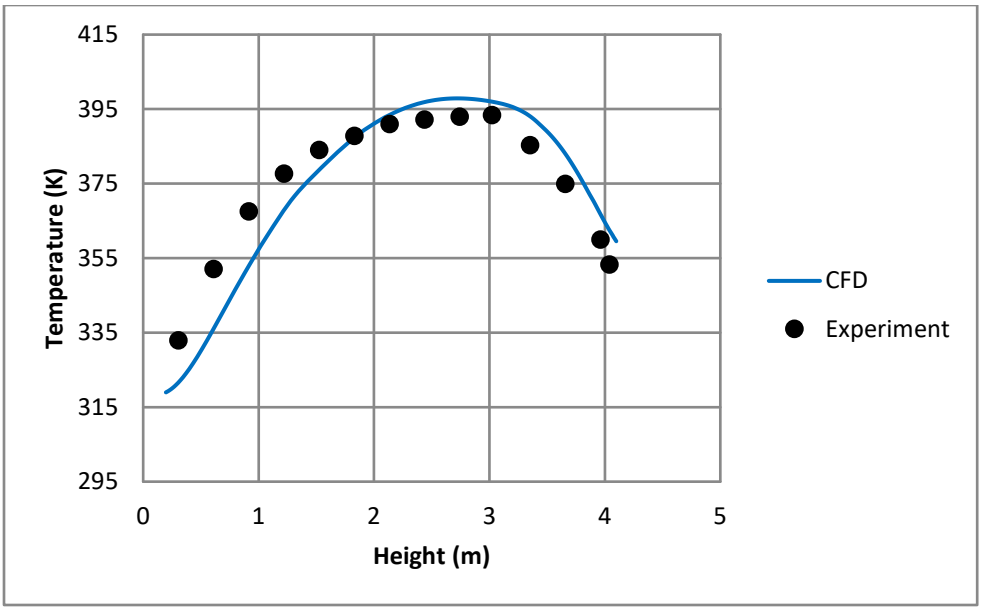

Figure 4-41 Shell1 Temperature for the Underground (100 kPa, 5 kW) Case

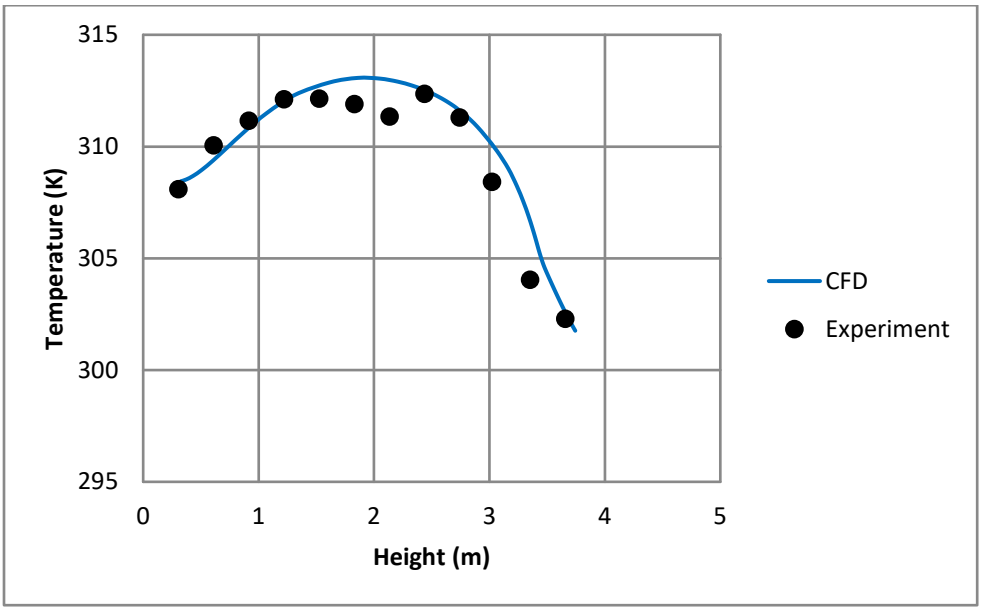

Figure 4-42 Shell2 Temperature for the Underground (100 kPa, 5 kW) Case

4.2.4 Underground (100 kPa, 0.5 kW) Case

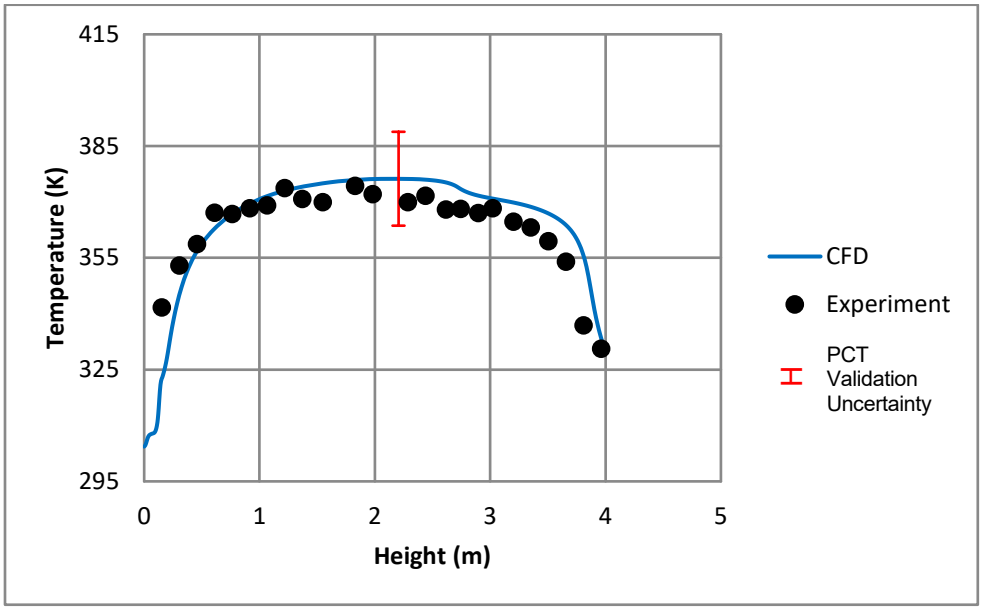

Figure 4-43 PCT for the Underground (100 kPa, 0.5 kW) Case

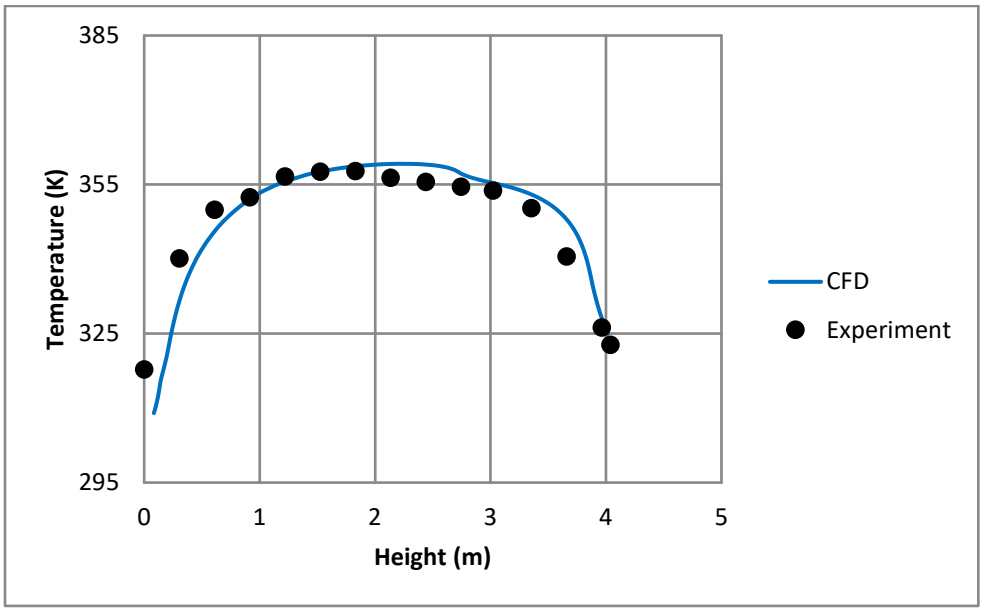

Figure 4-44 Channel Box Temperature for the Underground (100 kPa, 0.5 kW) Case

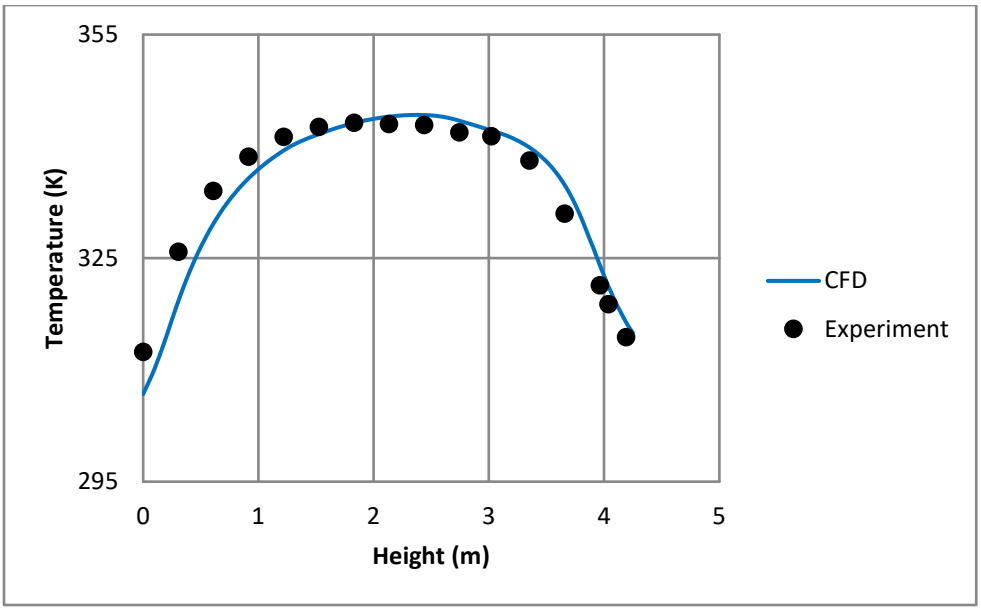

Figure 4-45 Basket Temperature for the Underground (100 kPa, 0.5 kW) Case

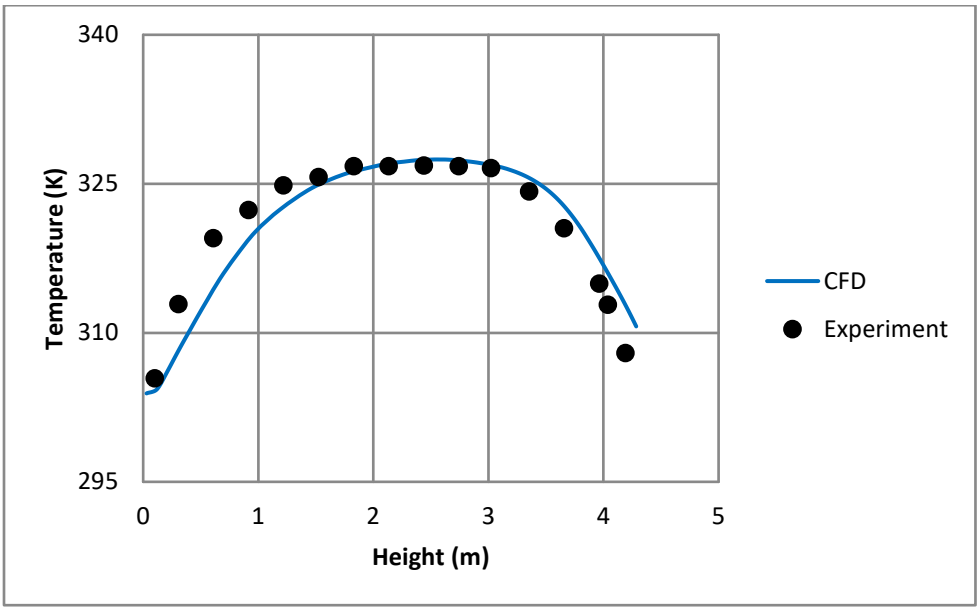

Figure 4-46 Pressure Vessel Temperature for the Underground (100 kPa, 0.5 kW) Case

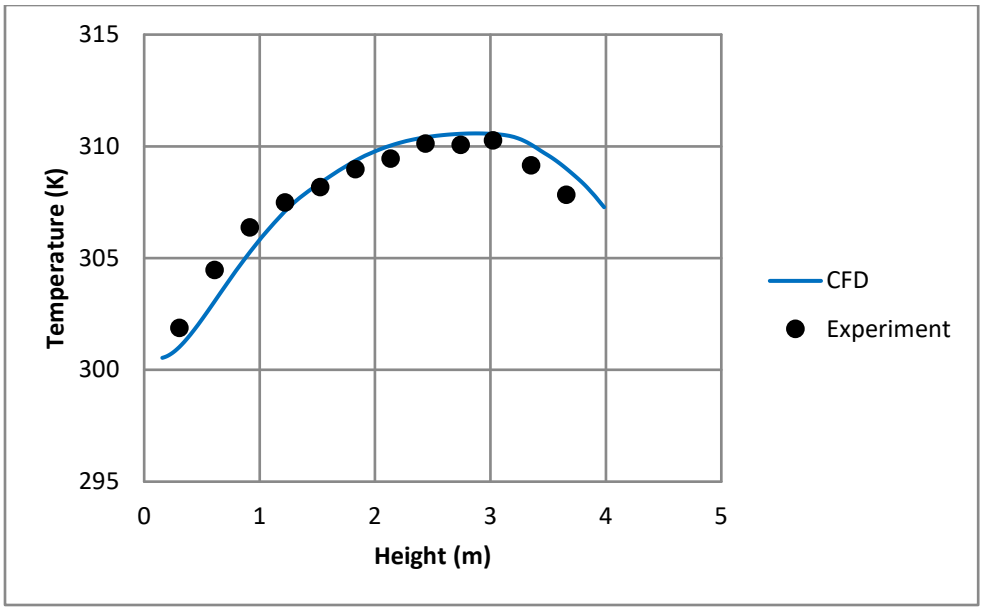

Figure 4-47 Shell1 Temperature for the Underground (100 kPa, 0.5 kW) Case

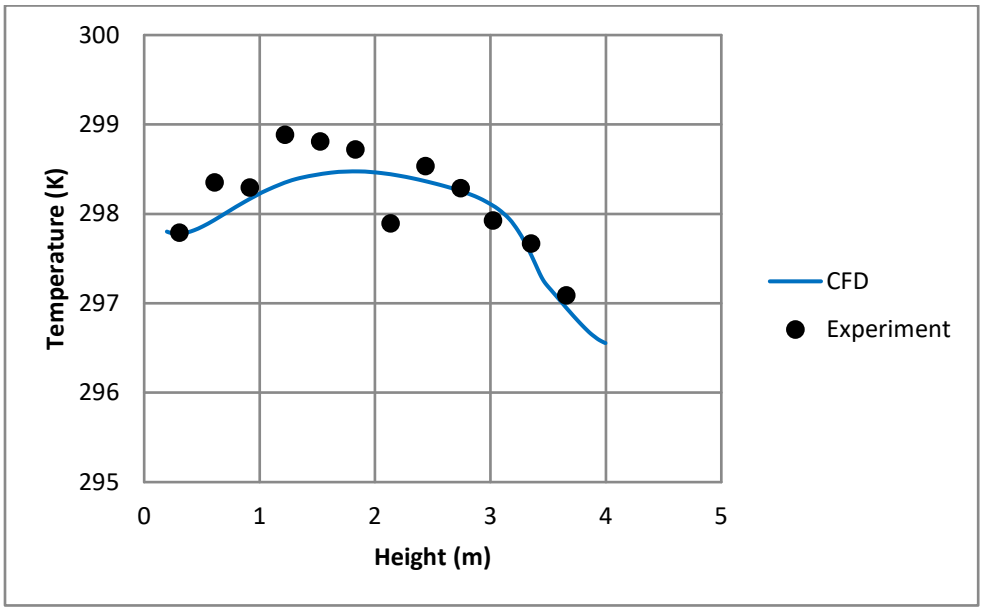

Figure 4-48 Shell2 Temperature for the Underground (100 kPa, 0.5 kW) Case

As shown in Table 4-1 through Table 4-3 for the aboveground cases, and in Table 4-4 through Table 4-7 for the underground cases, the PCT and air mass flow rate are within the validation uncertainty (i.e., the validation uncertainty is larger than the difference between the experiment and the CFD predictions). From the plots shown in this section and in Appendix B to this report, CFD results mimic and predicts very favorably the shape of the experimental temperature profile for all cases for the fuel temperature including PCT, channel box, basket, pressure vessel, shell1, shell2, and shell1-insulation. As shown for the high-pressure cases (i.e., 800 kPa), the higher temperatures occur near the top of the pressure vessel, as shown in Figures 4-1 and 4-7 for the aboveground cases, and Figures 4-25 and 4-31 for the underground cases. However, for the lower pressure cases (i.e., 100 kPa), the higher temperatures occur near the middle section of the vessel. Temperature in this middle section stayed almost flat for a distance spanning between 1/3 and 2/3 of the height, as illustrated in Figure 4-13 and Figure 4-19 for the aboveground cases, and Figures 4-37 and 4-43 for the underground cases. For the pressure of 450 kPa, the higher temperature values were reached at a height between the high temperature locations for the 800 kPa and 100 kPa cases (i.e., approximately at 2/3 height) as shown in Figures B-1 and B-25 for the aboveground cases and underground cases, respectively. For the sub-atmospheric (i.e. 0.3 kPa) cases shown in Appendix B.1, the higher temperatures are reached in the lower section (i.e., bottom 1/3) as illustrated in Figure B-13 and Figure B-19 for the aboveground cases, and Figures B-37 and B-43, for the underground cases.

Higher temperature values were reached at lower pressures for the same power value as a result of lower convection heat transfer, due to a lower helium mass flow rate inside the pressure vessel. Conversely, for higher pressure, higher convection heat transfer will take place as a result of the higher helium mass flow rate in the assembly. For the sub-atmospheric (i.e. 0.3 kPa) cases, as shown in Figure B-13 and Figure B-19 for the aboveground cases, and Figures B-37 and B-43 for the underground cases, even higher temperatures were reached due to the introduction of air (i.e. leakage) inside the pressure vessel. In these cases, vacuum conditions were sought, but due to unavoidable air leakage, vacuum conditions were not achieved. Air thermal conductivity is much lower than helium thermal conductivity. Consequently, lower heat transfer by conduction took place through the air medium, and higher temperatures were reached for these low-pressure sub-atmospheric (i.e. 0.3 kPa) cases.

The PCT axial profiles for all the cases show discrepancies between experimental data and CFD predictions at lower heights. This difference became smaller as the pressure decreased. The axial temperature profiles for the DCS structures (i.e., channel box, basket, pressure vessel, shell1, shell1-insulation, and shell2) trend closer to the experimental data than the axial temperature profiles for the PCT in all the cases. A possible explanation for this discrepancy could be attributed to the power distribution model or uncertainty for the thermocouple's location. Further work is needed to determine the reasons for these trends. However, one immediate observation was that the temperature profiles moving outward from the fuel assembly to the DCS structures approach the same ambient temperatures. Certainly, this cannot be attributed to the use of porous media to model the fuel region, as CFD models using an explicit representation of the fuel region predicted similar trends [10].

The CFD thermal model predicted the temperature profile for the DCS external wall (i.e., shell2) very favorably within the experimental uncertainty of 3 K, as seen in Figures 4-30, 4-36, 4-42, and 4-48, and in Figures B-30, B-36, B-42, and B-48 in Appendix B. These favorable predictions proved that the BCs, using the combination of convection and radiation through a linked subroutine to ANSYS Fluent at the external boundaries of DCS, were modeled correctly.

As illustrated in the uncertainty tables in Chapter 3 and Appendix A, the major component of the simulation uncertainty is the input uncertainty for both the PCT and the air mass flow rate. The PCT input uncertainty is affected by different input variables, depending on the case. For high decay heat cases, the carbon steel emissivity and fuel radial thermal conductivity contributed the most to the PCT input uncertainty. The decay heat variability also contributed to the input uncertainty but to a lesser extent. For lower decay heat cases, the PCT input uncertainty is mostly affected by the decay heat variability, ambient temperature variation, and, to a lesser extent, by fuel radial thermal conductivity and carbon steel emissivity. For all cases, the air mass flow rate input uncertainty was primarily affected by the variation of the inlet flow straightener's porous media frictional coefficient, ambient temperature, and, to a lesser extent, decay heat and carbon steel emissivity.

A PCT validation uncertainty varying between 10.7 and 13.6 K for pressurized-helium cases and changing between 15.5 and 18.2 K for the sub-atmospheric (i.e. 0.3 kPa) cases were calculated for both the aboveground and underground configuration testing. An air mass flow rate validation uncertainty varying between 1.25×10^{-3} and 1.93×10^{-3} kg/s was calculated for pressurized-helium cases, and between 1.32×10^{-3} and 1.83×10^{-3} kg/s for the sub-atmospheric (i.e. 0.3 kPa) cases. The maximum validation uncertainty of the PCT and the air mass flow rate represents 2.5 percent and 2.8 percent of the maximum measured PCT and air mass flow rate, respectively. The calculated validation uncertainties are a small fraction of the maximum PCT, and mass flow rate measured in the experiment. As such, this experiment can be classified as a CFD-grade experiment.

As part of the licensing of dry cask storage systems, vendors have submitted applications with margins in the range of 10 to 20 degrees C from the currently acceptable cladding temperature limit of 400 degrees C, as discussed in NRC ISG-11 [12]. To be useful as a demonstration of the accuracy of the CFD modeling process or to improve the model's capabilities, the validation uncertainty should be less than or equal to this margin of 10 to 20 degrees C. Cask system designs that are complex enough to benefit from CFD modeling generally have a great many inputs that influence the simulation result. CFD-grade experiments are those that precisely measure each one of these inputs so that the input uncertainty of the simulation can be minimized. It is a difficult and complicated task to design and conduct such an experiment, even for relatively simple configurations, which is why so few are conducted. However, to gain confidence in the application of CFD as a tool in the certification process, especially with more complex physics, validation exercises such as this are necessary.

4.3 Underground with Crosswind

Steady-state CFD calculations were performed for multiple cases, for decay heat power of 5 kW and pressure of 800 kPa and 100 kPa, using crosswind speeds varying between 0 to 8.9 m/s (0 to 20 mph). These steady state runs were initialized using steady state solutions with no crosswind. A transient analysis of 50 hours was also performed for one case using a decay heat power of 5 kW and a pressure of 100 kPa, with a crosswind speed of 5.4 m/s (12 mph), starting from naturally induced conditions with no crosswind.

4.3.1 Crosswind (800 kPa, 5 kW) Cases

4.3.1.1 Steady State

Table 4-8 Steady State CFD for Underground with Crosswind at (800 kPa, 5 kW)

Wind Speed in m/s (mph)	PCT (K)	$\dot{m}_{air}$ (kg/sec)	(PCT-$PCT_{naturally\ induced}$) (K)	$\dot{m}_{air}/\dot{m}_{air\_naturally\ induced}$	Δ (PCT-$PCT_{naturally\ induced}$) (K)	Δ ($\dot{m}_{air}/\dot{m}_{air\_naturally\ induced}$)
0 (naturally induced)	667	$5.86x10^{-2}$	0.0	1.000	21.08	$8.07x10^{-2}$
1.34 (3)	664	$5.15x10^{-2}$	-2.4	0.879	21.08	$7.58x10^{-2}$
2.68 (6)	662	$3.45x10^{-2}$	-4.4	0.588	21.08	$6.41x10^{-2}$
4.02 (9)	660	$2.95x10^{-2}$	-6.6	0.503	21.08	$6.06x10^{-2}$
4.47 (10)	659	$2.87x10^{-2}$	-7.9	0.490	21.08	$6.01x10^{-2}$
4.92 (11)	658	$2.84x10^{-2}$	-9.0	0.485	21.08	$5.99x10^{-2}$
5.36 (12)	656	$2.85x10^{-2}$	-10.6	0.486	21.08	$5.99x10^{-2}$
5.81 (13)	655	$2.90x10^{-2}$	-11.9	0.494	21.08	$6.03x10^{-2}$
6.71 (15)	652	$3.08x10^{-2}$	-14.8	0.526	21.08	$6.16x10^{-2}$
8.94 (20)	648	$3.44x10^{-2}$	-19.0	0.587	21.08	$6.40x10^{-2}$

Table 4-9 Steady-State Experiment for Underground with Crosswind at (800 kPa, 5 kW)

Wind Speed in m/s (mph)	$\dot{m}_{air}$ (kg/sec)	$\dot{m}_{air}/\dot{m}_{air\_naturally\ induced}$	(PCT-$PCT_{naturally\ induced}$) (K)	Δ ($\dot{m}_{air}/\dot{m}_{air\_naturally\ induced}$)	Δ (PCT-$PCT_{naturally\ induced}$) (K)
0 (naturally induced)	$6.32x10^{-2}$	1		$4.11x10^{-2}$	
0.45 (1.0)	$6.34x10^{-2}$	1.0026		$4.12x10^{-2}$	
0.89 (2.0)	$5.55x10^{-2}$	0.8783		$3.86x10^{-2}$	
1.34 (3.0)	$4.99x10^{-2}$	0.7892		$3.68x10^{-2}$	
1.79 (4.0)	$4.49x10^{-2}$	0.7105		$3.52x10^{-2}$	
2.24 (5.0)	$4.05x10^{-2}$	0.6403		$3.37x10^{-2}$	
2.68 (6.0)	$3.74x10^{-2}$	0.5923	-3.5	$3.27x10^{-2}$	14
3.17 (7.1)	$3.65x10^{-2}$	0.5779		$3.25x10^{-2}$	
3.58 (8.0)	$3.56x10^{-2}$	0.5636		$3.22x10^{-2}$	
4.02 (9.0)	$3.54x10^{-2}$	0.5599		$3.21x10^{-2}$	
4.47 (10.0)	$3.54x10^{-2}$	0.5605		$3.21x10^{-2}$	
4.92 (11.0)	$3.53x10^{-2}$	0.5580		$3.20x10^{-2}$	
5.32 (11.9)	$3.56x10^{-2}$	0.5625	-8	$3.21x10^{-2}$	14

Table 4-10 Simulation, Experimental and validation Errors for (800 kPa, 5 kW) Crosswind Cases

	Simulation Error	Experimental Error	Validation Error
Δ (PCT- $PCT_{naturally\ induced}$) (K)	23	14	27
Δ ($\dot{m}_{air}/\dot{m}_{air\_naturally\ induced}$)	0.130	0.056	0.142

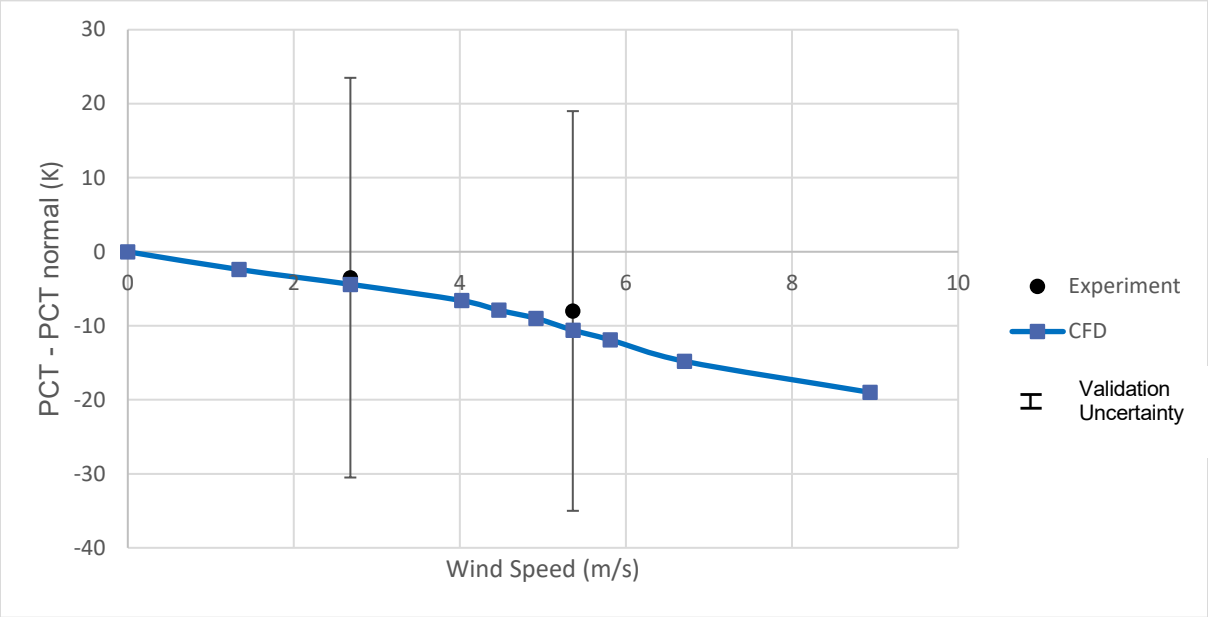

Figure 4-49 PCT Change as Function of Crosswind Speed for the Underground (800 kPa, 5 kW) Cases

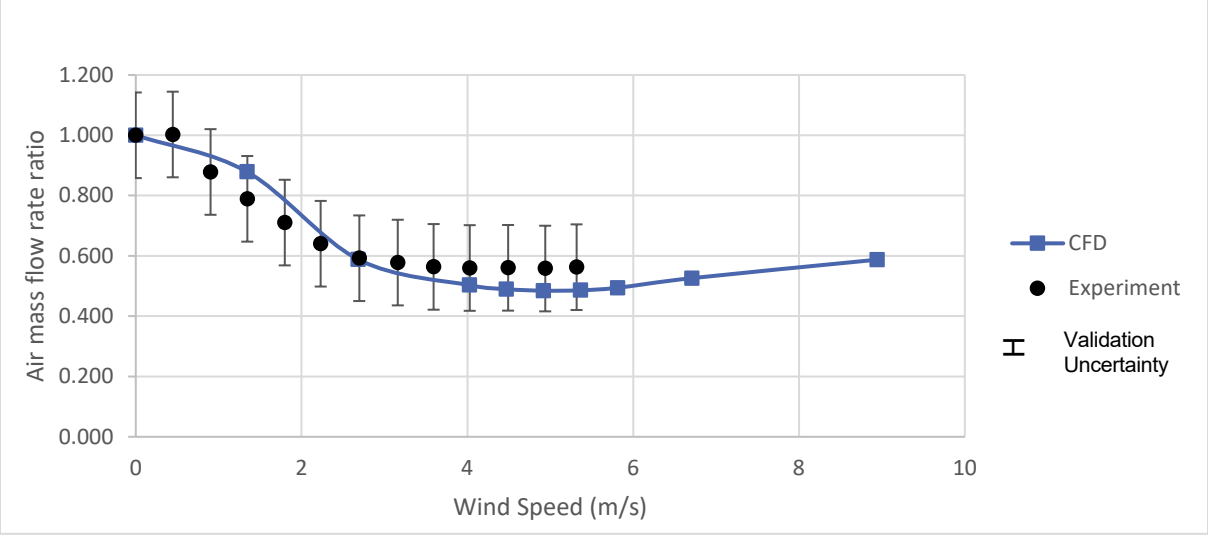

Figure 4-50 Inlet Air Mass Flow Rate Ratio Change as Function of Crosswind Speed for the Underground (800 kPa, 5 kW) Cases

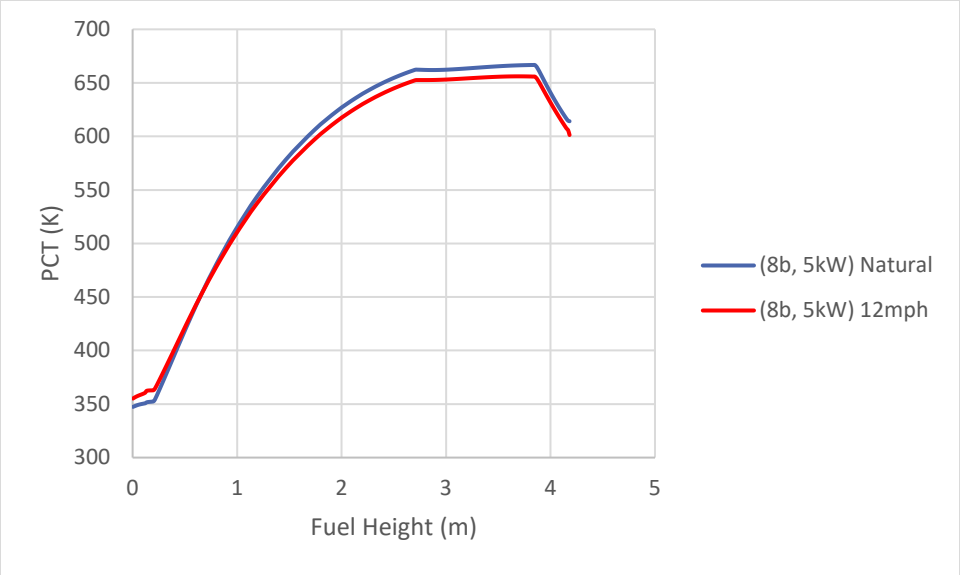

Figure 4-51 PCT as a function of height for the (800 kPa, 5 kW) Cases for Natural and Crosswind at 5.36 m/s (12 mph)

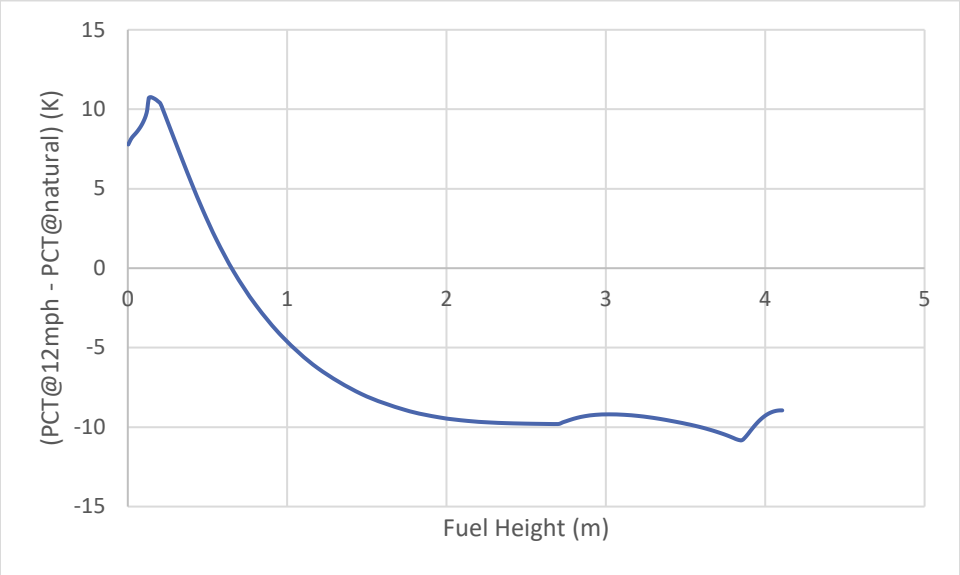

Figure 4-52 Delta PCT as a Function of Height for the (800 kPa, 5 kW) Cases for Natural and Crosswind at 5.36 m/s (12 mph)

4.3.2 Crosswind (100 kPa, 5 kW) Cases

4.3.2.1 Steady State

Table 4-11 Steady-State CFD for Underground with Crosswind at (100 kPa, 5 kW)

Wind Speed in m/s (mph)	PCT (K)	$\dot{m}_{air}$ (kg/sec)	(PCT-$PCT_{naturally\ induced}$) (K)	$\dot{m}_{air}/\dot{m}_{air\_naturally\ induced}$	Δ (PCT-$PCT_{naturally\ induced}$) (K)	Δ ($\dot{m}_{air}/\dot{m}_{air\_naturally\ induced}$)
0 (naturally induced)	713	$6.74x10^{-2}$	0.0	1.000	23.34	$7.01x10^{-2}$
1.34 (3)	715	$6.06x10^{-2}$	2.3	0.900	23.34	$6.66x10^{-2}$
2.68 (6)	719	$4.74x10^{-2}$	6.4	0.704	23.34	$5.98x10^{-2}$
4.02 (9)	723	$3.44x10^{-2}$	10.3	0.511	23.34	$5.30x10^{-2}$
4.47 (10)	723	$3.27x10^{-2}$	10.8	0.486	23.34	$5.21x10^{-2}$
4.92 (11)	724	$3.21x10^{-2}$	11.2	0.476	23.34	$5.18x10^{-2}$
5.36 (12)	723	$3.25x10^{-2}$	11.0	0.482	23.34	$5.20x10^{-2}$
5.81 (13)	723	$3.33x10^{-2}$	10.7	0.494	23.34	$5.24x10^{-2}$
6.71 (15)	722	$3.45x10^{-2}$	9.1	0.512	23.34	$5.30x10^{-2}$
8.94 (20)	721	$3.66x10^{-2}$	8.0	0.543	23.34	$5.41x10^{-2}$

Table 4-12 Steady-State Experiment for Underground with Crosswind at (100 kPa, 5 kW)

Wind Speed in m/s (mph)	$\dot{m}_{air}$ (kg/sec)	(PCT-$PCT_{naturally\ induced}$) (K)	$\dot{m}_{air}/\dot{m}_{air\_naturally\ induced}$	Δ (PCT-$PCT_{naturally\ induced}$) (K)	Δ ($\dot{m}_{air}/\dot{m}_{air\_naturally\ induced}$)
0 (naturally induced)	$7.16x10^{-2}$		1		$3.63x10^{-2}$
0.45 (1.0)	$7.19x10^{-2}$		1.0044		$3.64x10^{-2}$
0.89 (2.0)	$6.43x10^{-2}$		0.8977		$3.45x10^{-2}$
1.34 (3.0)	$5.73x10^{-2}$	1.7	0.8004	14	$3.27x10^{-2}$
1.83 (4.1)	$5.30x10^{-2}$		0.7410		$3.16x10^{-2}$
2.28 (5.1)	$4.82x10^{-2}$		0.6735		$3.04x10^{-2}$
2.68 (6.0)	$4.48x10^{-2}$	3.7	0.6252	14	$2.95x10^{-2}$
3.17 (7.1)	$4.32x10^{-2}$		0.6037		$2.91x10^{-2}$
3.58 (8.0)	$4.20x10^{-2}$		0.5872		$2.88x10^{-2}$
3.98 (8.9)	$4.17x10^{-2}$		0.5823		$2.87x10^{-2}$
4.47 (10.0)	$4.19x10^{-2}$		0.5850		$2.88x10^{-2}$
4.92 (11.0)	$4.17x10^{-2}$		0.5826		$2.87x10^{-2}$
5.28 (11.8)	$4.22x10^{-2}$	6	0.5901	14	$2.89x10^{-2}$

Table 4-13 Simulation, Experimental and validation Errors for (100 kPa, 5 kW) Crosswind Cases

	Simulation Error	Experimental Error	Validation Error
Δ (PCT- $PCT_{naturally\ induced}$) (K)	23	14	27
Δ ($\dot{m}_{air}/\dot{m}_{air\_naturally\ induced}$)	0.130	0.056	0.142

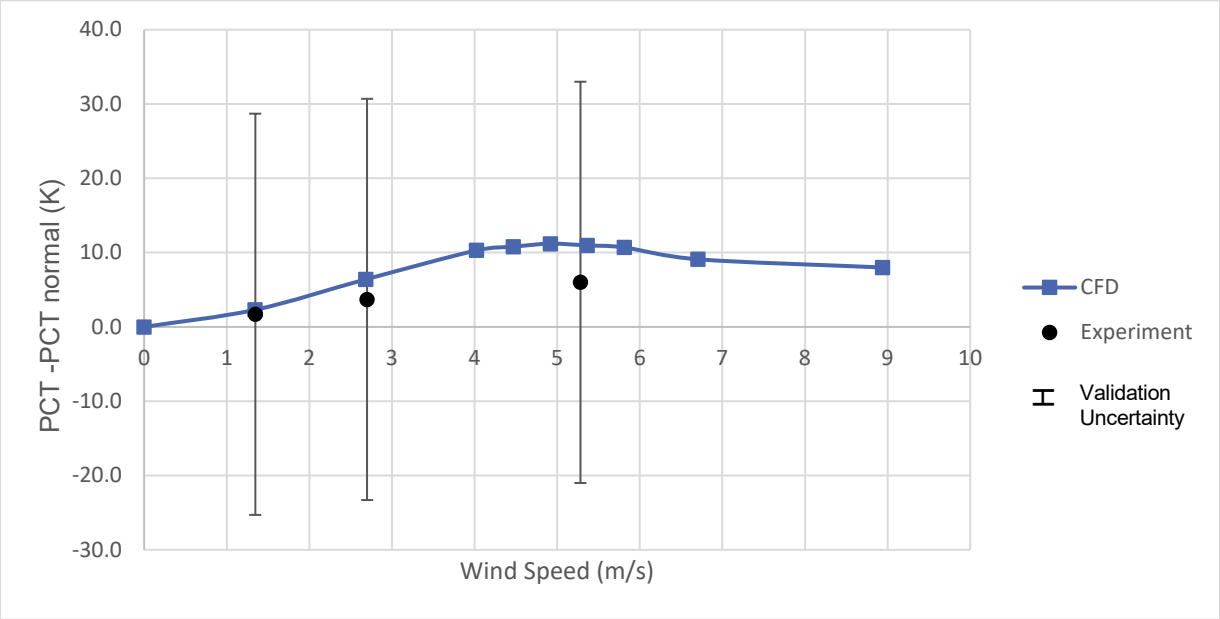

Figure 4-53 PCT Change as Function of Crosswind Speed for the Underground (100 kPa, 5 kW) Cases

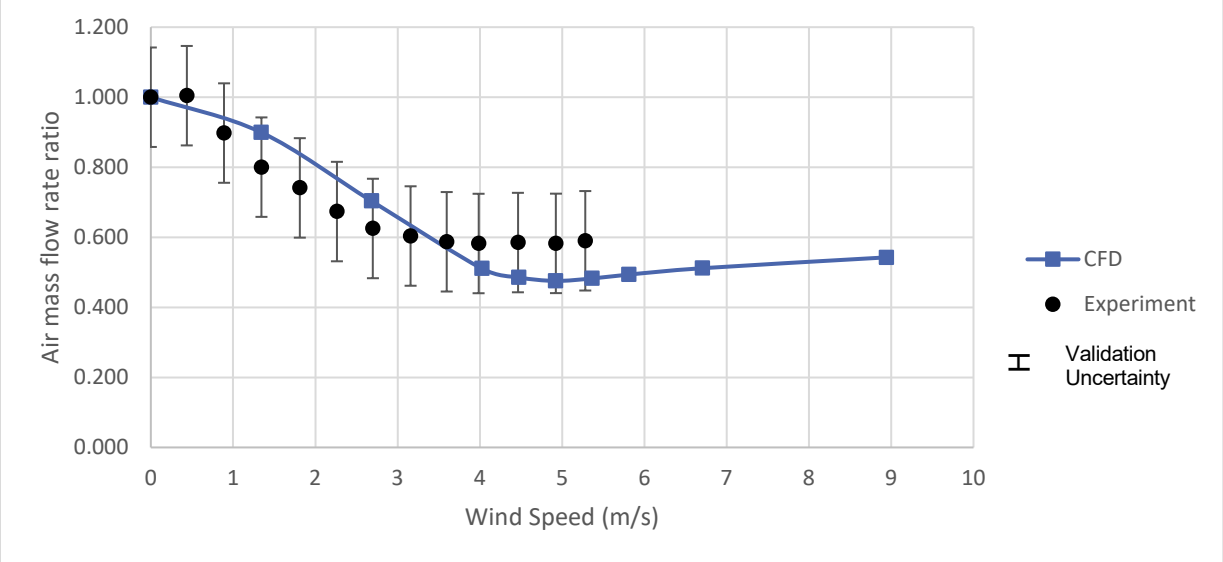

Figure 4-54 Inlet Air Mass Flow Rate Ratio Change as Function of Crosswind Speed for the Underground (100 kPa, 5 kW) Cases

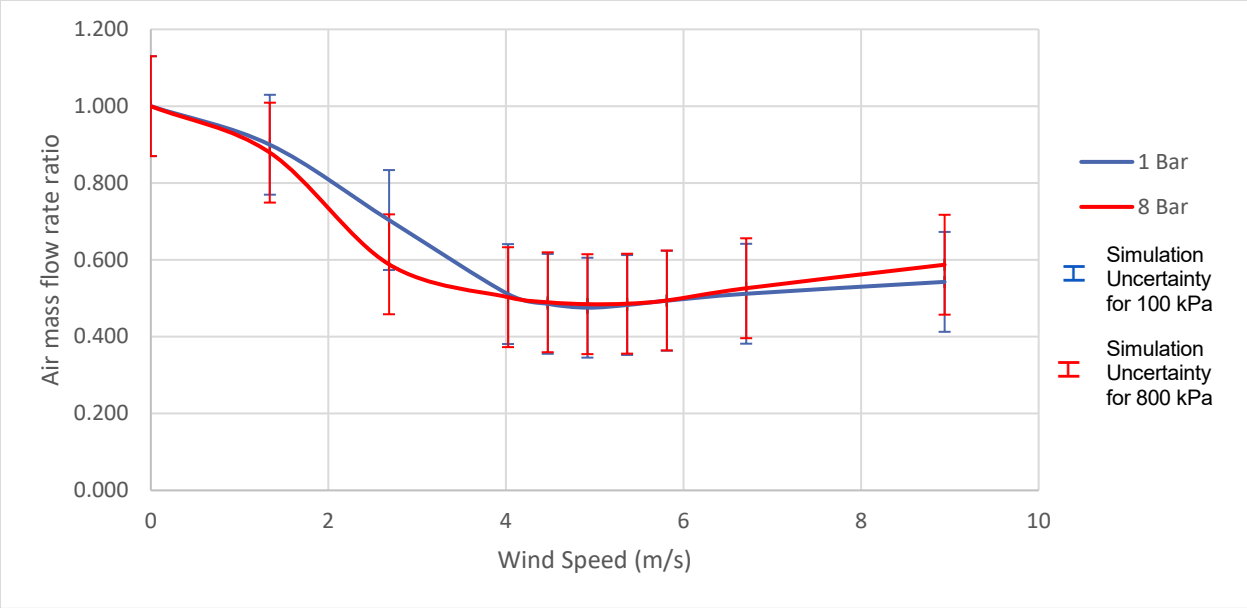

Figure 4-55 Inlet Air Mass Flow Rate Ratio Change as Function of Crosswind Speed for the Underground (100 kPa, 5 kW) and (800 kPa, 5 kW) Cases

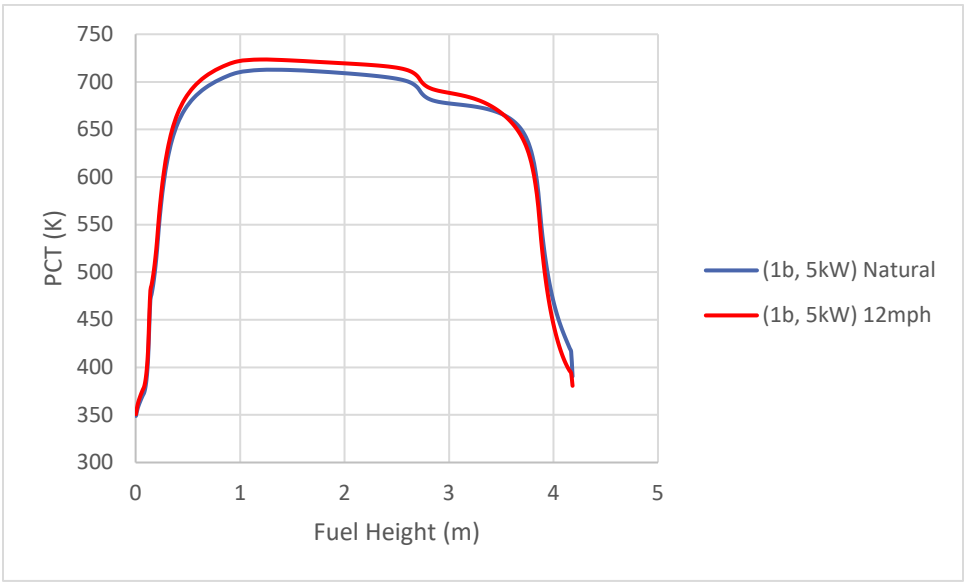

Figure 4-56 PCT as a Function of Height for the (100 kPa, 5 kW) Cases for Natural and Crosswind at 5.36 m/s (12 mph)

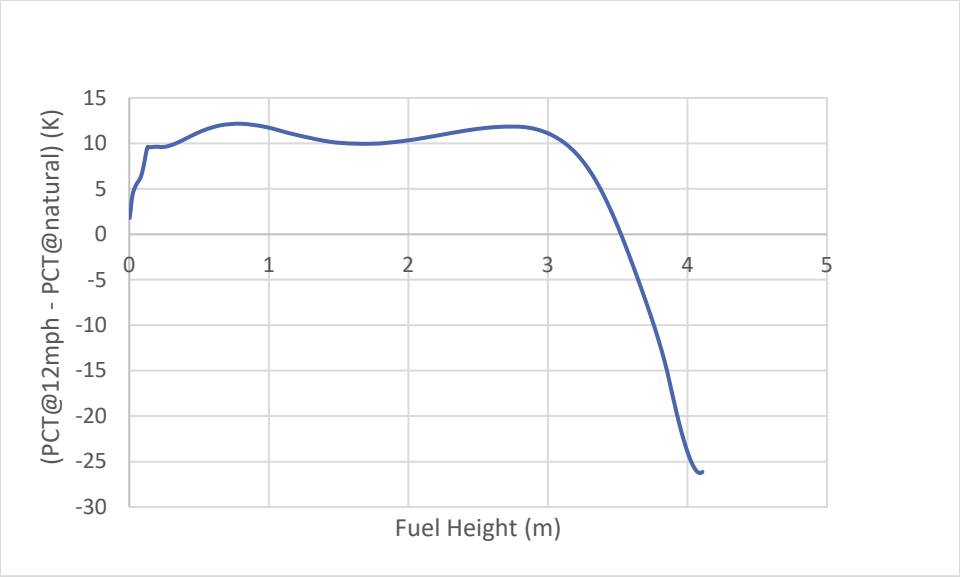

Figure 4-57 Delta PCT as a Function of Height for the (100 kPa, 5 kW) Cases for Natural and Crosswind at 5.36 m/s (12 mph)

4.3.2.2 Transient

Table 4-14 Transient CFD for Underground with Crosswind at (100 kPa, 5 kW) at 5.36 m/s (12 mph)

Time (hrs.)	$\dot{m}_{air}$ (kg/sec)	PCT (K)	$\dot{m}_{air}/\dot{m}_{air\_naturally\ induced}$	(PCT-PCT$_{naturally\ induced}$) (K)
0	0.074060	712.5	1.0000	0.0
2	0.032587	715.1	0.4400	2.6
4	0.032951	718.6	0.4449	6.1
6	0.031769	720.8	0.4290	8.3
8	0.031242	722.0	0.4218	9.5
10	0.031627	722.8	0.4270	10.3
12	0.031629	723.1	0.4271	10.6
14	0.031639	723.2	0.4272	10.7
16	0.031566	723.3	0.4262	10.8
18	0.031938	723.4	0.4312	10.9
20	0.031532	723.4	0.4258	10.9
25	0.032136	723.4	0.4339	10.9
30	0.031409	723.4	0.4241	10.9
40	0.031627	723.4	0.4270	10.9
50	0.031484	723.4	0.4251	10.9

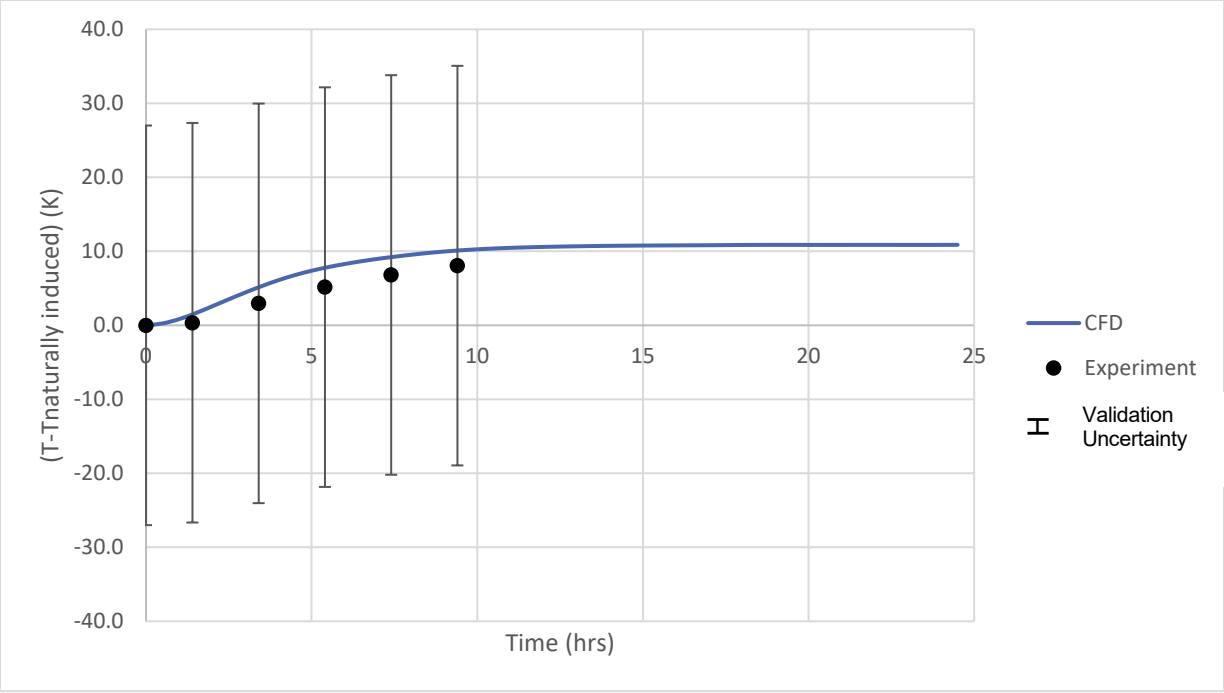

Figure 4-58 PCT Difference as a Function of Time for the (100 kPa, 5 kW) Case at a Crosswind Speed of 5.36 m/s (12 mph)

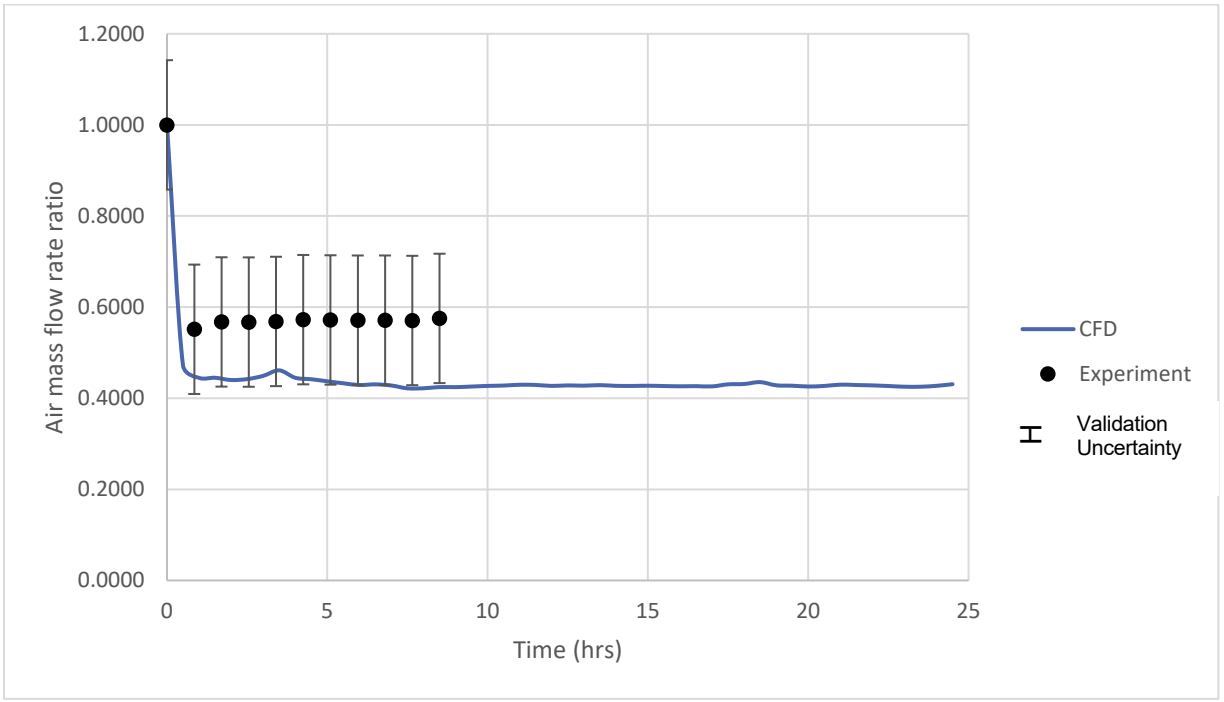

Figure 4-59 Inlet Air Mass Flow Rate Ratio as a Function of Time for the (100 kPa, 5 kW) Case at a Crosswind Speed of 5.36 m/s (12 mph)

As demonstrated in the experiment, crosswinds can affect the DCS thermal performance. When the crosswind is blowing straight on the inlet and outlet vents, air flow is blocked at the outlet vents but augmented through the inlet vents. At lower velocities, these two opposing actions of crosswind will restrict the flow overall.

The overall resistance to flow imposed by the wind will reduce the air mass flow rate when compared to the naturally induced air flow. At higher wind speeds, the air mass flow rate downward trend stops, and the flow through the DCS starts to increase. Depending on the case, there is a critical crosswind speed at which the air mass flow rate eventually starts to increase. These critical wind speeds can vary between 2.25 and 6.7 m/s (5 and 15 mph), depending on the cask configuration and environmental conditions.

CFD predictions in previous analyses as documented in NUREG-2174 [14] predicted a critical wind speed of 3.6 m/s (8 mph). As such, before the critical wind speed, less air is available to cool the dry cask and higher PCTs are expected. At the critical wind speed, the air mass flow rate reaches its lowest and the PCT is at its highest value. At speeds higher than the critical wind speed, the air mass flow rate starts to increase, and PCT starts to decrease. As shown in Figure 4-50, Figure 4-54, and Figure 4-55 for both cases (800 kPa, 5 kW) and (100 kPa,5 kW), the air mass flow rate is reduced by as much as 50 percent of the naturally induced case at the critical crosswind speed of close to 5.4 m/s (12 mph). Similar reduction of the air mass flow was obtained in earlier predictions [14]. For both cases, the CFD prediction of the air mass flow ratio compares very favorably with the obtained experimental data. The predicted and experimental air mass flow rate ratios are within the calculated uncertainty as shown in Figure 4-50, Figure 4-54, and Figure 4-55.

For the (100 kPa, 5 kW) case, the maximum PCT was reached at the critical crosswind speed of around 5.4 m/s (12 mph), when the air mass flow rate reached its minimum. Thereafter, PCT started decreasing due to the increase of air mass flow rate through the DCS. At around 5.4 m/s (12 mph), the PCT increased by 10 K. In previous CFD predictions for underground configurations designed by cask applicants [14], PCT increased by as much as 50 K for a crosswind speed of 5 mph. If the DCS had used a prototypical thick overpack, a much higher PCT change would be predicted.

The DCS shells (i.e., shell1 and shell2), as shown in Figure 1-4, were fabricated using a thin stainless-steel sheet to mimic the overpack. When wind was blowing at the thin stainless-steel sheet, this metal jacket was cooled, and eventually the cooling effect reached the fuel region. For the (800 kPa, 5 kW) case, the PCT slightly decreased as the crosswind increased from 0–8.95 m/s (0 to 20 mph). PCT never increased, even at the critical point at a crosswind speed of 5.4 m/s (12 mph). The PCT for the case of (800 kPa, 5 kW) is at the top of the fuel region, as shown in Figure 4-51, while the PCT location for the case of (100 kPa, 5 kW) is at the middle half, between 1/3rd and 2/3rd of the fuel height, as shown in Figure 4-56. As the PCT location for the high-pressure case is closer to the wind blowing machine, and the overpack consists of a thin stainless-steel sheet, the PCT decreased as shown in Figure 4-51 and Figure 4-52. The cooling effect at a crosswind of 5.4 m/s (12 mph) is also present in the lower pressure case (100 kPa, 5 kW) as shown in Figure 4-56, but it was not able to reach the location of the PCT. The cooling effect for the (100 kPa, 5 kW) case was observed at a height of 3.5 m as shown in Figure 4-56 and Figure 4-57. Similarly, in the (800 kPa, 5 kW) case, the cooling effect was observed at a height of 0.7 m as shown in Figure 4-51 and Figure 4-52.

As shown in Figure 4-58 and Figure 4-59 for the (100 kPa, 5 kW) transient case, the air mass flow rate reaches steady-state values sooner than the PCT. The air mass flow rate reached

95 percent of its steady-state value in 2 hours, while the PCT reached the same level in 12 hours. Due to the time constraint, the DCS experiment [6] used this fact to obtain the air mass flow rate for a crosswind speed of between 0 and 5.4 m/s (12 mph), using 3-hour intervals with a constant wind speed.

5 CONCLUSIONS

A CFD validation of data collected using a DCS followed guidelines from NUREG-2152 [13] and ASME V&V 20-2009 [2]. The DCS, a test apparatus simulating the fuel compartment of a dry cask, was constructed and operated to produce first-of-a-kind, high-fidelity transient and steady-state thermal-hydraulic data sets suitable for CFD model validation (i.e., CFD-quality data). The experiment tested configurations for both vertical aboveground and underground storage cask systems and validated the CFD models successfully. A wind machine also tested the effect of wind speed on the PCT and induced air mass flow rate in the underground configuration and validated them successfully. Over 40 unique data sets were collected and analyzed for these efforts. This report covered most of the measured data, to diligently validate the thermal model that the NRC uses for dry cask applications.

CFD analyses were performed for all 14 experimental cases with the DCS apparatus in the aboveground configuration. Complete validation, including UQ using ASME V&V 20-2009 [2], was performed for eight of these cases. Similarly, CFD cases were run for all 14 tests, with the DCS apparatus in the underground configuration. Complete validation, including UQ using ASME V&V 20-2009, was obtained for eight of these cases. Steady-state analysis was used to make CFD predictions for both configurations (i.e., 28 cases). These cases included different power levels, including 0.5, 1.0, 2.5, and 5.0 kW. The helium pressures inside the pressure vessel were sub-atmospheric (0.3 kPa), 100, 450, and 800 kPa absolute. CFD analyses were performed for 21 cases using the crosswind machine with the DCS apparatus in the underground configuration. The effect of crosswind velocity (from naturally induced to 5.4 m/s) on the induced air mass flow rate was measured using the highest used power of 5.0 kW and two helium pressures (100 kPa and 800 kPa).

This report has demonstrated that the CFD simulation results of the DCS thermal model are within the calculated validation uncertainties of the experimental data measured at Sandia National Laboratories. Moreover, the process outlined here demonstrates the process by which simulation uncertainty can be quantified, as outlined in ASME V&V 20-2009 [2], for a complex, real-world application.

The performances of the aboveground and underground DCS were similar, as expected, and can be summarized as follows:

- All steady-state peak temperatures and induced air mass flow rates increased with increasing assembly power.
- PCTs decreased with increasing internal helium pressure for a given assembly power, indicating increased internal convection for pressurized vessels.
- The location of the PCT moved from near the top of the assembly to approximately 1/3 the height of the assembly for the highest (800 kPa absolute) to the lowest (0.3 kPa absolute) pressure studied, respectively. This shift in PCT location is consistent with convective heat transfer increasing with internal helium pressure.
- The highest average steady-state PCT was 715 K for 5.0 kW and 100 kPa helium pressure. This temperature was in the range of the NRC limits for allowable PCT of 673 K for normal operation and 843 K for off-normal operation [12].

- For the crosswind test series, as the wind speed increased from zero, the normalized air mass flow rate rapidly dropped to a minimum of between 0.45 and 0.5 at a crosswind speed between 2.5 and 5.0 m/s and then slowly increased as the crosswind speed increased further.

The typical certification process [17] requires that the applicant demonstrate compliance under the worst-case scenarios. In the case of dry cask storage, the PCT must remain below the safe operating limits of the materials under the hottest ambient conditions that are expected to occur at a particular site. Using the same line of thinking, the simulation inputs (e.g., decay heat, ambient temperature, emissivity) would all be chosen as conservatively bounding values that would yield a PCT value that is equal to or greater than the actual PCT value. This type of approach provides reasonable assurance of the safe operation of the dry cask system.

When using the best estimate inputs for the DCS provided by Sandia National Laboratories for a validation test, consisting of the base CFD model and UQ, the simulation results predicted the experimental measurements very favorably for all the cases within the validation uncertainty. In fact, the thermal model used by the NRC for this validation work in this report predicted the PCTs and induced air mass flow rates for a majority of the cases within the experimental uncertainty, which is significantly lower than the validation uncertainty. In some cases, even with no discrepancy between CFD prediction and the data from the experiment. This ultimate finding yields confidence in the model choices used to create the CFD thermal model used by the NRC.

The highest PCT difference between the CFD prediction and experimental data was 13 K, obtained for the aboveground configuration under sub-atmospheric (i.e. 0.3 kPa) conditions with 1 kW power. A validation uncertainty of 15.5 K was calculated for this case. The highest air mass flow rate difference between the CFD prediction and experimental data was 1.5×10^{-3} kg/s, obtained for the aboveground configuration for the (450 kPa, 1 kW) case. The validation uncertainty for this case was not calculated, but the experimental uncertainty of 1.5×10^{-3} kg/s was provided in NUREG/CR-7250 [6]. The validation uncertainty for this case will be expected to be higher than the experimental uncertainty. The experimental uncertainty will be combined with the simulation uncertainty to obtain the validation uncertainty, as illustrated in Chapter 3.

A calculated PCT validation uncertainty varying between 10.7 K and 13.6 K for pressurized-helium cases and spanning between 15.5 K and 18.2 K for the sub-atmospheric (i.e. 0.3 kPa) cases were obtained. An air mass flow rate validation uncertainty varying between 1.5×10^{-3} kg/s and 1.93×10^{-3} kg/s was calculated for pressurized-helium cases, and between 1.32×10^{-3} kg/s and 1.83×10^{-3} kg/s for the sub-atmospheric (i.e. 0.3 kPa) cases. The maximum validation uncertainty of the PCT and air mass flow rate represents 2.5 percent and 2.8 percent of the maximum measured PCT and air mass flow rate. The calculated validation uncertainties are a small fraction of the maximum PCT, and the mass flow rate measured in the experiment. As such, this experiment can be classified as a CFD-grade experiment.

Cask vendors have been submitting applications within margins in the range of about 10 to 20 degrees C (18-36 °F) from the ISG-11 temperature limit of 400 degrees C. A validation experiment would be useful and successful if it can improve the model's capabilities. This can be achieved, if it is demonstrated that the accuracy of the CFD thermal model using the validation uncertainty is less than or equal to this margin of 10 to 20 degrees C (18 – 36 °F).

A validation experiment would also be useful and successful if it can improve the model's capabilities. This can be achieved by demonstrating that the accuracy of the CFD thermal

model using the validation uncertainty is as minimal as possible. Designs that are complex enough to benefit from CFD modeling generally have a great many inputs that influence the simulation result. CFD-grade experiments are those that precisely measure each one of these inputs so that the input uncertainty of the simulation can be minimized. It is a difficult and complicated task to design and conduct such an experiment, even for relatively simple configurations, which is why so few are conducted. However, to gain confidence in the application of CFD as a tool in the certification process, especially with more complex physics, validation exercises such as this are necessary. The experimental data collected in this program were geared toward obtaining a CFD-grade experiment. The main objective of the CFD-grade experiment is the minimization of the validation uncertainty and hence, the improvement of the CFD thermal model. When a thermal model is well validated, the dry cask applicants and thermal reviewers will have confidence in the predicted margin even when it is minimized without exceeding the set limit. This report shows that a well-crafted, best estimate thermal model is a model that is implemented using the design basis following CFD best practice guidelines and complemented by UQ. Such a model will have enough information for dry cask applicants and thermal reviewers on the margins that can be considered safe for applications and certifications. A range of 10-14 K for the validation uncertainty was calculated for the helium-filled canister DCS experiment.

The method presented here, using a best estimate analysis that consisted of a base-case CFD thermal model, complemented by UQ, showed that the PCT and air mass flow rate for all the cases were predicted within the calculated validation uncertainty bands, as shown in the result sections. As such, the CFD models and inputs that were used in the DCS modeling approach as suggested in CFD best practice guidelines [13] were successfully validated using the data obtained for the DCS experiment at Sandia National Laboratories. The validation uncertainty in this program consisted of a decay heat uncertainty input, which contributed to the increase of the validation uncertainty, especially for the low decay heat case, as shown in the uncertainty chapter (i.e. Chapter 3), results chapter (i.e. Chapter 4), and appendix A. As NRC certifies dry casks for a specific heat input, the uncertainty input from this variable will not be of concern. As such, the validation uncertainty, which also can be considered as margins to be kept from the limiting temperature, will decrease. Consequently, 10 K thermal margins can be considered acceptable if a best estimate CFD thermal model is used, consisting of the base case and UQ using CFD best practice guidelines. Based on this validation, the NRC has full confidence that the physical models and solver settings used in this thermal model will be able to predict dry cask thermal performance. Additionally, the UQ method for dry cask analysis should include the following:

- numerical uncertainty
  - discretization error
  - convergence errors
  - round-off errors
- input uncertainty, including wall thermal emissivity, porous media effective thermal conductivity (i.e., radial and axial), thermophysical properties for fluids and solids, BCs (i.e., ambient temperature, heat exchange with ambient, inlet BC, geometrical uncertainties (e.g., gaps, geometrical approximations))
- experimental uncertainty, in the case of validation

Often, the cask applicant uses the worst-case scenario to perform dry cask thermal analyses, especially when there are enough margins from the allowable PCT limit. However, when the cask is designed for higher decay heat, the PCT values are getting close to the limit, and the obtained margin is questionable, the method presented in this report to evaluate the UQ should be used as a guide to show compliance with the PCT limit. The method presented herein, when used properly, will inform the applicant and thermal reviewer about the right margin to have for any cask design. The worst-case scenario model is based on conservative input values using a phenomena identification and ranking table (PIRT). The right PIRT should include all the possible input variables and modeling settings with possible uncertainties. As such, the worst-case scenario model is a model that will consist of input choices that will impact the dry cask thermal performance negatively (i.e., each input variable will lead to a conservative PCT). The modeling uncertainty for this type of thermal model should only include numerical uncertainties. In this case, the safety margins will be defined at least by the numerical uncertainty given that the worst-case scenario thermal model followed CFD best practice guidelines as given and documented in NUREG-2152 [13].

6 REFERENCES

[1] "ANSYS Fluent User's Guide," January 2017.

[2] ASME V&V 20-2009, "Standard for Verification and Validation in Computational Fluid Dynamics and Heat Transfer," American Society of Mechanical Engineers, 2009.

[3] Bestion, D. et al, "Requirement for CFD-Grade Experiments for Nuclear Reactor Thermal-Hydraulics," Organisation for Economic Co-operation and Development, Nuclear Energy Agency, Committee on the Safety of Nuclear Installations, Working Group on Analysis and Management of Accidents, CFD group, 2019.

[4] Bestion, D. et al, "Review of Uncertainty Methods for Computational Fluid Dynamics Application to Nuclear Reactor Thermal Hydraulics," Organisation for Economic Co-operation and Development, Nuclear Energy Agency, Committee on the Safety of Nuclear Installations, Working Group on Analysis and Management of Accidents, CFD group, 2016.

[5] Durbin, S.G., E.R. Lindgren, A. Zigh, and J. Solis, "Description of Dry Cask Simulator for Measuring Internal and External Thermal-Hydraulic Performance," SAND2016-0176C, Trans. American Nuclear Society, New Orleans, LA, June 2016.

[6] Durbin, S.G. and E.R. Lindgren, "Thermal-Hydraulic Experiments Using a Dry Cask Simulator," NUREG/CR-7250, Sandia National Laboratories, Albuquerque, NM, October 2018.

[7] Hall K., A. Zigh., and J. Solis., "CFD Validation of Vertical Dry Cask Storage System," NUREG/CR-7260, Alden Research Laboratory, Inc., Holden, MA, May 2019.

[8] Lindgren, E.R., and S.G. Durbin, "Characterization of Thermal-Hydraulic and Ignition Phenomena in Prototypic, Full-Length Boiling Water Reactor Spent Fuel Pool Assemblies after a Complete Loss-of-Coolant Accident," NUREG/CR-7143, Sandia National Laboratories, Albuquerque, NM, April 2007.

[9] Lindgren, E.R., and S.G. Durbin, "Materials and Dimensional Reference Handbook for the Boiling Water Reactor Dry Cask Simulator," SAND2017-13058R, Sandia National Laboratories, Albuquerque, NM, November 2017.

[10] Pulido R.J.M., E.R. Lindgren, S.G. Durbin, A. Zigh, J. Solis, S.R. Suffield, D.J. Richmond, J.A. Fort, L.E. Herranz., F. Feria, J. Penalva, M. Lloret, M. Galban, J. Benavides, and G. Jimenez, "Modeling Validation Exercises Using the Dry Cask Simulator," SAND2019-6079 R, Sandia National Laboratories, Albuquerque, NM, May 2019.

[11] TRW Environmental Safety Systems, Inc., "Spent Nuclear Fuel Effective Thermal Conductivity Report," prepared for U.S. Department of Energy, Las Vegas, NV, July 11, 1996.

[12] U.S. NRC, "Cladding Considerations for the Transportation and Storage of Spent Fuel," Interim Staff Guidance-11, Rev. 3, U.S. Nuclear Regulatory Commission, Washington, DC, November 2003.

[13] U.S. NRC, NUREG-2152, "Computational Fluid Dynamics Best Practice Guidelines for Dry Cask Applications, Final Report," U.S. Nuclear Regulatory Commission, Washington, DC, March 2013.

[14] U.S. NRC, NUREG-2174, “Impact of Variation in Environmental Conditions on the Thermal Performance of Dry Storage Casks,” Office of Nuclear Regulatory Research and Office of Nuclear Material Safety and Safeguards, U.S. Nuclear Regulatory Commission, Washington, DC, March 2016.

[15] U.S. NRC, NUREG-2208, “Validation of Computational Fluid Dynamics Methods Using Prototypic Light Water Reactor Spent Fuel Assembly Thermal-Hydraulic Data,” Office of Nuclear Regulatory Research, U.S. Nuclear Regulatory Commission, Washington, DC, March 2017.

[16] U.S. NRC, NUREG-0800 “Standard Review Plan for the Review of Safety Analysis Reports for Nuclear Power Plants: LWR Edition,” U.S. Nuclear Regulatory Commission, Washington, DC.

[17] U.S. NRC, 10 CFR Par 72 *“Licensing Requirements for the Independent Storage of Spent Fuel Nuclear Fuel, High’Level Radioactive Waste, and Reactive-Related Greater than Class C Waste,”* U.S. Nuclear Regulatory Commission, Washington, DC

APPENDIX A
UNCERTAINTY QUANTIFICATION FOR OTHER CASES

A.1 Aboveground

A.1.1 Aboveground (800 kPa, 0.5 kW) Case

Table A-1 Overall Numerical and Input Uncertainty for PCT and $\dot{m}_{air}$ for the (800 kPa, 0.5kW) Aboveground Case

	PCT	$\dot{m}_{air}$ for One inlet Vent
Computer Round-off	± 0.0 K (0.0°F)	± 0 kg/s (0 lb/s)
Iterative Convergence	± 0.05 K (0.09°F)	± 1.140×10^{-5} kg/s (2.51×10^{-5} lb/s)
Discretization (GCI)	± 0.61 K (1.1°F)	± 1.442×10^{-4} kg/s (3.17×10^{-4} lb/s)
Numerical Uncertainty	± 0.66 K (1.19°F)	± 1.556×10^{-4} kg/s (3.42×10^{-4} lb/s)
Total Input Uncertainty	± 8 K (14.4°F)	± 4.502×10^{-4} kg/s (9.90×10^{-4} lb/s)

Table A-2 Simulation Uncertainty for PCT and $\dot{m}_{air}$ for the (800 kPa, 0.5 kW) Aboveground Case

	PCT	$\dot{m}_{air}$ for All the Vents
Simulation Uncertainty	±8 K (14.4°F)	±9.526×10^{-4} kg/s (2.096×10^{-3} lb/s)

Table A-3 Validation Uncertainty for PCT and $\dot{m}_{air}$ for the (800 kPa, 0.5 kW) Aboveground Case

	PCT	$\dot{m}_{air}$ for All the Vents
Experimental Uncertainty	± 7 K (12.6 °F)	±1.5×10^{-3} kg/s (3.3×10^{-3} lb/s)
Validation Uncertainty	± 10.6 K (19.1 °F)	±1.76×10^{-3} kg/s (3.872×10^{-3} lb/s)

A.1.2 Aboveground (450 kPa, 2.5 kW) Case

Table A-4 Overall Numerical and Input Uncertainty for PCT and $\dot{m}_{air}$ for the (450 kPa, 2.5 kW) Aboveground Case

	PCT	$\dot{m}_{air}$ for One inlet Vent
Computer Round-off	± 0 K	± 0 kg/s
Iterative Convergence	± 0.02 K	± 1.637×10^{-6} kg/s
Discretization (GCI)	± 0.733 K	±1.222×10^{-5} kg/s
Numerical Uncertainty	± 0.75 K (1.4°F)	± 1.386×10^{-5} kg/s (3.049×10^{-5} lb/s)
Total Input Uncertainty	± 8.6 K (15.5°F)	± 2.797×10^{-4} kg/s (6.153×10^{-4} lb/s)

Table A-5 Simulation Uncertainty for PCT and $\dot{m}_{air}$ for the (450 kPa, 2.5 kW) Aboveground Case

	PCT	$\dot{m}_{air}$ for All the Vents
Simulation Uncertainty	± 8.7 K (15.7 °F)	±5.601x10^{-4} kg/s (1.232x10^{-3} lb/s)

Table A-6 Validation Uncertainty for PCT and $\dot{m}_{air}$ for the (450 kPa, 2.5 kW) Aboveground Case

	PCT	$\dot{m}_{air}$ for All the Vents
Experimental Uncertainty	± 7 K (12.6 °F)	±1.5x10^{-3} kg/s (3.3x10^{-3} lb/s)
Validation Uncertainty	± 11.1 K (20 °F)	±1.582x10^{-3} kg/s (3.48x10^{-3} lb/s)

A.1.3 Aboveground (100 kPa, 5kW) Case

Table A-7 Overall Numerical and Input Uncertainty for PCT and $\dot{m}_{air}$ for the (100 kPa, 5 kW) Aboveground Case

	PCT	$\dot{m}_{air}$ for One inlet Vent
Computer Round-off	± 0 K	± 0 kg/s
Iterative Convergence	± 0.001 K	± 3.739x10^{-7} kg/s
Discretization (GCI)	± 0.037 K	± 2.444x10^{-4} kg/s
Numerical Uncertainty	± 0.038 K (0.07 °F)	± 2.448x10^{-4}kg/s (5.3856x10^{-4} lb/s)
Total Input Uncertainty	± 11.7 K (21.1°F)	± 5.7x10^{-4} kg/s (1.254x10^{-3} lb/s)

Table A-8 Simulation Uncertainty for PCT and $\dot{m}_{air}$ for the (100 kPa, 5 kW) Aboveground Case

	PCT	$\dot{m}_{air}$ for All the Vents
Simulation Uncertainty	± 11.7 K (21.1 °F)	±1.241x10^{-3} kg/s (2.7302x10^{-3} lb/s)

Table A-9 Validation Uncertainty for PCT and $\dot{m}_{air}$ for the (100 kPa, 5 kW) Aboveground Case

	PCT	$\dot{m}_{air}$ for All the Vents
Experimental Uncertainty	± 7 K (12.6 °F)	±1.5x10^{-3} kg/s (3.3x10^{-3} lb/s)
Validation Uncertainty	± 13.6 K (24.5 °F)	±1.931x10^{-3} kg/s (4.2482x10^{-3} lb/s)

A.1.4 Aboveground (100 kPa, 2.5 kW) Case

Table A-10 Numerical Uncertainty for PCT and $\dot{m}_{air}$ for the (100 kPa, 2.5 kW) Aboveground Case

	PCT	$\dot{m}_{air}$ for One inlet Vent
Computer Round-off	± 0 K	± 0 kg/s
Iterative Convergence	± 0.0005 K	± 3.966×10^{-7} kg/s
Discretization (GCI)	± 1.47 K	± 1.222×10^{-5} kg/s
Numerical Uncertainty	± 1.47 K (2.6°F)	± 1.262×10^{-5} kg/s (2.7764×10^{-5} lb/s)
Total Input Uncertainty	± 9.2 K (16.6°F)	± 3.146×10^{-4} kg/s (6.921×10^{-4} lb/s)

Table A-11 Simulation Uncertainty for PCT and $\dot{m}_{air}$ for the (100 kPa, 2.5 kW) Aboveground Case

	PCT	$\dot{m}_{air}$ for All the Vents
Simulation Uncertainty	±9.34 K (16.8 °F)	±6.297×10^{-4} kg/s (1.385×10^{-3} lb/s)

Table A-12 Validation Uncertainty for PCT and $\dot{m}_{air}$ for the (100 kPa, 2.5 kW) Aboveground Case

	PCT	$\dot{m}_{air}$ for All the Vents
Experimental Uncertainty	± 7 K (12.6 °F)	±1.5×10^{-3} kg/s (3.3×10^{-3} lb/s)
Validation Uncertainty	± 11.7 K (21.1 °F)	±1.608×10^{-3} kg/s (3.5376×10^{-3} lb/s)

A.1.5 Aboveground (100 kPa, 0.5 kW) Case

Table A-13 Numerical Uncertainty for PCT and $\dot{m}_{air}$ for the (100 kPa, 0.5 kW) Aboveground Case

	PCT	$\dot{m}_{air}$ for One inlet Vent
Computer Round-off	± 0 K	± 0 kg/s
Iterative Convergence	± 0.038 K	± 1.212×10^{-5} kg/s
Discretization (GCI)	± 0.122 K	± 1.332×10^{-4} kg/s
Numerical Uncertainty	± 0.16 K (0.3°F)	± 1.453×10^{-4} kg/s (3.1966×10^{-4} lb/s)
Total Input Uncertainty	± 10.3 K (18.5°F)	± 5.047×10^{-4} kg/s (1.1×10^{-3} lb/s)

Table A-14 Simulation Uncertainty for PCT and $\dot{m}_{air}$ for the (100 kPa, 0.5 kW) Aboveground Case

	PCT	$\dot{m}_{air}$ for One inlet Vent
Simulation Uncertainty	± 10.3 K (18.5 °F)	±1.05×10^{-3} kg/s (2.31×10^{-3} lb/s)

Table A-15 Validation Uncertainty for PCT and $\dot{m}_{air}$ for the (100 kPa, 0.5 kW) Aboveground Case

	PCT	$\dot{m}_{air}$ for All the Vents
Experimental Uncertainty	± 7 K (12.6 °F)	±1.5x10^{-3} kg/s (3.3x10^{-3} lb/s)
Validation Uncertainty	± 12.4 K (22.3 °F)	±1.815x10^{-3} kg/s (3.993x10^{-3} lb/s)

A.1.6 Aboveground (0.3 kPa, 1 kW) Case

Table A-16 Numerical Uncertainty for PCT and $\dot{m}_{air}$ for the Aboveground Case for the (0.3 kPa, 1 kW) Aboveground Case

	PCT	$\dot{m}_{air}$ for One inlet Vent
Computer Round-off	± 0 K	± 0 kg/s
Iterative Convergence	± 0.0007 K	± 1.791x10^{-6} kg/s
Discretization (GCI)	± 1.344 K	± 3.544x10^{-4} kg/s
Total Numerical Uncertainty	± 1.345 K (2.421°F)	± 3.562x10^{-4} kg/s (7.8364x10^{-4} lb/s)
Total Input Uncertainty	± 13.8 K (24.8°F)	± 3.033x10^{-4} kg/s (6.6726Ex10^{-4} lb/s)

Table A-17 Simulation Uncertainty for PCT and $\dot{m}_{air}$ for Aboveground Case for the (0.3 kPa, 1 kW) Aboveground Case

	PCT	$\dot{m}_{air}$ for All the Vents
Simulation Uncertainty	± 13.8 K (24.8°F)	±1.037x10^{-3} kg/s (2.2814x10^{-3} lb/s)

Table A-18 Validation Uncertainty for PCT and $\dot{m}_{air}$ for Aboveground Case for the (0.3 kPa, 1 kW) Aboveground Case

	PCT	$\dot{m}_{air}$ for All the Vents
Experimental Uncertainty	± 7 K (12.6 °F)	±1.5x10^{-3} kg/s (3.3x10^{-3} lb/s)
Validation Uncertainty	± 15.5 K (27.9 °F)	±1.807x10^{-3} kg/s (3.9754x10^{-3} lb/s)

A.1.7 Aboveground (0.3 kPa, 0.5 kW) Case

Table A-19 Numerical Uncertainty for PCT and $\dot{m}_{air}$ for the (0.3 kPa, 0.5 kW) Aboveground Case

	PCT	$\dot{m}_{air}$ for One inlet Vent
Computer Round-off	± 0 K	± 0 kg/s
Iterative Convergence	± 0.0008 K	± 9.045x10^{-6} kg/s
Discretization (GCI)	± 1.589 K	± 2.212x10^{-4} kg/s
Numerical Uncertainty	±1.589 K (2.9°F)	± 2.302x10^{-4} kg/s (5.0644x10^{-4} lb/s)
Total Input Uncertainty	± 16.6 K (29.9°F)	± 5.012x10^{-4} kg/s (1.1026x10^{-3} lb/s)

Table A-20 Simulation Uncertainty for PCT and $\dot{m}_{air}$ for the (0.3 kPa, 0.5 kW) Aboveground Case

	PCT	$\dot{m}_{air}$ for All the Vents
Simulation Uncertainty	± 16.7 K (30.1°F)	±1.103x10^{-3} kg/s (2.4266x10^{-3} lb/s)

Table A-21 Validation Uncertainty for PCT and $\dot{m}_{air}$ for the (0.3 kPa, 0.5 kW) Aboveground Case

	PCT	$\dot{m}_{air}$ for All the Vents
Experimental Uncertainty	± 7 K (12.6 °F)	±1.5x10^{-3} kg/s (3.3x10^{-3} lb/s)
Validation Uncertainty	± 18.1 K (32.5 °F)	±1.846x10^{-3} kg/s (4.0612x10^{-3} lb/s)

A.2 Underground

A.2.1 Underground (800 kPa, 5 kW) Case

Table A-22 Numerical Uncertainty for PCT and $\dot{m}_{air}$ for the (800 kPa, 5kW) Underground Case

	PCT	$\dot{m}_{air}$ for One inlet Vent
Computer Round-off	± 0 K	± 0 kg/s
Iterative Convergence	± 0.345 K	± 4.2641×10^{-6} kg/s
Discretization (GCI)	± 2.277 K	± 3.7948×10^{-4} kg/s
Numerical Uncertainty	± 2.6 K (4.7 °F)	± 3.84×10^{-4} kg/s (8.448×10^{-4} lb/s)
Total Input Uncertainty	± 10.2 K (18.4°F)	± 1.081×10^{-3} kg/s (2.3782×10^{-3} lb/s)

Table A-23 Simulation Uncertainty for PCT and $\dot{m}_{air}$ for the (800 kPa, 5 kW) Underground Case

	PCT	$\dot{m}_{air}$ for All the Vents
Simulation Uncertainty	± 10.5K (18.9°F)	±2.295×10^{-3} kg/s (5.049×10^{-3} lb/s)

Table A-24 Validation Uncertainty for PCT and $\dot{m}_{air}$ for the (800 kPa, 5 kW) UndergroundCase

	PCT	$\dot{m}_{air}$ for All the Vents
Experimental Uncertainty	± 7 K (12.6 °F)	±1.1×10^{-3} kg/s (2.42×10^{-3} lb/s)
Validation Uncertainty	± 12.6 K (22.7 °F)	±2.545×10^{-3} kg/s (5.599×10^{-3} lb/s)

A.2.2 Underground (800 kPa, 0.5 kW) Case

Table A-25 Numerical Uncertainty for PCT and $\dot{m}_{air}$ for the (800 kPa, 0.5 kW) Underground Case

	PCT	$\dot{m}_{air}$ for One inlet Vent
Computer Round-off	± 0 K	± 0 kg/s
Iterative Convergence	± 0.063 K	± 3.1864×10^{-6} kg/s
Discretization (GCI)	± 3.542 K	±4.0731×10^{-4} kg/s
Numerical Uncertainty	± 3.604 K (6.5 °F)	± 4.1×10^{-4} kg/s (9.02×10^{-4} lb/s)
Total Input Uncertainty	± 8.15 K (14.7°F)	± 6.915×10^{-4} kg/s (1.5213×10^{-3} lb/s)

Table A-26 Simulation Uncertainty for PCT and $\dot{m}_{air}$ for the (800 kPa, 0.5 kW) Underground Case

	PCT	$\dot{m}_{air}$ for All the Vents
Simulation Uncertainty	± 8.9K (16°F)	±1.608x10^{-3} kg/s (3.5376x10^{-3} lb/s)

Table A-27 Validation Uncertainty for PCT and $\dot{m}_{air}$ for the (800 kPa, 0.5 kW) Underground Case

	PCT	$\dot{m}_{air}$ for All the Vents
Experimental Uncertainty	± 7 K (12.6 °F)	±1.1x10^{-3} kg/s (2.42x10^{-3} lb/s)
Validation Uncertainty	± 11.3 K (20.3 °F)	±1.949x10^{-3} kg/s (4.2878x10^{-3} lb/s)

A.2.3 Underground (450 kPa, 2.5 kW) Case

Table A-28 Numerical Uncertainty for PCT and $\dot{m}_{air}$ for the (450 kPa, 2.5 kW) Underground Case

	PCT	$\dot{m}_{air}$ for One inlet Vent
Computer Round-off	± 0 K	± 0 kg/s
Iterative Convergence	± 0.10 K	± 6.2153x10^{-6} kg/s
Discretization (GCI)	± 3.67 K	± 2.5299x10^{-4} kg/s
Numerical Uncertainty	± 3.77 K (6.8 °F)	± 2.59x10^{-4} kg/s (5.698x10^{-4} lb/s)
Total Input Uncertainty	± 8.7 K (15.7°F)	± 9.174x10^{-4} kg/s (2.0183x10^{-3} lb/s)

Table A-29 Simulation Uncertainty for PCT and $\dot{m}_{air}$ for the (450 kPa, 2.5 kW) Underground Case

	PCT	$\dot{m}_{air}$ for All the Vents
Simulation Uncertainty	±9.5 K (17.1°F)	±1.907x10^{-3} kg/s (4.1954x10^{-3} lb/s)

Table A-30 Validation Uncertainty for PCT and $\dot{m}_{air}$ for the (450 kPa, 2.5 kW) Underground Case

	PCT	$\dot{m}_{air}$ for All the Vents
Experimental Uncertainty	± 7 K (12.6 °F)	±1.1x10^{-3} kg/s (2.42x10^{-3} lb/s)
Validation Uncertainty	± 11.8 K (21.2 °F)	±2.201x10^{-3} kg/s (4.8422x10^{-3} lb/s)

A.2.4 Underground (100 kPa, 5 kW) Case

Table A-31 Numerical Uncertainty for PCT and $\dot{m}_{air}$ for the (100 kPa, 5 kW) Underground Case

	PCT	$\dot{m}_{air}$ for One inlet Vent
Computer Round-off	± 0 K	± 0 kg/s
Iterative Convergence	± 0.002 K	± 8.35×10^{-7} kg/s
Discretization (GCI)	± 1.01 K	± 1.2649×10^{-4} kg/s
Numerical Uncertainty	± 1.01 K (1.8°F)	± 1.27×10^{-4} kg/s (2.794×10^{-4} lb/s)
Total Input Uncertainty	± 11.7 K (21.1°F)	± 1.175×10^{-3} kg/s (2.585×10^{-3} lb/s)

Table A-32 Simulation Uncertainty for PCT and $\dot{m}_{air}$ for the (100 kPa, 5 kW) Underground Case

	PCT	$\dot{m}_{air}$ for All the Vents
Simulation Uncertainty	±11.7 K (21.1 °F)	±2.364×10^{-3} kg/s (5.2008×10^{-3} lb/s)

Table A-33 Validation Uncertainty for PCT and $\dot{m}_{air}$ for the (100 kPa, 5 kW) Underground Case

	PCT	$\dot{m}_{air}$ for All the Vents
Experimental Uncertainty	± 7 K (12.6 °F)	±1.1×10^{-3} kg/s (2.42×10^{-3} lb/s)
Validation Uncertainty	± 13.6 K (24.5 °F)	±2.607×10^{-3} kg/s (5.7354×10^{-3} lb/s)

A.2.5 Underground (100 kPa, 2.5 kW) Case

Table A-34 Numerical Uncertainty for PCT and $\dot{m}_{air}$ for the (100 kPa, 2.5 kW) Underground Case

	PCT	$\dot{m}_{air}$ for One inlet Vent
Computer Round-off	± 0 K	± 0 kg/s
Iterative Convergence	± 0.0014 K	± 8.3507×10^{-7} kg/s
Discretization (GCI)	± 1.26 K	± 1.2649×10^{-5} kg/s
Numerical Uncertainty	± 1.27 K (2.3 °F)	± 1.35×10^{-5} kg/s (2.97×10^{-5} lb/s)
Total Input Uncertainty	± 9.2 K (16.6°F)	± 9.885×10^{-4} kg/s (2.1747×10^{-3} lb/s)

Table A-35 Simulation Uncertainty for PCT and $\dot{m}_{air}$ for the (100 kPa, 2.5 kW) Underground Case

	PCT	$\dot{m}_{air}$ for All the Vents
Simulation Uncertainty	± 9.3 K (16.7°F)	±1.977×10^{-3} kg/s (4.3494×10^{-3} lb/s)

Table A-36 Validation Uncertainty for PCT and $\dot{m}_{air}$ for the (100 kPa, 2.5 kW) Underground Case

	PCT	$\dot{m}_{air}$ for All the Vents
Experimental Uncertainty	± 7 K (12.6 °F)	±1.1x10^{-3} kg/s (2.42x10^{-3} lb/s)
Validation Uncertainty	± 11.6 K (20.9 °F)	±2.263x10^{-3} kg/s (4.9786x10^{-3} lb/s)

A.2.6 Underground (100 kPa, 0.5 kW) Case

Table A-37 Numerical Uncertainty for PCT and $\dot{m}_{air}$ for the (100 kPa, 0.5 kW) Underground Case

	PCT	$\dot{m}_{air}$ for One inlet Vent
Computer Round-off	± 0 K	± 0 kg/s
Iterative Convergence	± 0.007 K	± 2.7313x10^{-6} kg/s
Discretization (GCI)	± 0.38 K	± 1.0119x10^{-5} kg/s
Numerical Uncertainty	± 0.39K (0.7°F)	± 1.29 x10^{-5} kg/s (2.838x10^{-5} lb/s)
Total Input Uncertainty	± 10.5 K (18.9°F)	± 7.831x10^{-4} kg/s (1.7228x10^{-3} lb/s)

Table A-38 Total Simulation Uncertainty for PCT and $\dot{m}_{air}$ for the (100 kPa, 0.5 kW) Underground Case

	PCT	$\dot{m}_{air}$ for All the Vents
Simulation Uncertainty	± 10.5 K (18.9°F)	±1.566x10^{-3} kg/s (3.4452x10^{-3} lb/s)

Table A-39 Total Validation Uncertainty for PCT and $\dot{m}_{air}$ for the (100 kPa, 0.5 kW) Underground Case

	PCT	$\dot{m}_{air}$ for All the Vents
Experimental Uncertainty	± 7 K (12.6 °F)	±1.1x10^{-3} kg/s (2.42x10^{-3} lb/s)
Validation Uncertainty	± 12.6 K (22.7 °F)	±1.914x10^{-3} kg/s (4.2108x10^{-3} lb/s)

A.2.7 Underground (0.3 kPa, 1 kW) Case

Table A-40 Numerical Uncertainty for PCT and $\dot{m}_{air}$ for the (0.3 kPa, 1 kW) Underground Case

	PCT	$\dot{m}_{air}$ for One inlet Vent
Computer Round-off	± 0 K	± 0 kg/s
Iterative Convergence	± 0.01 K	± 6.5448x10^{-6} kg/s
Discretization (GCI)	± 1.39 K	± 1.0372x10^{-4} kg/s
Numerical Uncertainty	± 1.40 K (2.5 °F)	± 1.1x10^{-4} kg/s (2.42x10^{-4} lb/s)
Total Input Uncertainty	± 14. K (25.2°F)	± 6.482x10^{-4} kg/s (1.426x10^{-3} lb/s)

Table A-41 Simulation Uncertainty for PCT and $\dot{m}_{air}$ for the (0.3 kPa, 1 kW) Underground Case

	PCT	$\dot{m}_{air}$ for All the Vents
Simulation Uncertainty	±14 K (25.2°F)	±1.315x10^{-3} kg/s (2.893x10^{-3} lb/s)

Table A-42 Validation Uncertainty for PCT and $\dot{m}_{air}$ for the (0.3 kPa, 1 kW) Underground Case

	PCT	$\dot{m}_{air}$ for All the Vents
Experimental Uncertainty	± 7 K (12.6 °F)	±1.1x10^{-3} kg/s (2.42x10^{-3} lb/s)
Validation Uncertainty	± 15.7 K (28.2 °F)	±1.714x10^{-3} kg/s (3.7708 x10^{-3} lb/s)

A.2.8 Underground (0.3 kPa, 0.5 kW) Case

Table A-43 Numerical Uncertainty for PCT and $\dot{m}_{air}$ for the (0.3 kPa, 0.5 kW) Underground Case

	PCT	$\dot{m}_{air}$ for One inlet Vent
Computer Round-off	± 0 K	± 0 kg/s
Iterative Convergence	± 0.002 K	± 5.5594x10^{-6} kg/s
Discretization (GCI)	± 1.39 K	± 2.1504x10^{-5} kg/s
Numerical Uncertainty	± 1.39 K (2.5°F)	± 2.71x10^{-5} kg/s (5.962x10^{-5} lb/s)
Total Input Uncertainty	± 16.7 K (30.1°F)	± 7.901x10^{-4} kg/s (1.7382x10^{-3} lb/s)

Table A-44 Simulation Uncertainty for PCT and $\dot{m}_{air}$ for the (0.3 kPa, 0.5 kW) Underground Case

	PCT	$\dot{m}_{air}$ for All the Vents
Simulation Uncertainty	± 16.8 K (30.2°F)	±1.581x10^{-3} kg/s (3.4782x10^{-3} lb/s)

Table A-45 Validation Uncertainty for PCT and $\dot{m}_{air}$ for the (0.3 kPa, 0.5 kW) Underground Case

	PCT	$\dot{m}_{air}$ for All the Vents
Experimental Uncertainty	± 7 K (12.6 °F)	±1.1x10^{-3} kg/s (2.42x10^{-3} lb/s)
Validation Uncertainty	± 18.2 K (32.8 °F)	±1.926x10^{-3} kg/s (4.2372x10^{-3} lb/s)

APPENDIX B
RESULTS FOR OTHER CASES

B.1 Aboveground

B.1.1 Aboveground (450 kPa, 2.5 kW) Case

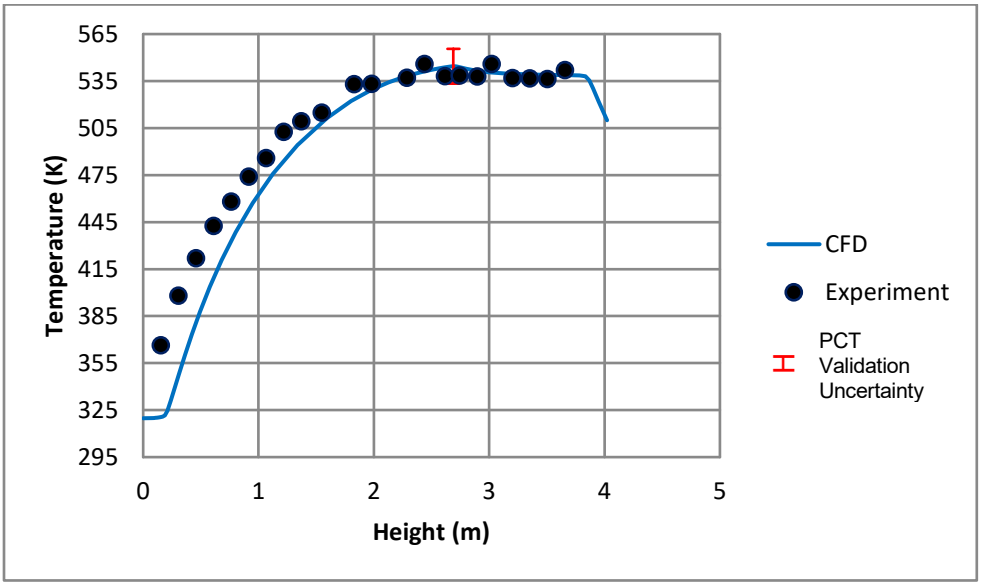

Figure B-1 PCT for the Aboveground (450 kPa, 2.5 kW) Case

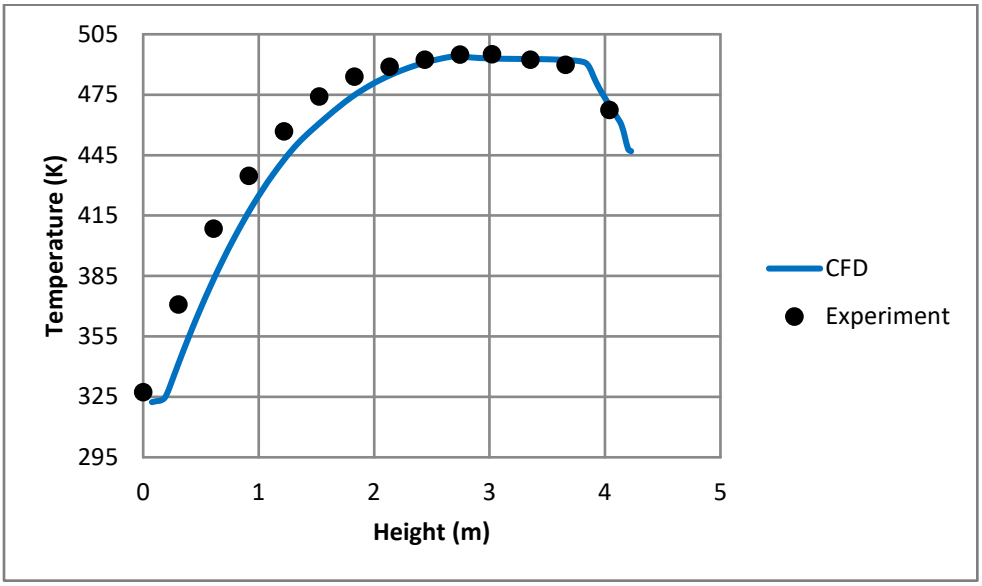

Figure B-2 Channel Box Temperature for the Aboveground (450 kPa, 2.5 kW) Case

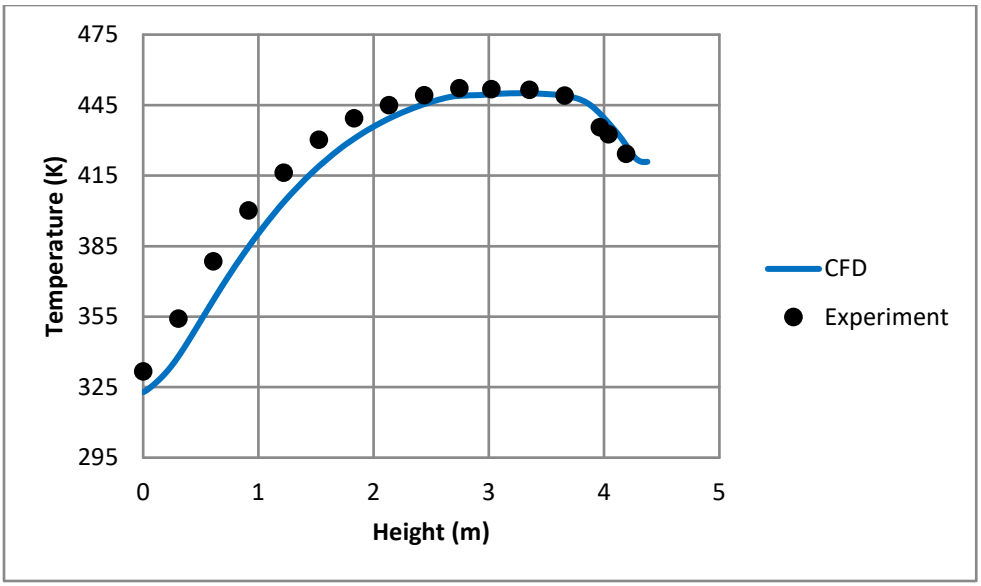

Figure B-3 Basket Temperature for the Aboveground (450 kPa, 2.5 kW) Case

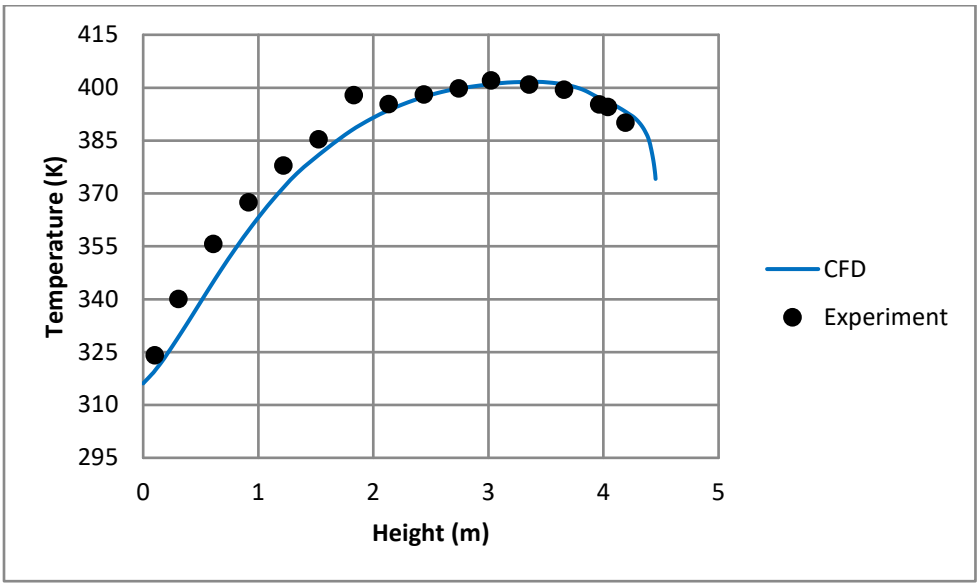

Figure B-4 Pressure Vessel Temperature for the Aboveground (450 kPa, 2.5 kW) Case

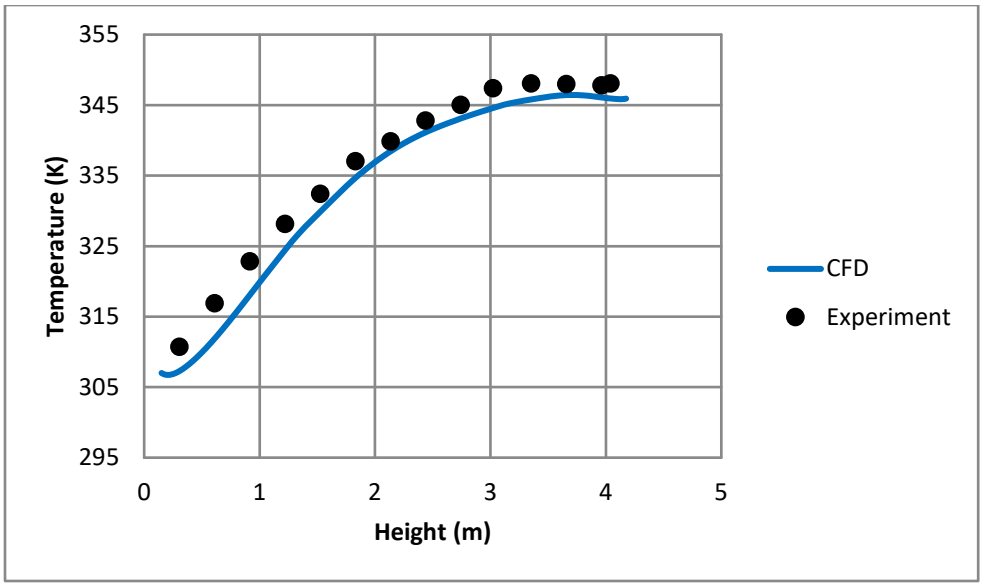

Figure B-5 Shell1 Temperature for the Aboveground (450 kPa, 2.5 kW) Case

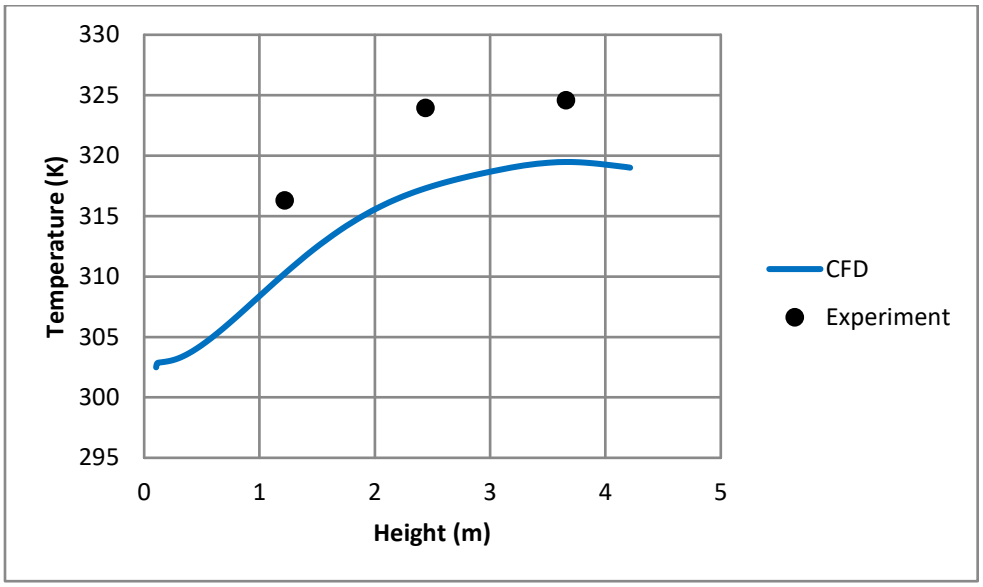

Figure B-6 Shell1-Insulation Temperature for the Aboveground (450 kPa, 2.5 kW) Case

B.1.2 Aboveground (100 kPa, 2.5 kW) Case

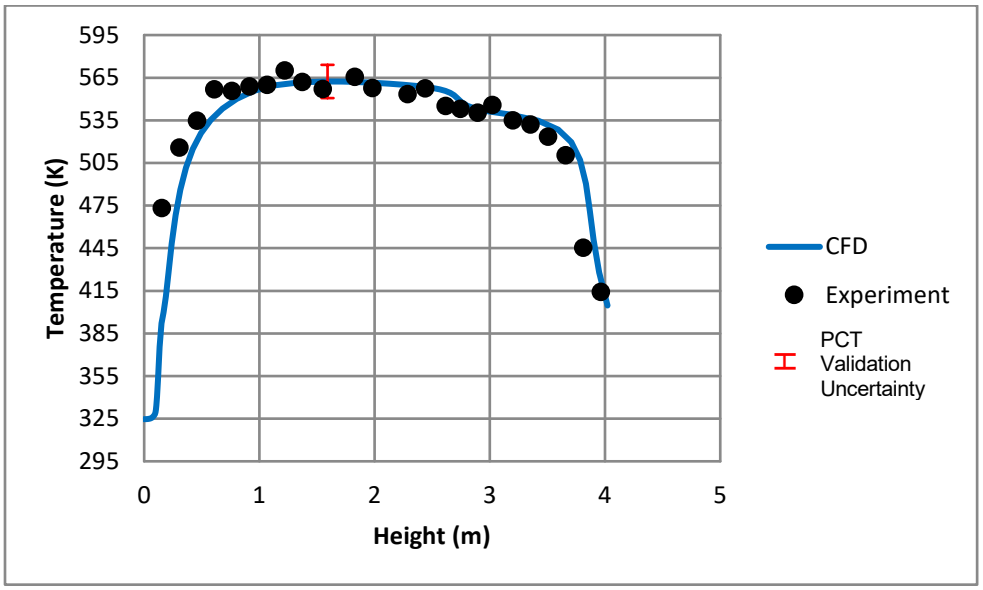

Figure B-7 PCT for the Aboveground (100 kPa, 2.5 kW) Case

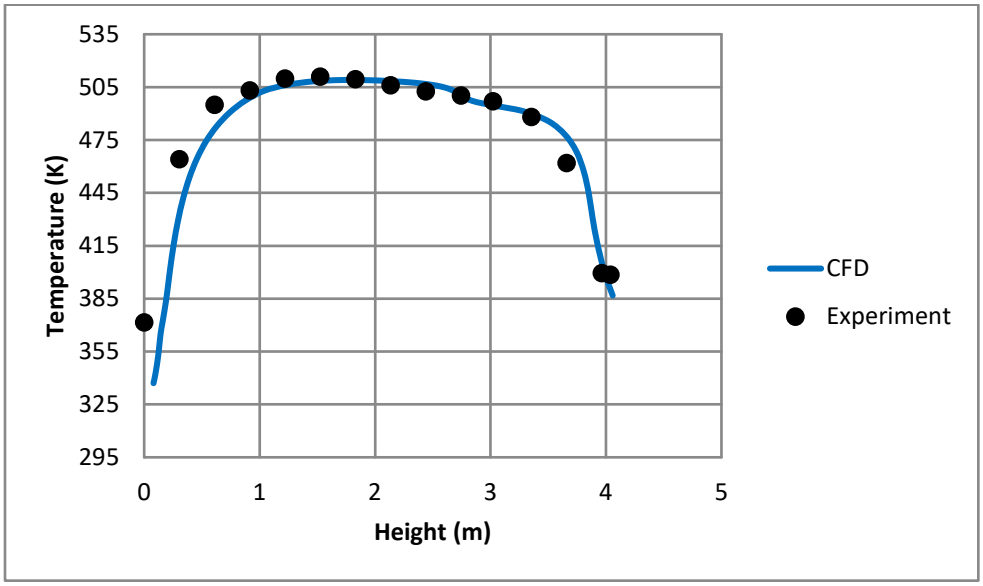

Figure B-8 Channel Box Temperature for the Aboveground (100 kPa, 2.5 kW) Case

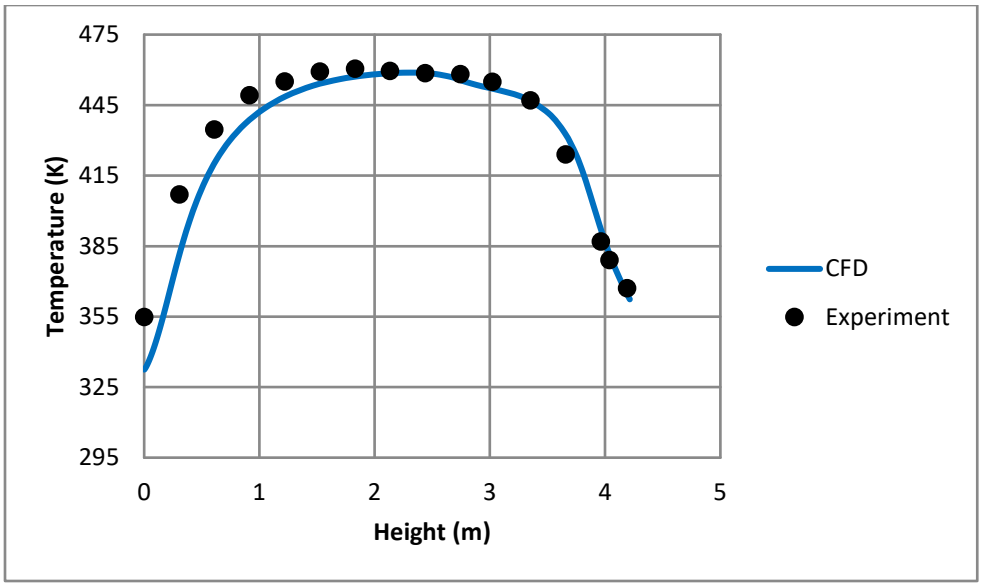

Figure B-9 Basket Temperature for the Aboveground (100 kPa, 2.5 kW) Case

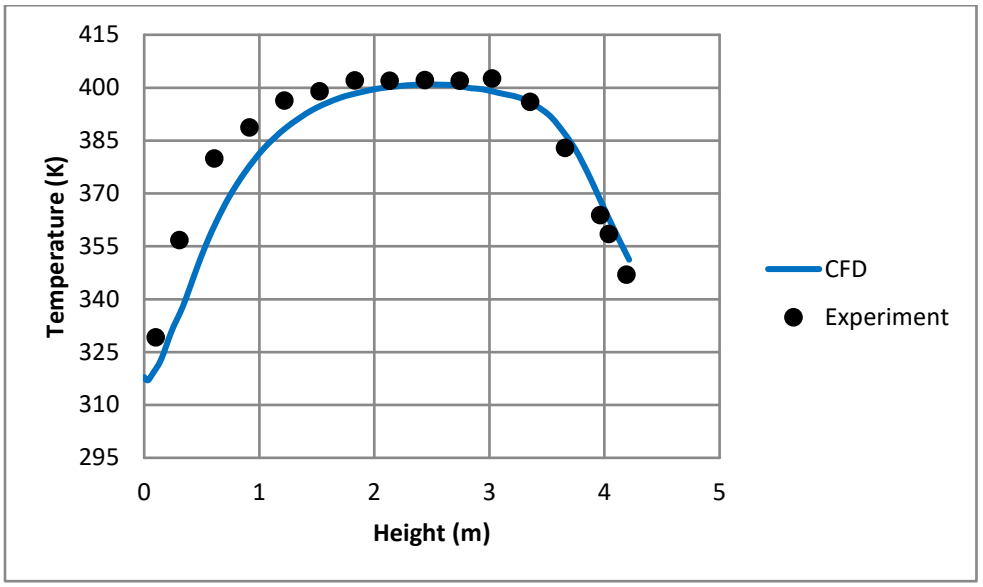

Figure B-10 Pressure Vessel Temperature for the Aboveground (100 kPa, 2.5 kW) Case

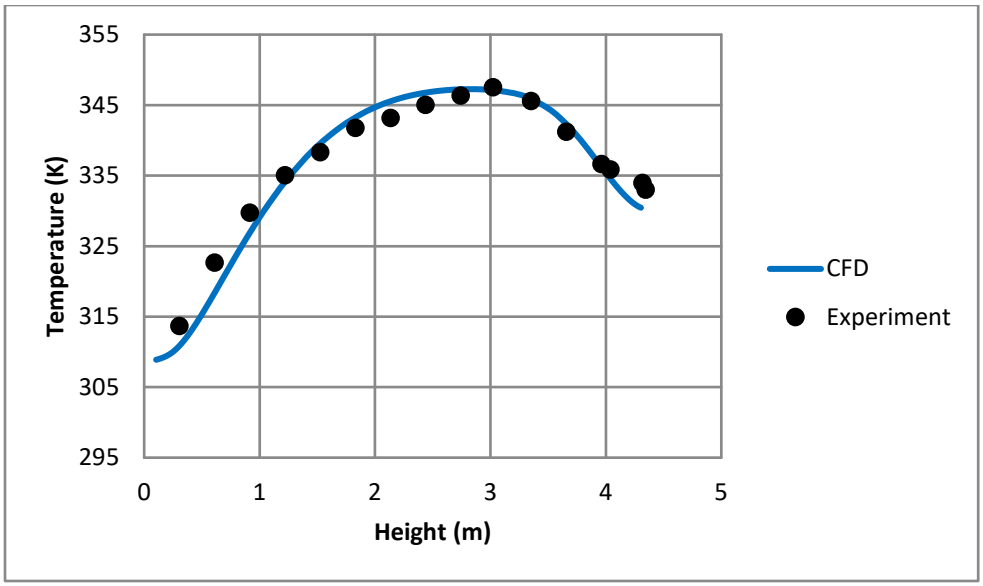

Figure B-11 Shell1 Temperature for the Aboveground (100 kPa, 2.5 kW) Case

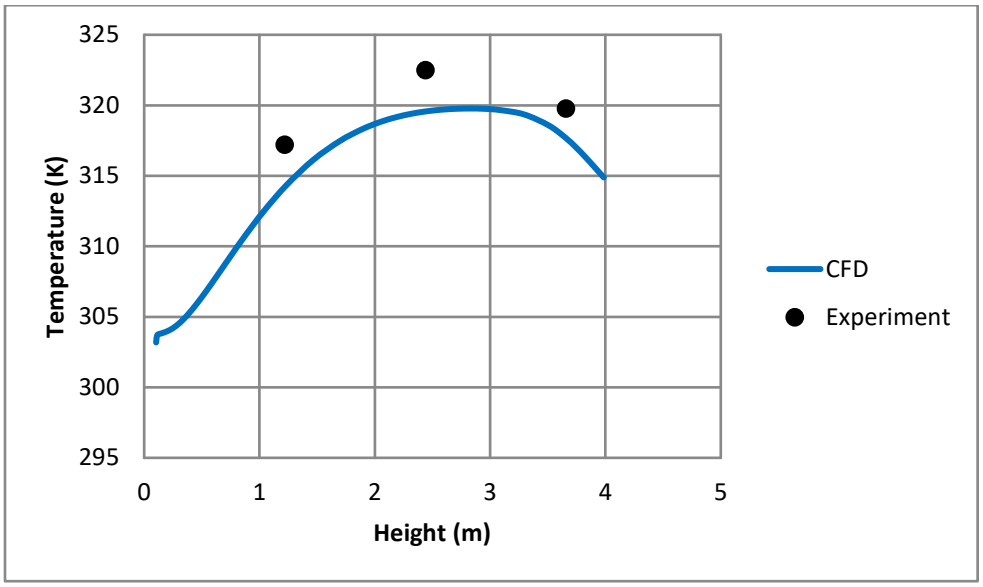

Figure B-12 Shell1-Insulation Temperature for the Aboveground (100 kPa, 2.5 kW) Case

B.1.3 Aboveground (0.3 kPa, 1 kW) Case

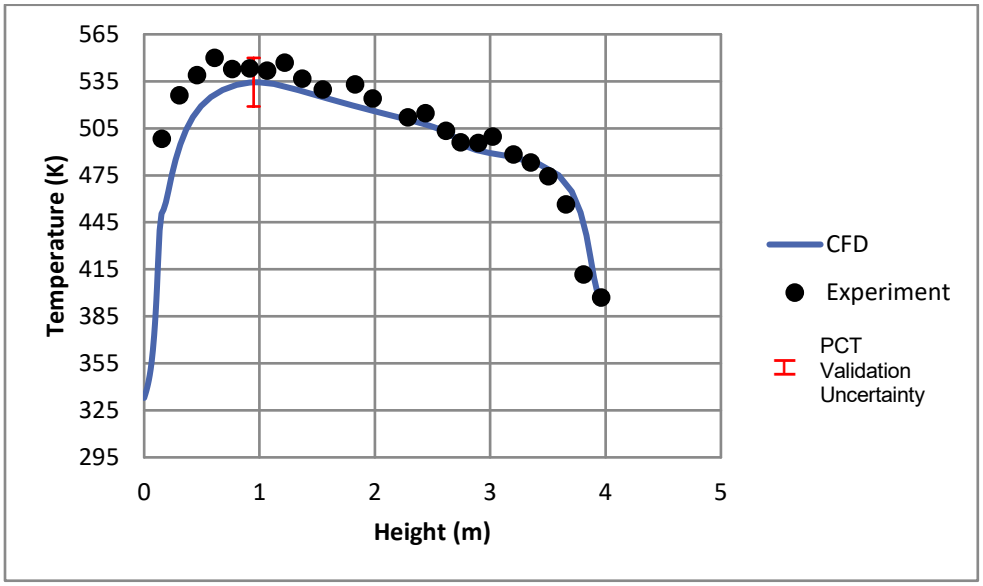

Figure B-13 PCT for the Aboveground (0.3 kPa, 1 kW) Case

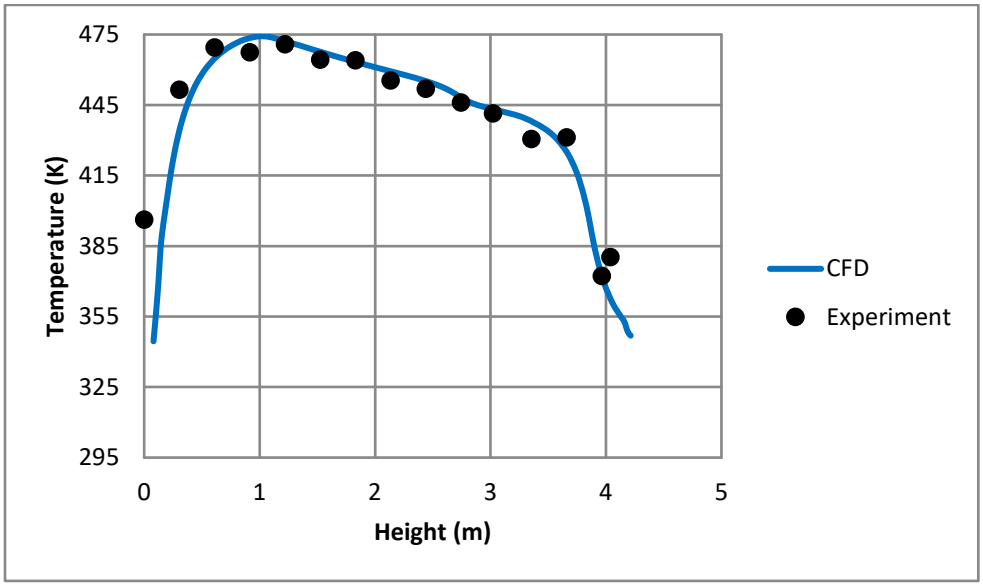

Figure B-14 Channel Box Temperature for the Aboveground (0.3 kPa, 1 kW) Case

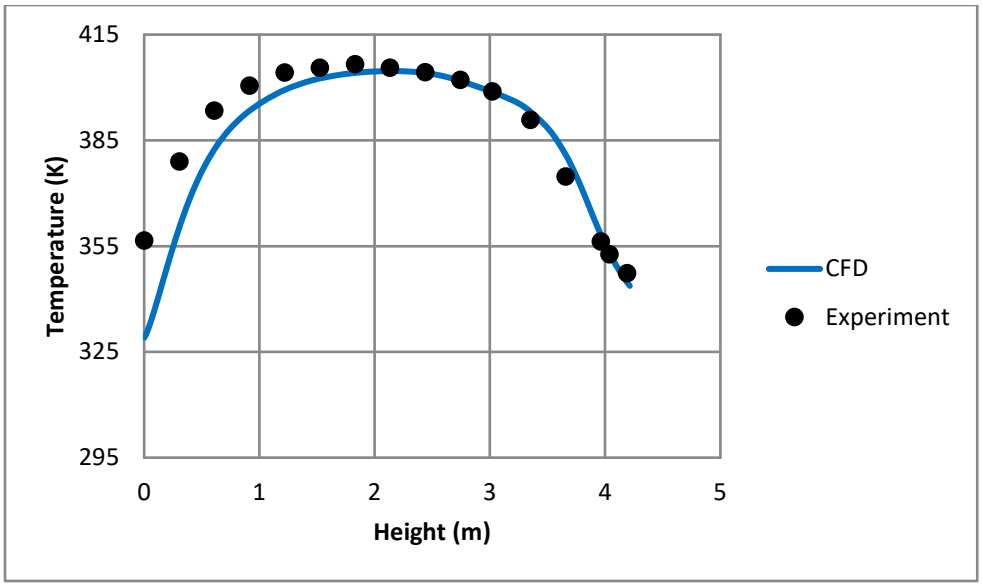

Figure B-15 Basket Temperature for the Aboveground (0.3 kPa, 1 kW) Case

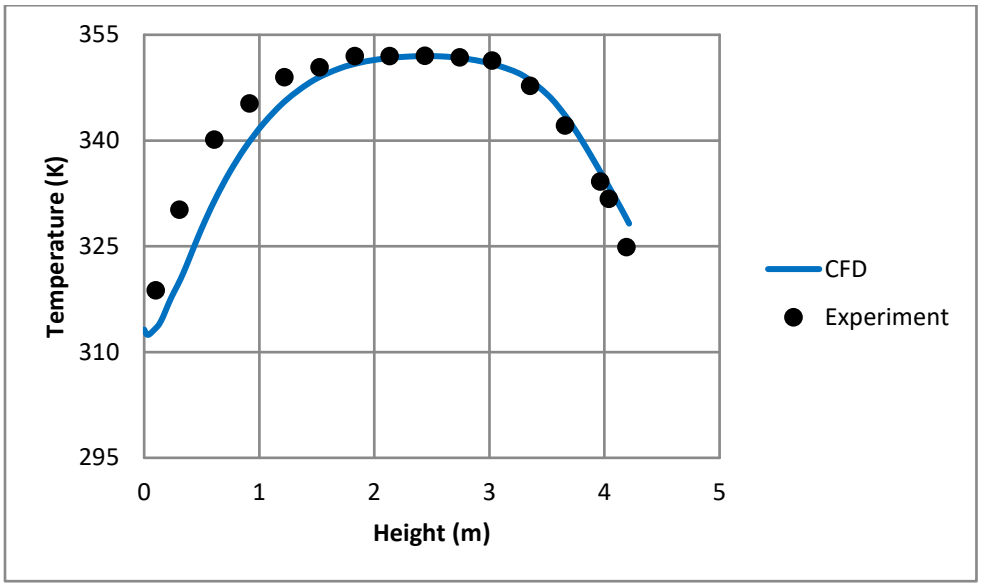

Figure B-16 Pressure Vessel Temperature for the Aboveground (0.3 kPa, 1 kW) Case

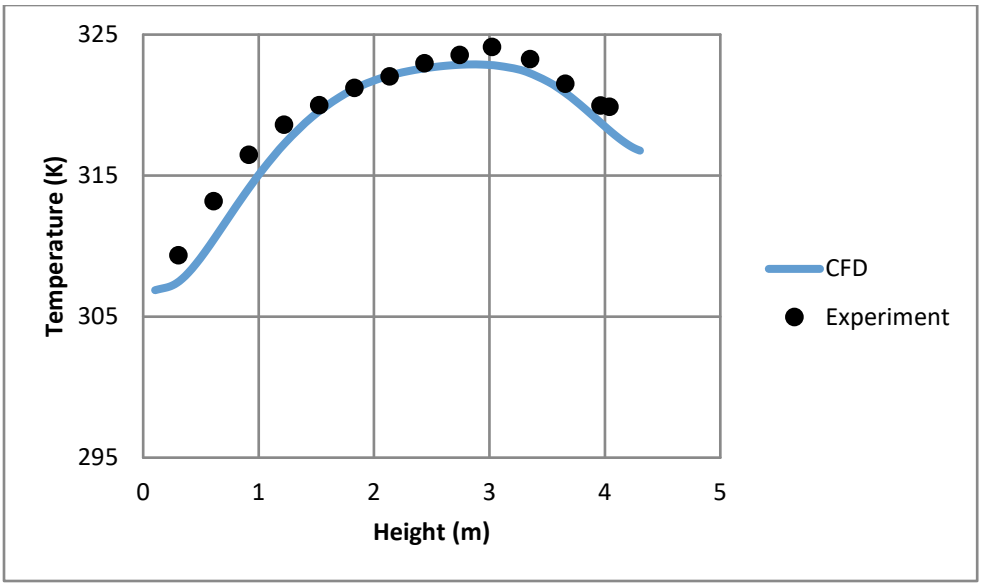

Figure B-17 Shell1 Temperature for the Aboveground (0.3 kPa, 1 kW) Case

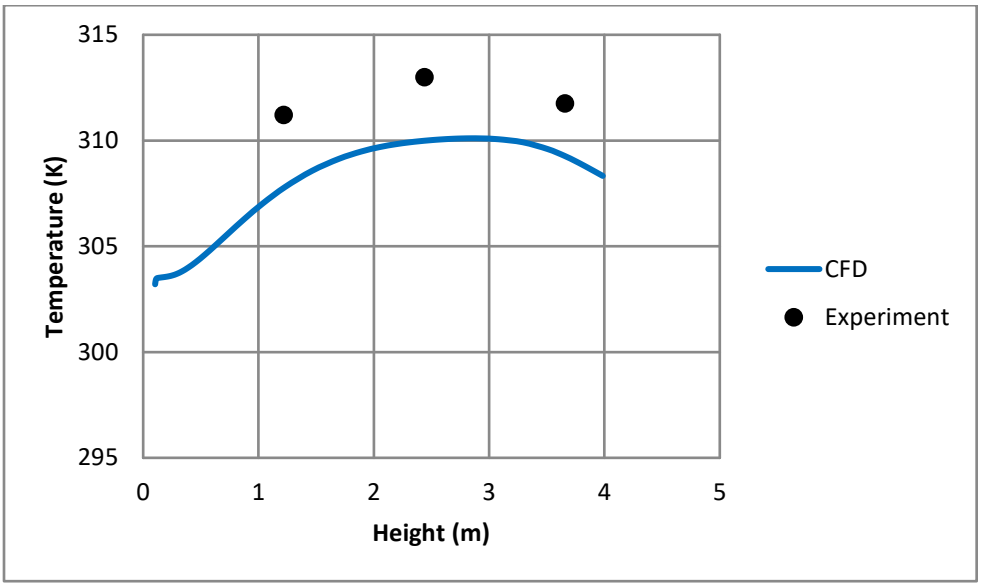

Figure B-18 Shell1-Insulation Temperature for the Aboveground (0.3 kPa, 1 kW) Case

B.1.4 Aboveground (0.3 kPa, 0.5 kW) Case

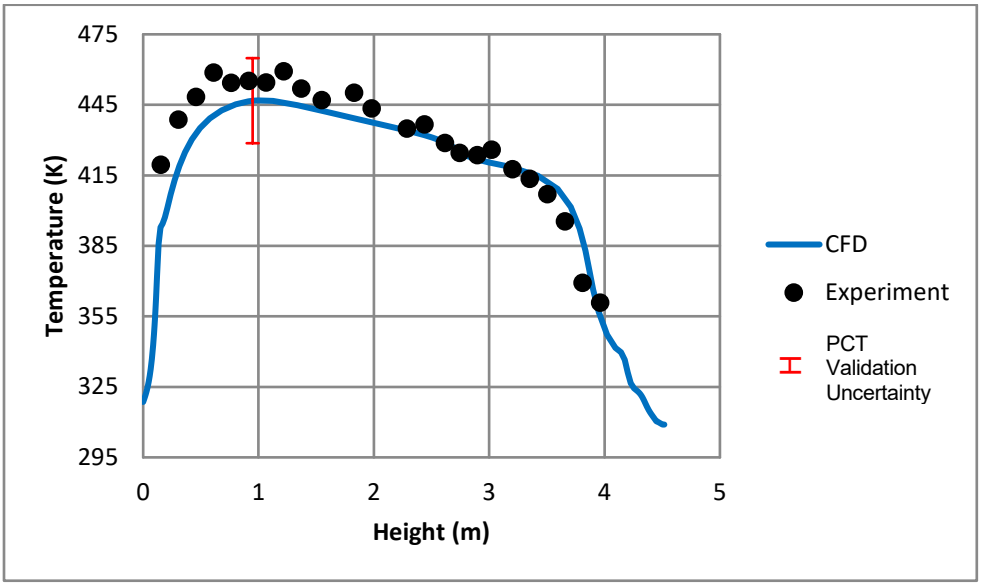

Figure B-19 PCT for the Aboveground (0.3 kPa, 0.5 kW) Case

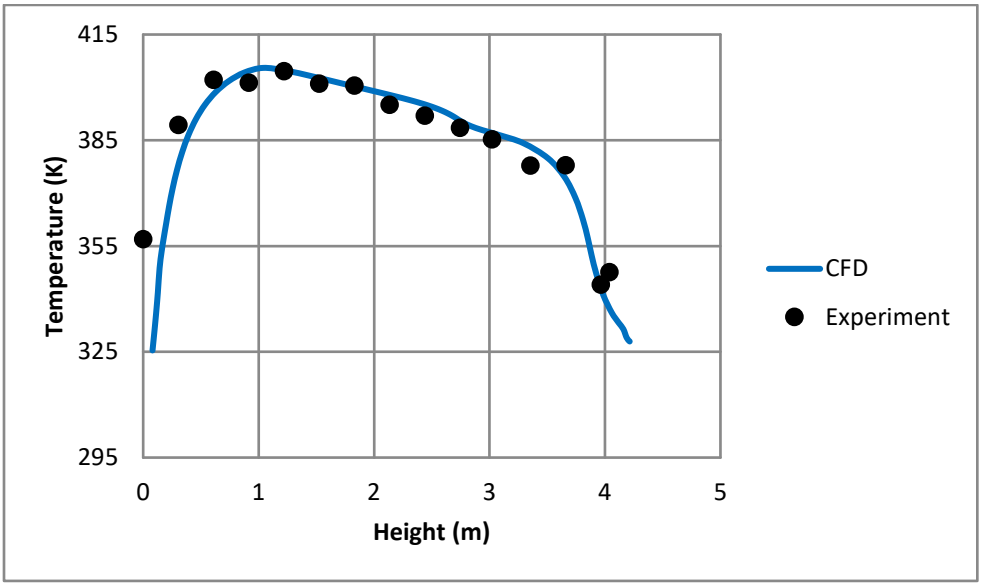

Figure B-20 Channel Box Temperature for the Aboveground (0.3 kPa, 0.5 kW) Case

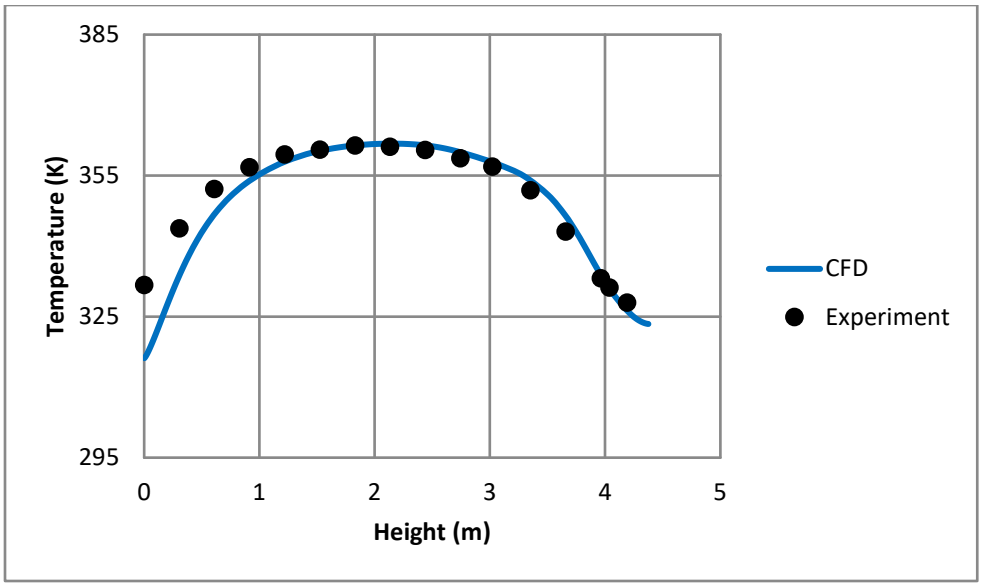

Figure B-21 Basket Temperature for the Aboveground (0.3 kPa, 0.5 kW) Case

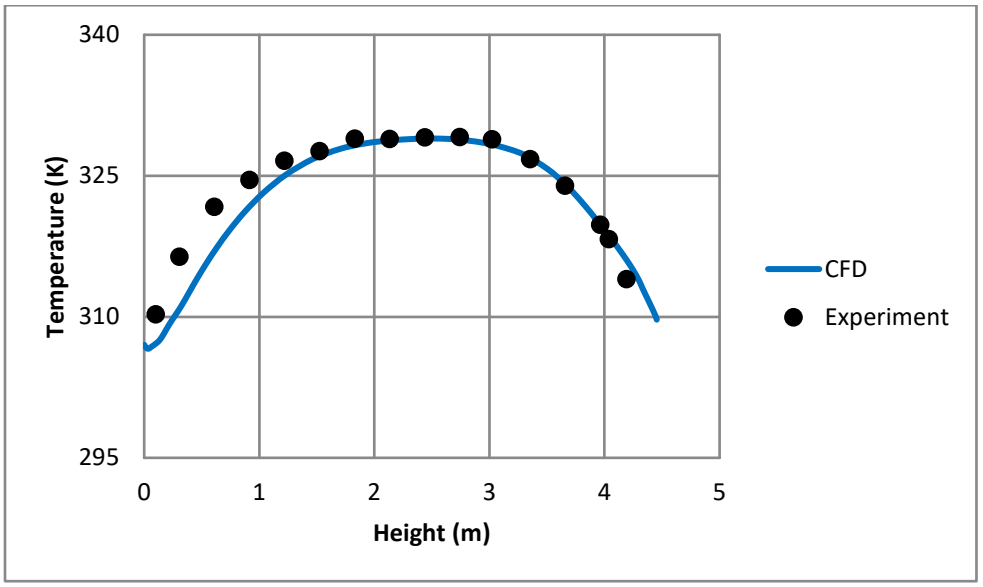

Figure B-22 Pressure Vessel Temperature for the Aboveground (0.3 kPa, 0.5 kW) Case

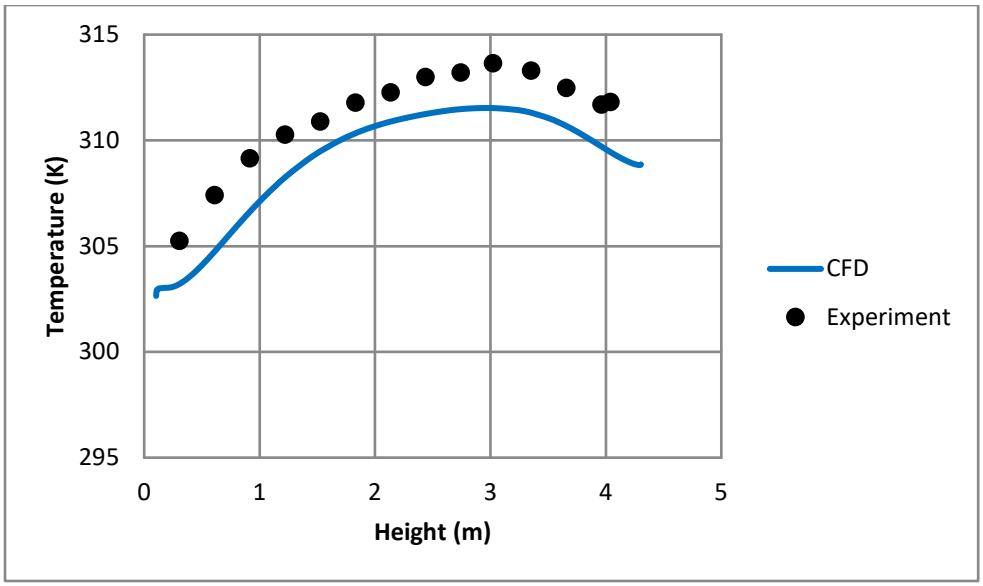

Figure B-23 Shell1 Temperature for the Aboveground (0.3 kPa, 0.5 kW) Case

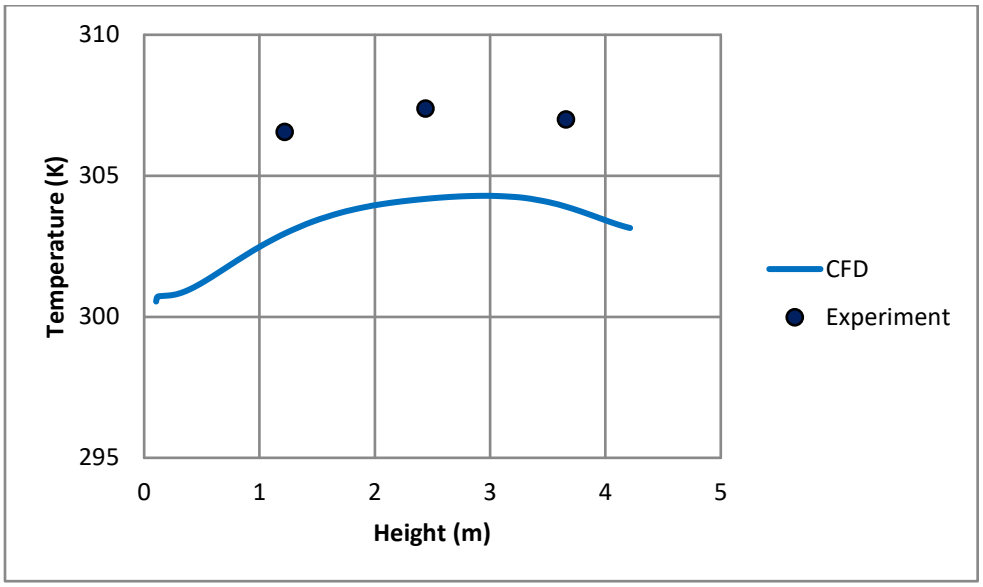

Figure B-24 Shell1-Insulation Temperature for the Aboveground (0.3 kPa, 0.5 kW) Case

B.2 Underground

B.2.1 Underground (450 kPa, 2.5 kW) Case

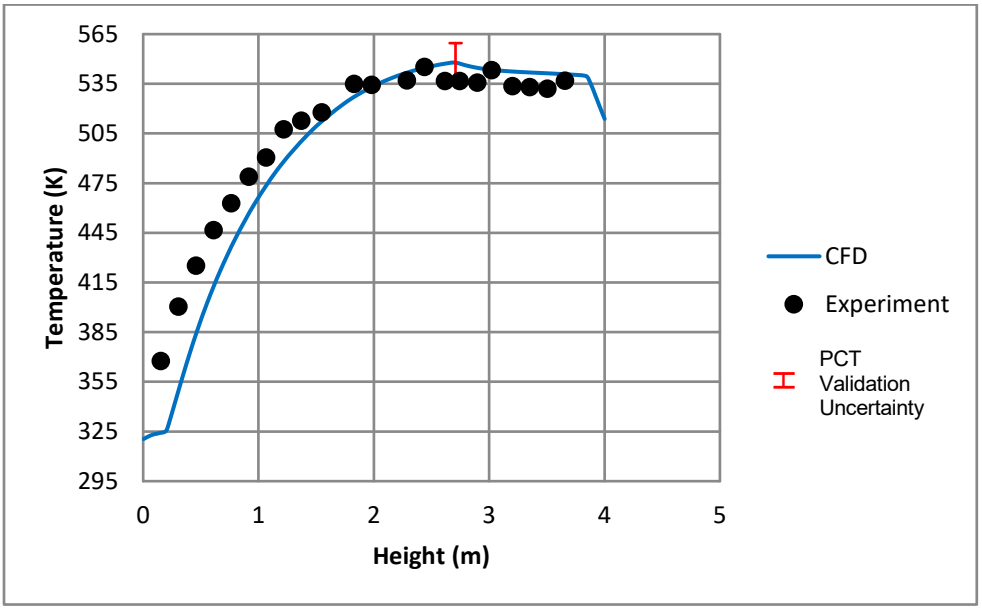

Figure B-25 PCT for the Underground (450 kPa, 2.5 kW) Case

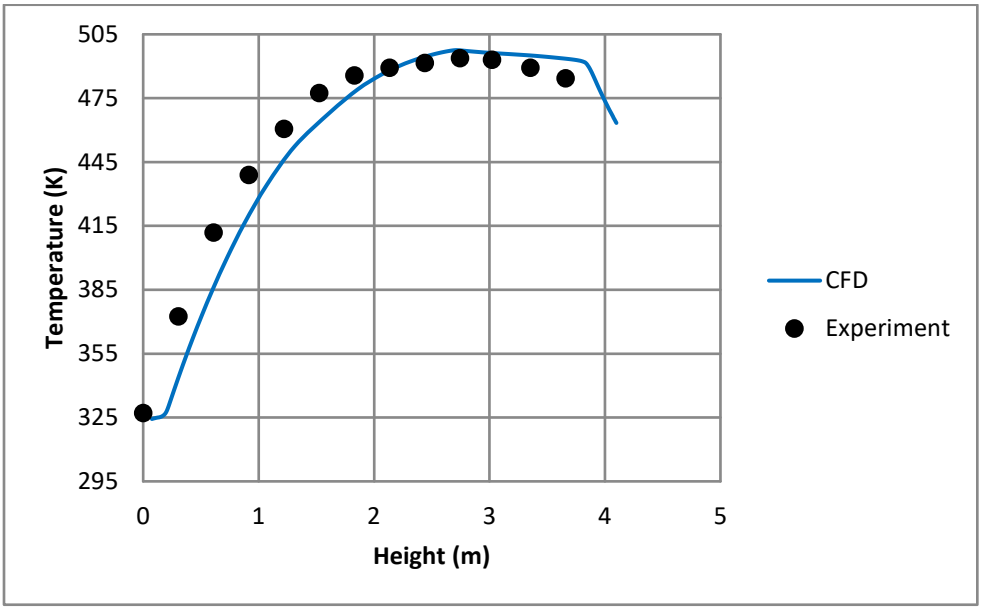

Figure B-26 Channel Box Temperature for the Underground (450 kPa, 2.5 kW) Case

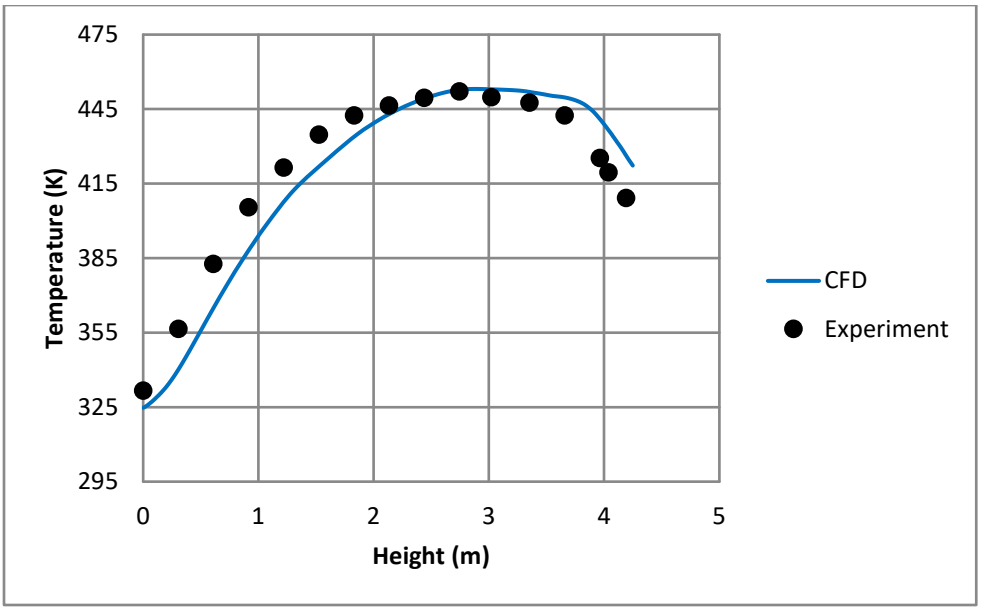

Figure B-27 Basket Temperature for the Underground (450 kPa, 2.5 kW) Case

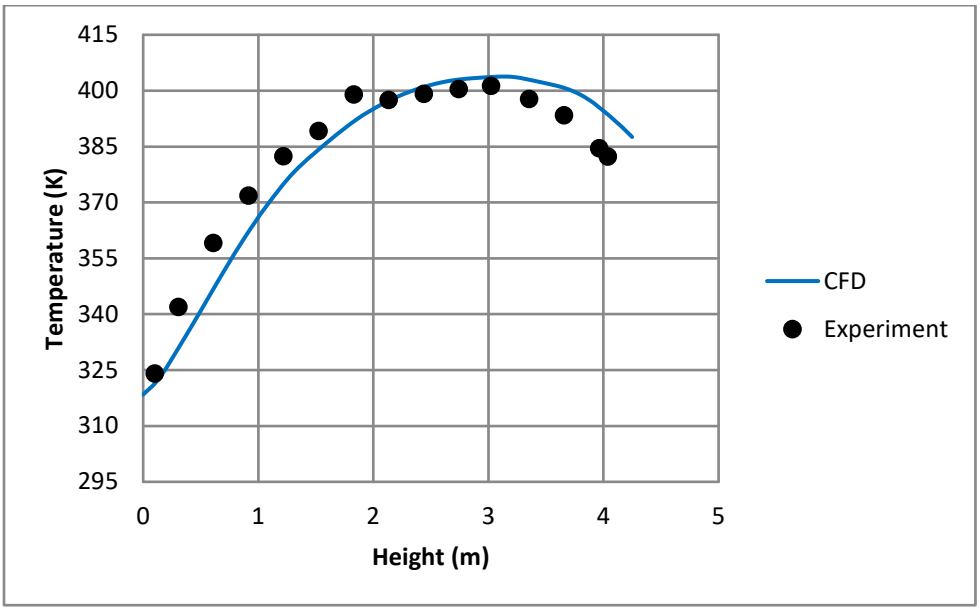

Figure B-28 Pressure Vessel Temperature for the Underground (450 kPa, 2.5 kW) Case

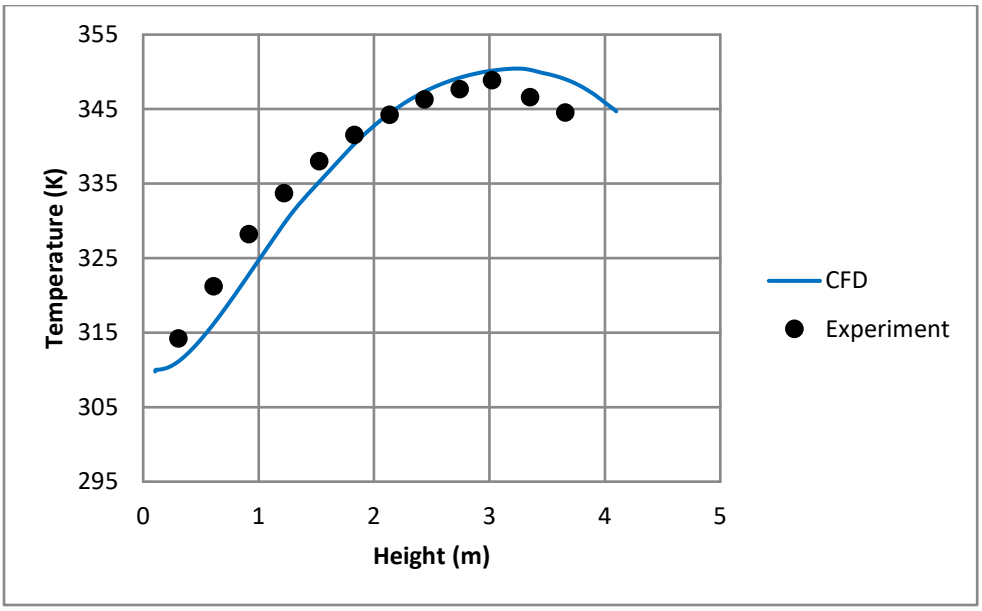

Figure B-29 Shell1 Temperature for the Underground (450 kPa, 2.5 kW) Case

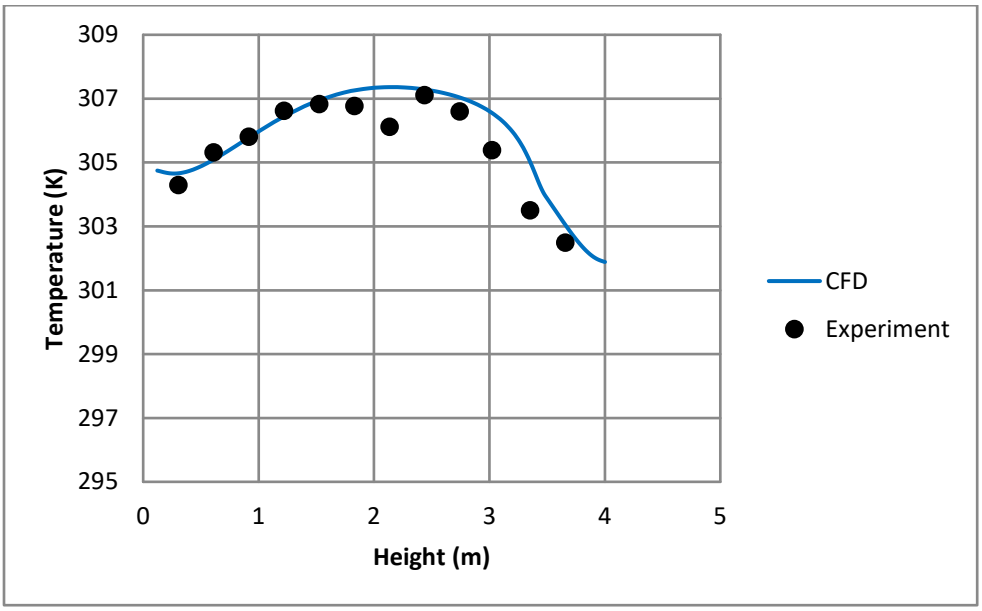

Figure B-30 Shell2 Temperature for the Underground (450 kPa, 2.5 kW) Case

B.2.2 Underground (100 kPa, 2.5 kW) Case

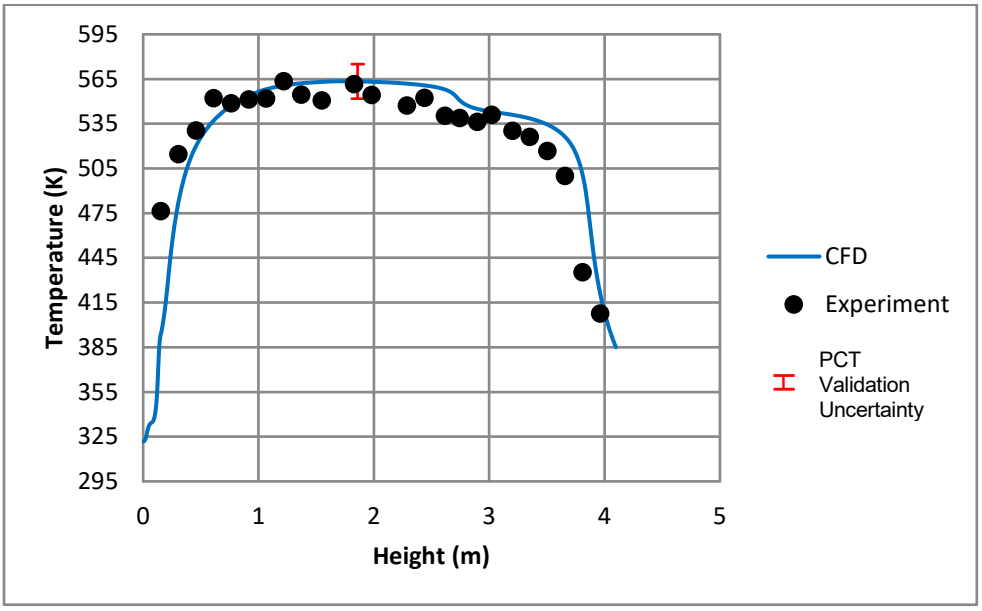

Figure B-31 PCT for the Underground (100 kPa, 2.5 kW) Case

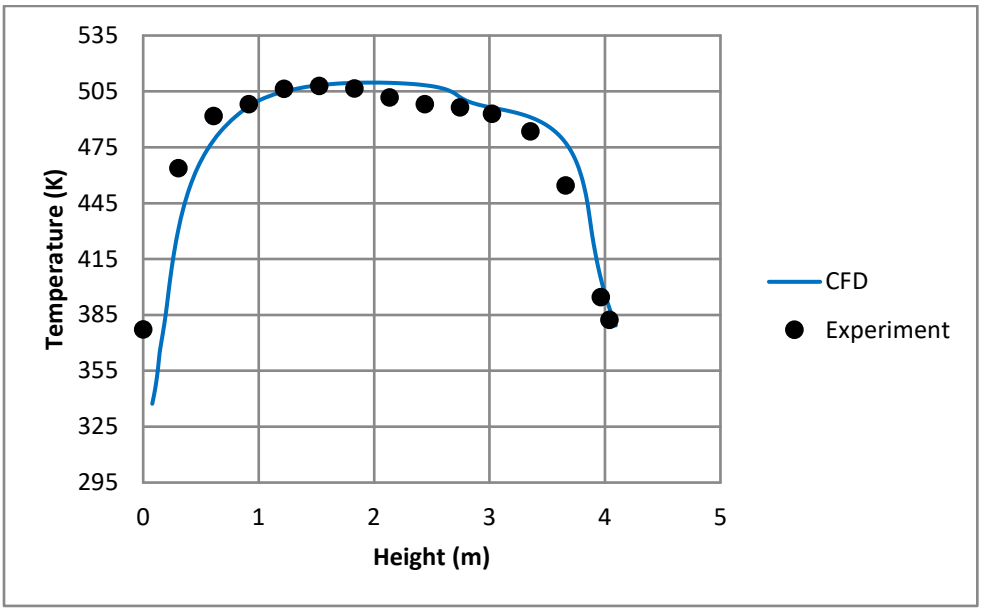

Figure B-32 Channel Box Temperature for the Underground (100 kPa, 2.5 kW) Case

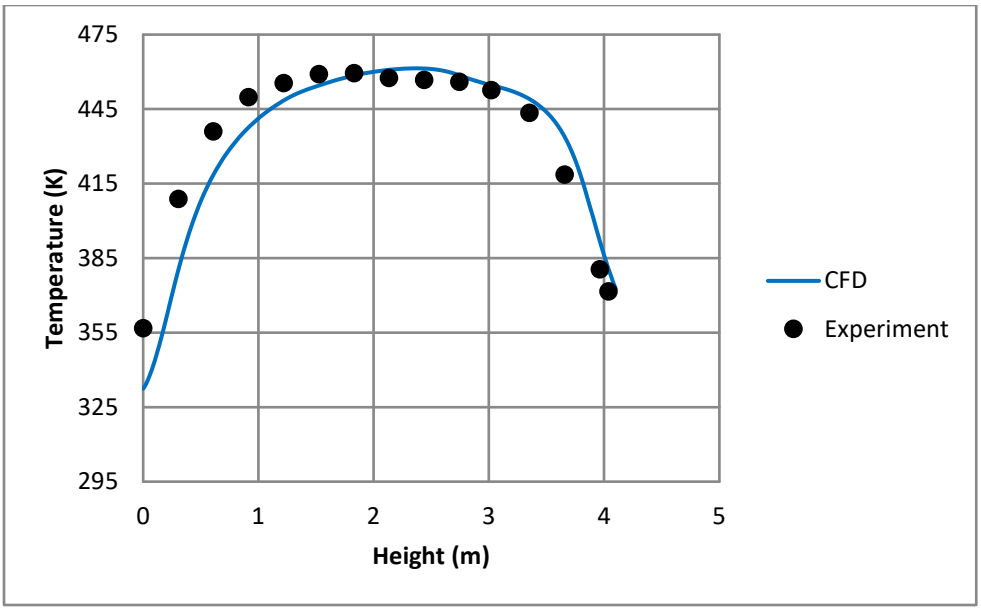

Figure B-33 Basket Temperature for the Underground (100 kPa, 2.5 kW) Case

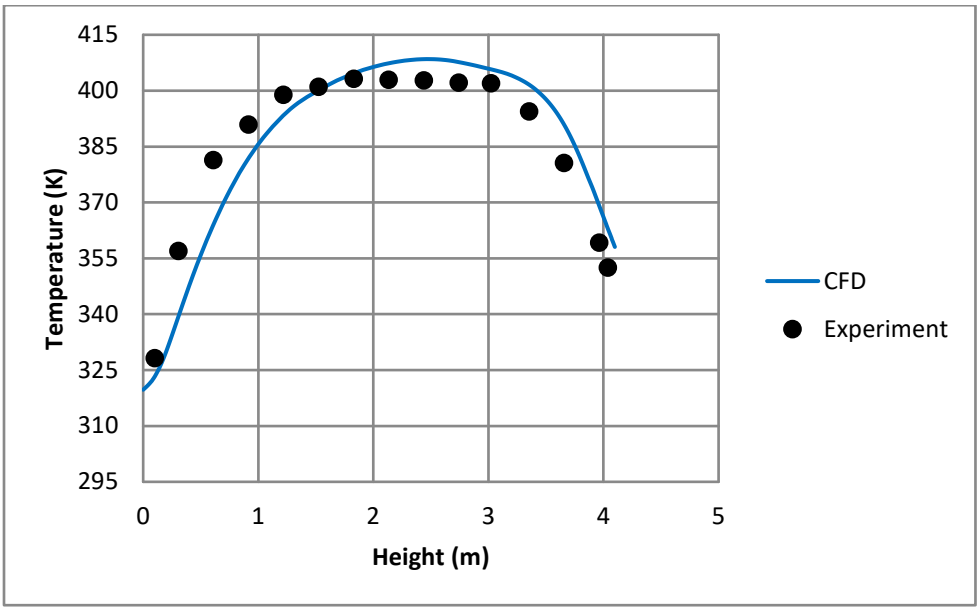

Figure B-34 Pressure Vessel Temperature for the Underground (100 kPa, 2.5 kW) Case

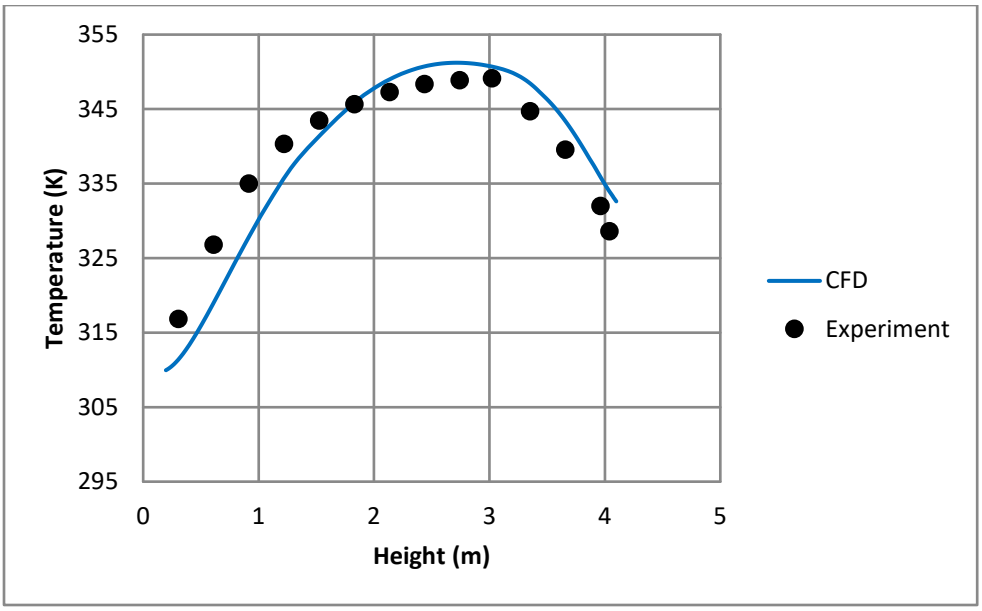

Figure B-35 Shell1 Temperature for the Underground (100 kPa, 2.5 kW) Case

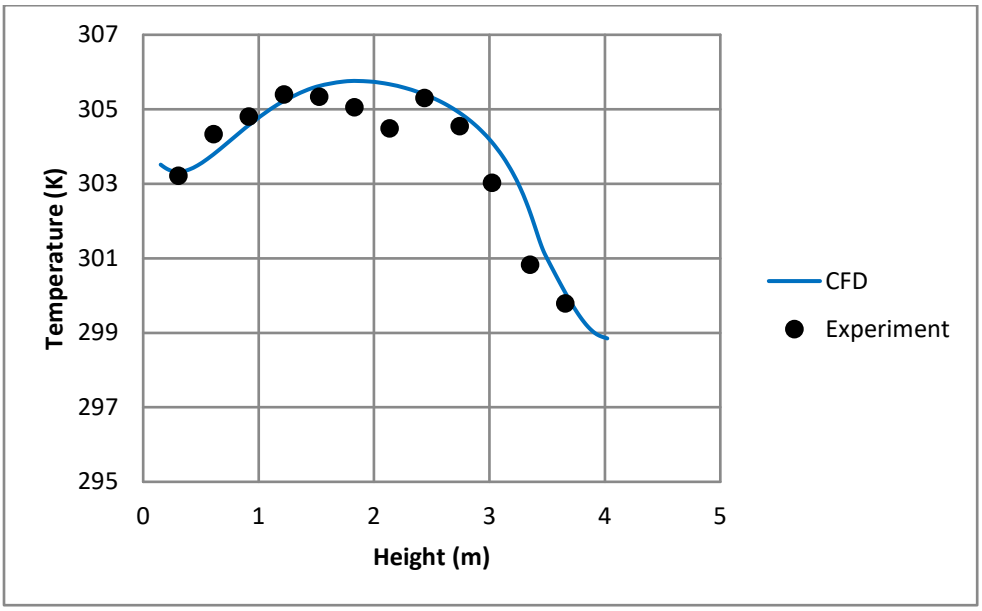

Figure B-36 Shell2 Temperature for the Underground (100 kPa, 2.5 kW) Case

B.2.3 Underground (0.3 kPa, 1 kW) Case

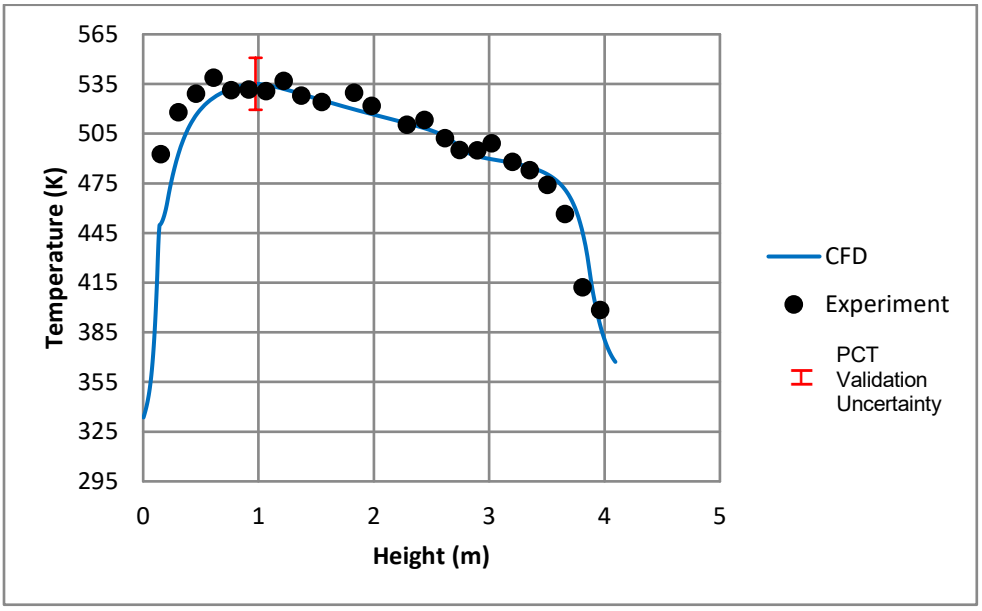

Figure B-37 PCT for the Underground (0.3 kPa, 1 kW) Case

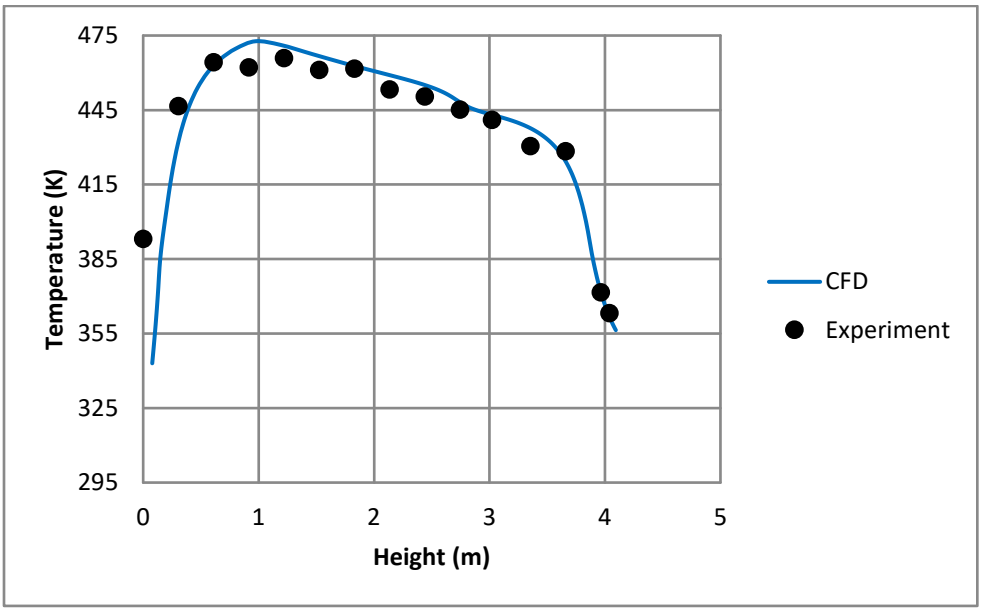

Figure B-38 Channel Box Temperature for the Underground (0.3 kPa, 1 kW) Case

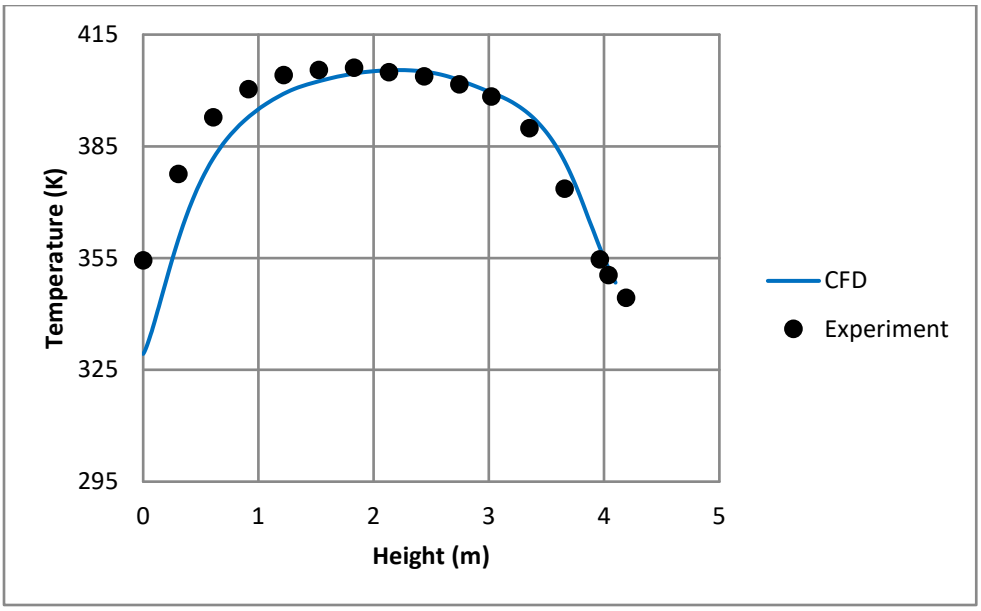

Figure B-39 Basket Temperature for the Underground (0.3 kPa, 1 kW) Case

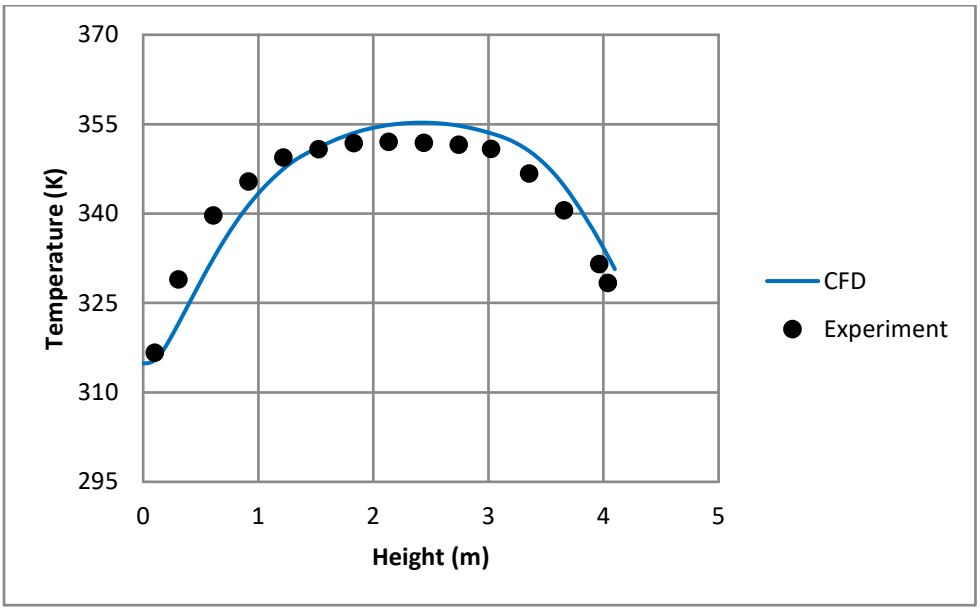

Figure B-40 Pressure Vessel Temperature for the Underground (0.3 kPa, 1 kW) Case

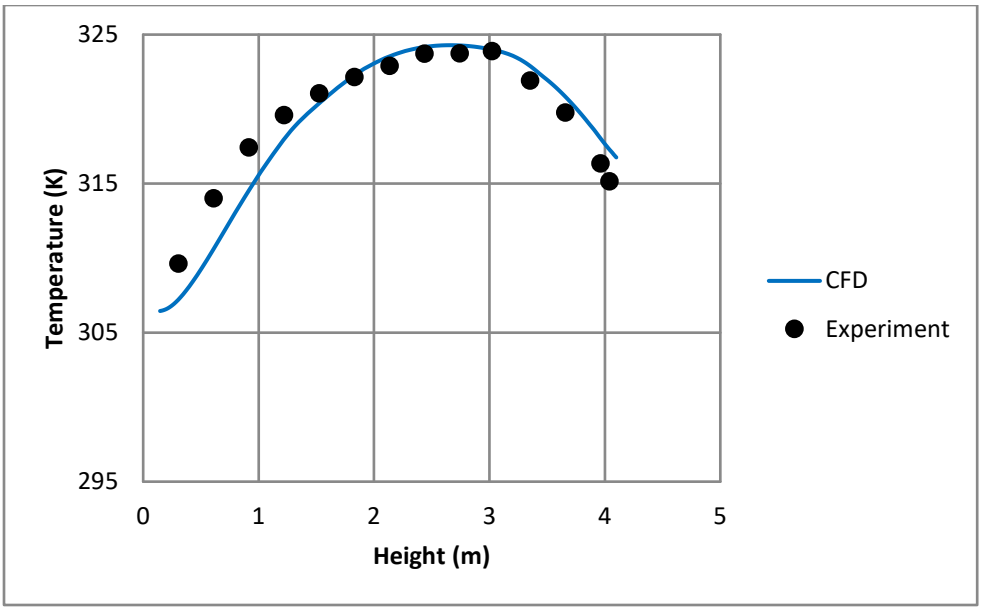

Figure B-41 Shell1 Temperature for the Underground (0.3 kPa, 1 kW) Case

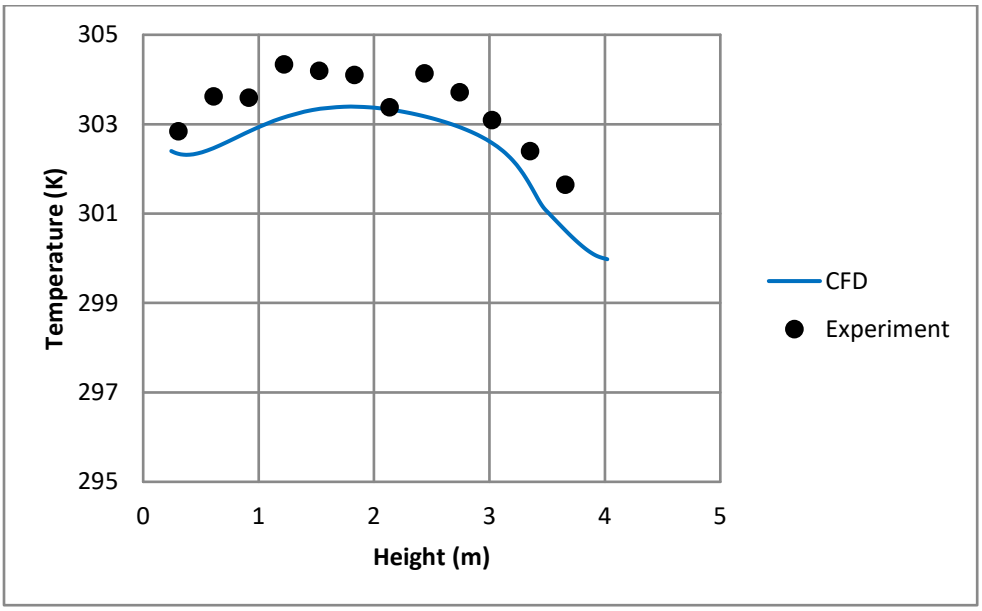

Figure B-42 Shell2 Temperature for the Underground (0.3 kPa, 1 kW) Case

B.2.4 Underground (0.3 kPa, 0.5 kW) Case

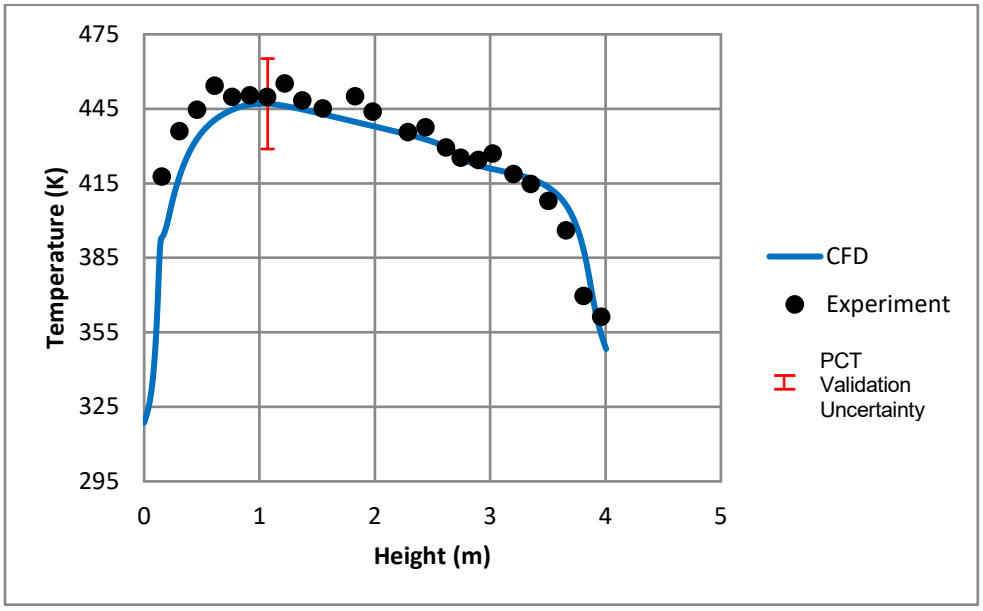

Figure B-43 PCT for the Underground (0.3 kPa, 0.5 kW) Case

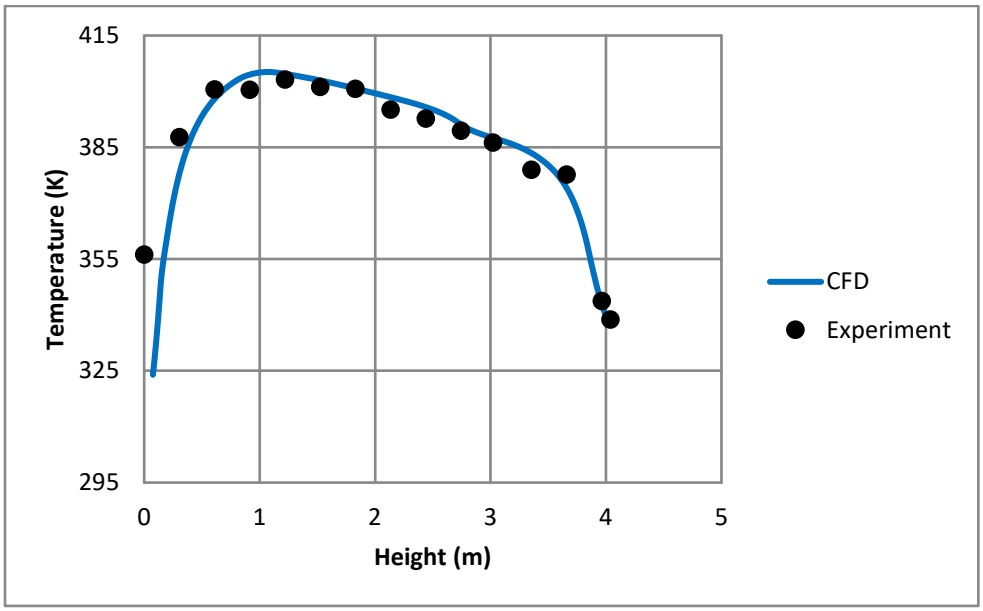

Figure B-44 Channel Box Temperature for the Underground (0.3 kPa, 0.5 kW) Case

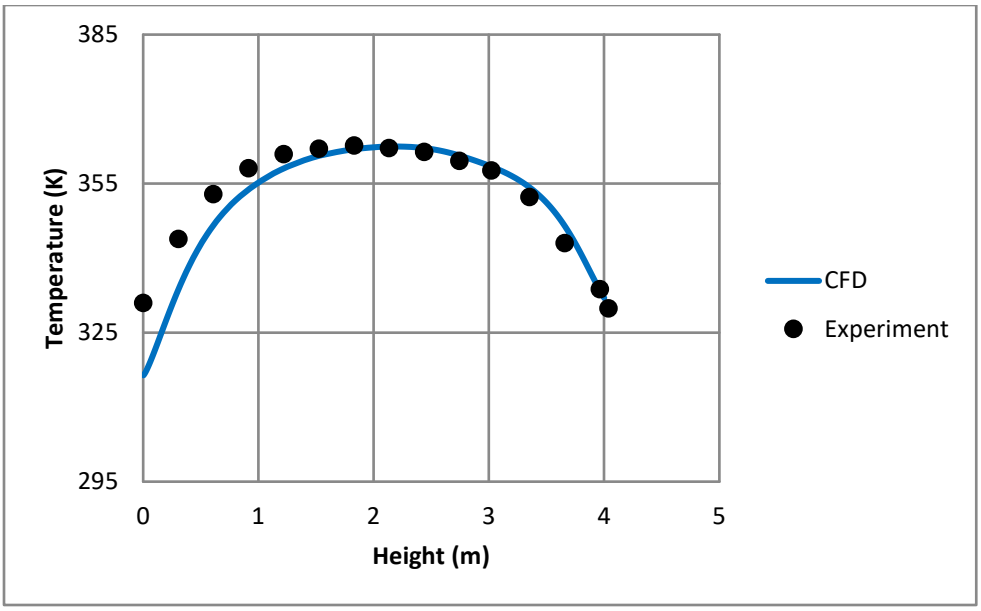

Figure B-45 Basket Temperature for the Underground (0.3 kPa, 0.5 kW) Case

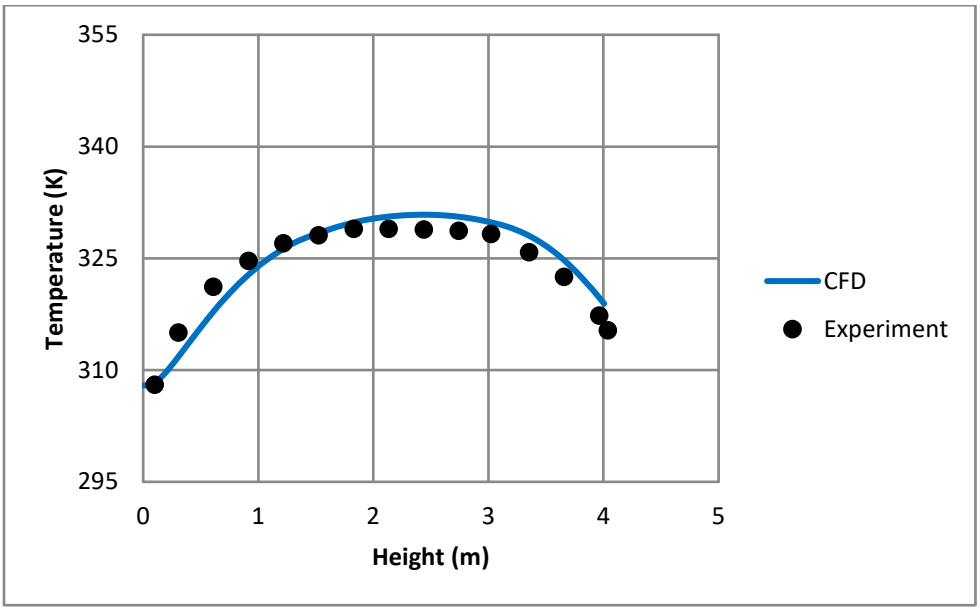

Figure B-46 Pressure Vessel Temperature for the Underground (0.3 kPa, 0.5 kW) Case

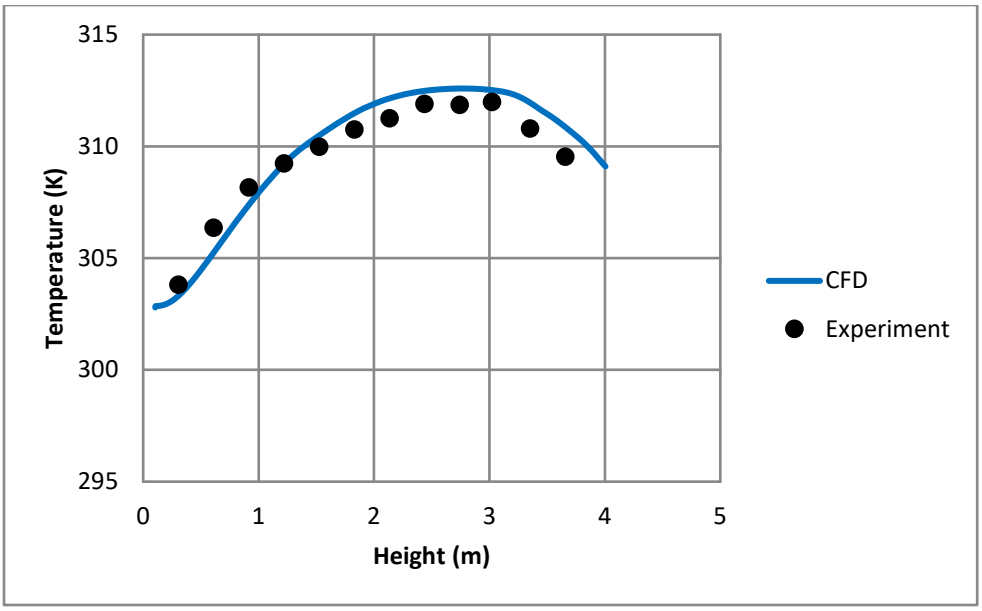

Figure B-47 Shell1 Temperature for the Underground (0.3 kPa, 0.5 kW) Case

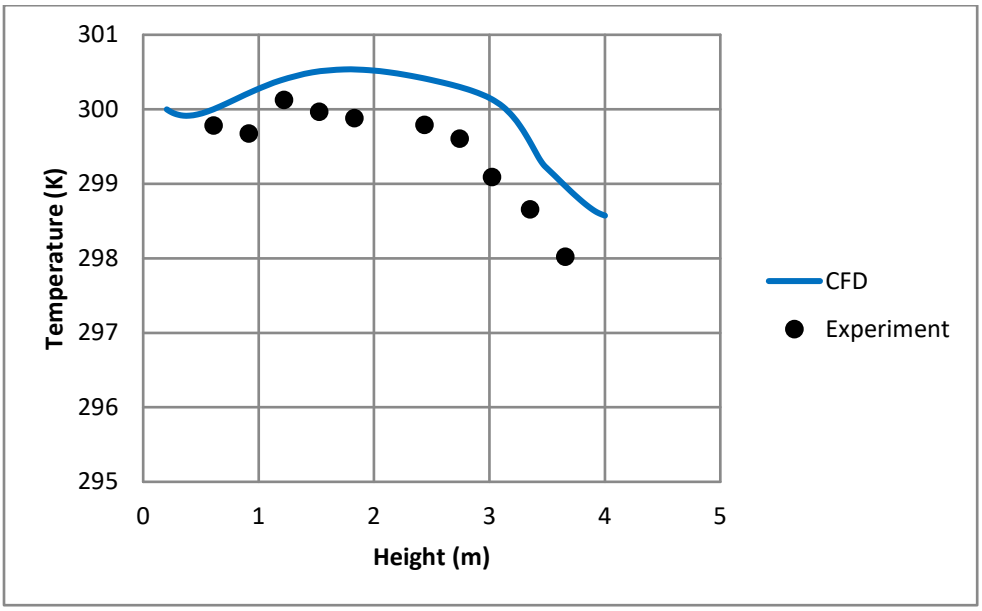

Figure B-48 Shell2 Temperature for the Underground (0.3 kPa, 0.5 kW) Case

NRC FORM 335
(12-2010)
NRCMD 3.7

U.S. NUCLEAR REGULATORY COMMISSION

BIBLIOGRAPHIC DATA SHEET

(See instructions on the reverse)

1. REPORT NUMBER
(Assigned by NRC, Add Vol., Supp., Rev., and Addendum Numbers, if any.)

NUREG-2238

2. TITLE AND SUBTITLE

Validation of a Computational Fluid Dynamics Method Using Vertical Dry Cask Simulator **Data**

3. DATE REPORT PUBLISHED

MONTH	YEAR
June	2020

4. FIN OR GRANT NUMBER

5. AUTHOR(S)

A. Zigh
S. Gonzalez

6. TYPE OF REPORT

Technical

7. PERIOD COVERED (Inclusive Dates)

8. PERFORMING ORGANIZATION - NAME AND ADDRESS (If NRC, provide Division, Office or Region, U. S. Nuclear Regulatory Commission, and mailing address; if contractor, provide name and mailing address.)

Division of Systems Analysis
Office of Nuclear Regulatory Research
U.S. Nuclear Regulatory Commission
Washington, DC 20555-0001

9. SPONSORING ORGANIZATION - NAME AND ADDRESS (If NRC, type "Same as above", if contractor, provide NRC Division, Office or Region, U. S. Nuclear Regulatory Commission, and mailing address.)

Division of Fuel Management
Office of Nuclear Material Safety and Safeguards
U.S. Nuclear Regulatory Commission
Washington, DC 20555-0001

10. SUPPLEMENTARY NOTES

11. ABSTRACT (200 words or less)

This report discusses validation and uncertainty quantification of a computational fluid dynamics model using the experimental data from NUREG/CR-7250. The primary variables of interest (i.e., target variables) in this report are air mass flow rate and peak cladding temperature. Uncertainty quantification follows the procedures outlined in ASME V&V 20-2009. Sources of uncertainty examined in the analysis include simulation input uncertainty, numerical errors (i.e., iterative, discretization, and round-off), and experimental errors.

12. KEY WORDS/DESCRIPTORS (List words or phrases that will assist researchers in locating the report.)

Spent nuclear fuel; dry storage cask; computational fluid dynamics; validation; verification; CFD-grade experiment

13. AVAILABILITY STATEMENT

unlimited

14. SECURITY CLASSIFICATION

(This Page)
unclassified

(This Report)
unclassified

15. NUMBER OF PAGES

16. PRICE

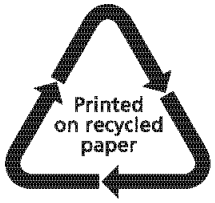

Federal Recycling Program

UNITED STATES
NUCLEAR REGULATORY COMMISSION
WASHINGTON, DC 20555-0001

OFFICIAL BUSINESS